THE UNIVERSITY *of* EDINBURGH

An electronically coarse grained molecular model of water

Flaviu Cipcigan

Doctor of Philosophy
The University of Edinburgh
March 2017

Abstract

Electronic coarse graining is a technique improving the predictive power of molecular dynamics simulations by representing electrons via a quantum harmonic oscillator. This construction, known as a Quantum Drude Oscillator, provides all molecular long-range responses by uniting many-body dispersion, polarisation and cross interactions to all orders.

To demonstrate the predictive power of electronic coarse graining and provide insights into the physics of water, a molecular model of water based on Quantum Drude Oscillators is developed. The model is parametrised to the properties of an isolated molecule and a single cut through the dimer energy surface. Such a parametrisation makes the condensed phase properties of the model a prediction rather than a fitting target. These properties are studied in four environments via two-temperature adiabatic path integral molecular dynamics: a proton ordered ice, the liquid–vapour interface, supercritical and supercooled water.

In all these environments, the model predicts a condensed phase in excellent agreement with experiment, showing impressive transferability. It predicts correct densities and pressures in liquid water from 220 K to 647 K, and a correct temperature of maximum density. Furthermore, it predicts the surface tension, the liquid-vapour critical point, density of ice II, and radial distribution functions across all conditions studied.

The model also provides insight into the relationship between the molecular structure of water and its condensed phase properties. An asymmetry between donor and acceptor hydrogen bonds is identified as the molecular scale mechanism responsible for the surface orientation of water molecules. The dipole moment is identified as a molecular scale signature of liquid-like and gas-like regions in supercritical water. Finally, a link between the coordination number and the anomalous thermal expansion of the second coordination shell is also presented.

Lay abstract

Imagine a glass of water. Inside, there are billions of billions of water molecules, each made out of two hydrogen atoms and one oxygen atom. These molecules jiggle all the time, pushing and pulling each other and interacting via what we call intermolecular forces. The properties of water (what I'll call the *macro*) depend on the details of these forces (the *micro*). For example, if the molecules like to keep close to each other, water will be denser. If on the other hand, they like to be further apart, it will be less dense.

The observation that the macro depends on the micro is a powerful one. It means we can use computer simulation to study matter at the level of atoms and molecules. We can simulate how molecules push and pull each other. From these simulations, we can *calculate* the properties of the substance they make. We can calculate how dense water is. We can calculate how hard you have to push to break its surface.

But why do so when we can already measure these things? For two reasons. First, computer simulation allows us to understand how the macro emerges from the micro. On a computer, we can do experiments that are impossible to do in the laboratory. We can ask: "What if water molecules pulled each other just a little bit more. How would that change its density?".

Second, computer simulation allows us to try out new substances. We can ask: "What if I made this particular molecule? What will it do?". In other words, we can use computers to *design* molecules for a specific purpose. We can arrange nature's ingredients – the atoms in the periodic table – to create materials never seen before. Need a better solar panel? Need an antibiotic to target a resistant bacteria? Computer simulation has started to give answers to those questions.

The interactions between atoms and molecules are governed by the laws of quantum mechanics. These are hard to simulate on a computer. Even a few

thousand atoms would need a computer larger than any ever built. Thus, scientists resort to molecular models. These are simple laws that capture the essential physics, but are faster to simulate. However, most molecular models miss a key element: the electrons of each molecule. The electrons move when other molecules move, changing the nature of interactions. This means that most models lack *transferability*. They work in one situation, say liquid water, but not in a different one, such as ice.

I am part of a team that invented a novel technique of adding electrons to molecular models while keeping them efficient to simulate. I used this technique, called electronic coarse graining, to create a new model of the water molecule. I showed that this model predicts the properties of real water in many environments: liquid water from 220 K to 800 K, high pressure ice and the surface between the liquid and the vapour.

I also discovered a new link between micro and macro. In my simulations, the way water molecules push and pull each other is different on the side of the oxygen atoms than on the side of the hydrogen atoms. This *asymmetry* makes water molecules orient at the interface between liquid water and vapour in a particular way that can be measured by shining laser light onto the surface of water.

My work makes computer simulation of atoms and molecules more *predictive*. In other words, it gives us a tool to confidently predict macro from micro with only a computer and a knowledge of the underlying laws of physics.

Declaration

I declare that this thesis was composed by myself, that the work contained herein is my own except where explicitly stated otherwise in the text, and that this work has not been submitted for any other degree or professional qualification except as specified. Where the work was done in collaboration with others, a significant contribution was made by the author.

Parts of this work have been published in Cipcigan et al. [52, 53, 54], Jones et al. [123, 124], Sokhan et al. [254, 255].

(*Flaviu Cipcigan, March 2017*)

Structure of thesis and contributions

The work presented in this thesis was done in a collaboration between the University of Edinburgh, National Physical Laboratory and IBM T.J. Watson Research Center that included myself, Dr. Vlad Sokhan, Dr. Andrew Jones, Prof. Glenn Martyna and Prof. Jason Crain. The thesis is written as a coherent body of work, presenting the story of the past four years where we developed and validated an electronically coarse-grained model for water and used it to understand how the condensed phase properties of water emerge from its molecular structure. My role in the team was the latter: understanding the structure of liquid water using this newly proposed model. Thus, a large part of the thesis is dedicated to interpreting the results of the simulations in the context of the physics of water. Each chapter that contains work co-authored by myself begins with the title of supporting publications.

Chapter 1 introduces the main argument of the thesis and places electronically coarse-grained methods in the context of predictive materials modelling. The discussion is based on my own thoughts and is new material written for the purpose of this thesis.

Chapter 2 presents a review of the development of Quantum Drude Oscillators, a framework for electronic coarse-graining. It is based on a perspective article I wrote for a special edition of the Journal of Computational Physics [53]. Section 2.2.4 is my original work that is unpublished.

Chapter 3 presents the development of QDO-water, an electronically coarse-grained model of water. The first part is a review of existing water models, which is new material written for the purpose of this thesis. Section 3.3 presents the parametrisation of QDO-water. The parameters were chosen and optimised by Dr. Vlad Sokhan with contributions from Dr. Andrew Jones, Prof. Glenn Martyna and myself. Ab initio simulations of the dimer potential energy surface were performed by Dr. Vlad Sokhan. The cluster calculations in Section 3.4 are my original work and is unpublished.

Chapters 4-7 present and interpret simulations of QDO-water in four different environments: the liquid-vapour interface, ice II, supercritical and supercooled

water. The simulations were performed by myself and Dr. Vlad Sokhan using the following HPC services: Hector and Archer (EPCC), Blue Joule and Blue Wonder (Hartree Centre) and local clusters at the University of Edinburgh (including the CM-CDT condensed matter cluster) and the National Physical Laboratory. The analysis, conclusions and figures are my own unless explicitly mentioned in the figure caption. Chapter 5 is based on work published in Cipcigan et al. [52], with Section 4.3.7 being unpublished. Chapters 4 and 6 are mainly written for the purpose of this thesis, with the results published in two papers I co-authored [254, 255]. Chapter 7 is based on a manuscript in preparation [54].

Chapter 8 and 9 wrap the thesis up, discussing the merits of the model and suggesting future work. They are new material written for the purpose of this thesis

Software All the software written by myself during the course of this thesis is open sourced on my bitbucket repository at `bitbucket.org/flaviu`.

Acknowledgements

The research presented in this thesis has been challenging yet greatly satisfying. I'd like to thank my research supervisors, whom I had the honour of working with: Prof. Jason Crain, Prof. Glenn Martyna, Dr. Vlad Sokhan and Prof. Graeme Ackland. I'd also like to thank Dr. Andrew Jones for his collaboration and valuable advice.

This work would not have been possible without the generosity of my sponsors. I thank the EPSRC, the Scottish Doctoral Training Centre in Condensed Matter Physics and the National Physical Laboratory for funding, along with the EPCC, Hartree Centre and the University of Edinburgh for generous allocation of computational resources.

During my PhD, I've had the honour of being embedded in a vibrant research environment through the four institutions I was affiliated with: the University of Edinburgh, the Scottish Doctoral Training Centre in Condensed Matter Physics, the National Physical Laboratory and IBM T.J. Watson Research Centre. I'd like to thank my colleagues from these institutions for their wisdom and advice. Since working between three cities involved a good deal of travel, I'd like to thank my hosts in Teddington, Sarah and Jamie, and in New York, Alan, for opening up their homes to me. A further thanks goes to Dr. Dennis Newns who supervised me during my placement at IBM Watson, and to Dr. Richard Burguete and the NPL Postgraduate Institute, which I had the honour to represent as a postgraduate ambassador while at the NPL.

A PhD is so much more than just research and I'd like to thank those who made it so. I've had the pleasure of taking part and organising outreach events in major science festivals throughout Scotland. Thank you Anne and Katherine for putting together the kitchen science events. Thank you Toby and Andrew for helping me build the oobleck-on-a-speaker demo. Thank you Carole and Jack for making me a part of the Quantum Circus. Thank you Ian and Ross for enticing artists and scientists to work together for the SCART connection. Thank you Sam and Rachel for transforming my research into a sculpture and thank you Gio for all the amazing ideas on algorithmic music composition we're still putting into practice!

Teaching was also something dear to me and I'm privileged to have taught amazing groups of students. Thank you Victoria for inviting me to host

presentation skills workshops for Masters students. Thanks to all the students who have challenged me with their questions and to all my colleagues in Introduction to Academic Practice for giving me a flavour of modern theories of teaching.

Most importantly I'd like to thank my family, in particular my mother Liana and my grandparents Viorica and Miron for their support, encouragement and open arms. You've all made my life so much richer.

Contents

List of Figures

List of Tables

Chapter 1

Introduction

Atomistic materials modelling has become an integral part of research in all areas of condensed matter, forming a new part of the scientific method, elucidating scientific principles and accelerating discovery of new materials. The computational revolution has been driven by the exponential scaling of computer hardware [192] along with implementation of scalable software on these platforms [207]. Today we can perform computational feats inconceivable 50 years ago. We can calculate the band structure of a periodic crystal using a smartphone [198] and simulate the influenza virus with atomic detail on a supercomputer [222].

The progress in atomistic materials modelling has led to the discovery of new materials and medicine. For example, Schames et al. [240] found a hidden binding site in HIV integrase, which lead to the development of the small molecule drug raltegravir that halts the progression of HIV into AIDS [240]. A second example is the rational design of a multiferroic material for measuring the electron's dipole moment [231].

The progress has also lead to a better understanding of atomic and molecular scale mechanisms in systems ranging from solid state materials to proteins and cells. For example, the design rules behind the folding of proteins have begun to be understood well enough to enable the design of amino acid sequences that fold into desired structures [115, 142, 270], although complete success remains elusive.

Despite these successes, two major challenges still limit the predictive power of atomistic materials modelling: the accuracy of the models and the timescales reached in simulation.

This thesis addresses the former challenge: improving the accuracy of the approximations used to model materials at the scale of atoms and molecules. I address the challenge by constructing a model of the water molecule using a novel technique known as electronic coarse graining. The essence of this technique is to replace the electrons of a molecule with a simpler system – in this case, a quantum harmonic oscillator.

Electronic coarse-graining has been pioneered by the work of Whitfield and Martyna [297, 298] and improves the accuracy of molecular dynamics force fields by providing many-body polarisation and dispersion beyond the dipole level in a single, efficient to simulate building block. This building block is a quantum harmonic oscillator known as a quantum Drude oscillator in the honour of Paul Drude [70], who was first to use such a system to study condensed matter.

To construct an electronically coarse grained model of water, a frame consisting of fixed charges is combined with a quantum Drude oscillator and an empirical repulsion term. The parametrisation of the model contains no condensed phase data, being done using the charge density and responses of the isolated molecule and a single cut through the dimer energy surface.

The model is then assessed in four environments to test its predictive power and understand the link between the molecular structure of water and its condensed phase properties. First, I look at a proton ordered ice: ice II. Then, liquid water follows, at its interface with vapour and its limits of stability – supercritical and supercooled. An accurate prediction of water's condensed phase properties in all these environments would demonstrate a degree of transferability displayed in no existing water model to date.

Further questions I will address in this thesis range from the orientation of water molecules at the liquid–vapour interface, the link between this orientation and the hydrogen bonding motifs present in the liquid, and the evolution of these motifs at water's limits of stability. I begin by an in-depth review of electronic coarse graining followed by an overview of the construction of an electronically coarse grained water model and a study of its properties in the four environments.

Chapter 2

Electronic coarse graining

Electronic coarse graining enhances the predictive power of molecular simulation allowing challenges in water physics to be addressed
Cipcigan, Sokhan, Crain, Martyna. J. Comp. Phys. 326 (2016).

2.1 Introduction

Simplified models of physical systems with complex emergent behaviour are at the heart of modern theories. Electronic coarse graining, pioneered by the work of Whitfield and Martyna [297], is one such approach applied to modelling materials. Electronic coarse graining is physically motivated, taking the molecule rather than the condensed phase as a starting point for the model, transferable, owing to a parametrisation unbiased to any thermodynamic state point, and computationally cheap, with a cost that can scale linearly with the number of molecules. The technique treats many-body polarisation and many-body dispersion on the same footing by representing electronic distributions of individual atoms and molecular moieties using a single coarse grained particle. This particle, known as a Quantum Drude Oscillator (QDO), consists of a *negative charge bound to a positive centre by a quantum harmonic oscillator*.

Designing theories for computers rather than for pencil and paper requires both new ways of thinking and new approaches to model building. QDOs are a physical approach to modelling intermolecular interactions for one main reason: they contain all long-range, many-body interactions to all orders. In

other words, QDOs do not truncate interactions to low order terms such as monopole and dipole, which is typical of classical strategies for dealing with polarisation and dispersion interactions. The absence of truncation reduces the assumptions inherent in modelling. The modeller does not need to pick the symmetry of the key terms in the interactions. Rather, the *environment* selects which interactions are important and which are not (Figure 2.1 illustrates the environmental selection in action for water). This type of simplified but rich model allows both the essential physics to emerge naturally and modellers to understand the molecular and electronic origins of this physics.

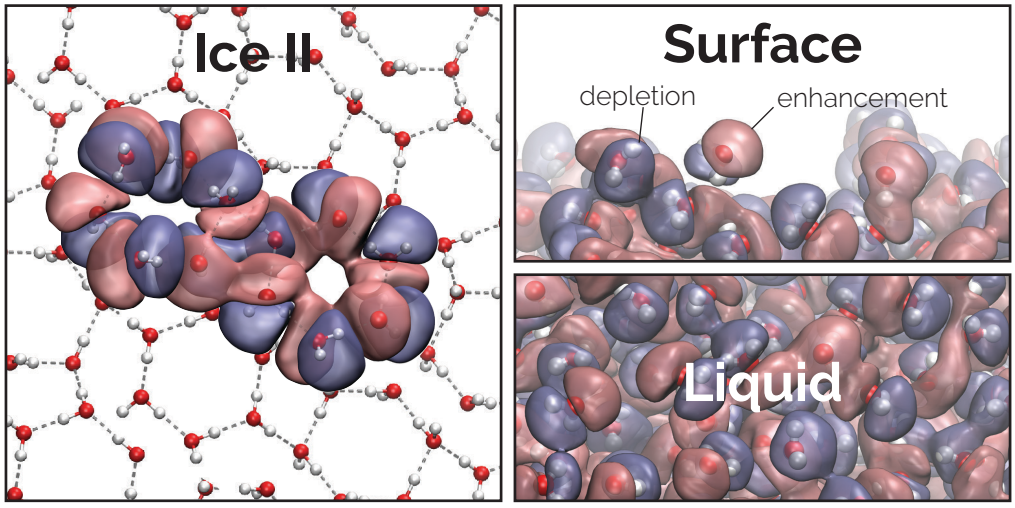

Figure 2.1 *Examples of Quantum Drude Oscillators in different environments: ice II, ambient temperature liquid water and the surface of liquid water. The images illustrate their electronic responses, with red and blue isosurfaces corresponding to regions of enhancement and depletion of electronic density, respectively.*

Since QDOs represent single molecule electronic responses (or more generally, responses of functional groups), their parametrisation involves molecular rather than condensed phase properties. We hypothesise that this parametrisation is sufficient for a condensed phase to naturally emerge from a limited set of single-molecule data. This means that QDOs, and in general physical models built with the same philosophy, are a faithful representation of individual molecules. This situation is in opposition to standard force field models, which: have limited responses, are typically constructed using a fixed charge distribution and two-body van der Waals terms, and are fitted to reproduce a limited set of condensed phase environments. With QDOs, the goal is to start with the intent of creating a

minimal model that behaves like a water molecule (meaning that its interactions approximate the real thing) and thus create a building block that can be then used to *predict* rather than just extrapolate. The ideal is that this approach can indeed say something new about the real thing.

Drude oscillators have rich history pre-dating our use in modelling intermolecular interactions. The earliest application dates back to London (1937) [168], who used them to derive from quantum mechanical calculations the $1/R^6$ functional form of the dispersion interaction between non-polar atoms and molecules. Earlier applications of Drude oscillators date back to the start of the 20th century when their eponym, Paul Drude, used their classical limit to understand the dispersion of light passing through insulators [70].

The 1950s to 1990s saw a revival of classical Drude oscillators [68, 177, 236, 261], which were employed in theory and simulation following the work of Cochran [56]. The quantum limit of the model served as an exemplar model for dispersion in the 1950s [109, 259], following London's initial calculations. It has been used to simulate xenon clusters by Martyna et al. [177] via an N^3 scaling method, to model electron attachment to water clusters via a Configuration Integral approach with a high order polynomial scaling by Wang et al. [289], served as an approximate treatment for dispersion of one valance electron systems by Fontana in 1961 [84], and even as a simplified model with which to calculate the quantum entanglement between base pairs in DNA [229].

In a series of papers beginning in 2006 [124, 126, 128, 297, 298], the tools to simulate the full model with order N [97] to $N \log N$ complexity (depending on the method used to treat long-range interactions) via non-perturbative path integral techniques were developed. Applications begun with rare gases [128, 297] and moved forward to liquid water [52–54, 123, 254, 255] – the latter being the focus of this thesis.

In related work during this period, the dipole-limit quantum model has been embedded within density functional theory (within the local density approximation) by Tkachenko et. al. [272] to treat many-body dipole dispersion beyond empirical potentials using the adiabatic connection formula [273]. This merger of embedded dipole-limit quantum oscillators and density functional theory lead to applications to heterogeneous systems such as benzene adsorbed onto metal surfaces [164] or DNA-graphene interactions [50].

2.2 Polarisation and dispersion

2.2.1 One dimensional model

To begin and gain intuition into how quantum Drude oscillators reproduce electronic responses, start by considering a simple model that formed the basis of London's early work on dispersion interactions [109, 168]: a negative charge $-q$ of mass m, free to move in a dimension x. The charge is localised by connecting it by a spring of frequency ω to a positive charge $+q$ fixed at the origin.

Now add a positive, fixed test charge Q at a distance $R \gg x$ from the positive origin. The system is in equilibrium when the Coulomb force Eq on the negative charge equals the spring force $m\omega^2 x$. Balancing the two forces results in the oscillator acquiring a dipole moment $\mu = qx = q^2E/(m\omega^2)$ and thus having a dipole polarisability of:

$$\alpha_1 := \frac{\mu}{E} = \frac{q^2}{m\omega^2}. \tag{2.1}$$

In order to account for dispersion effects, the system has to be treated quantum mechanically. Consider two identical oscillators separated by a distance R interacting via a term $c(R)$. The leading order interaction is dipole-dipole, meaning that $c(R)$ is proportional to R^{-3}. Thus, the Hamiltonian is:

$$\hat{H} = \frac{\hat{p}_1^2}{2m} + \frac{\hat{p}_2^2}{2m} + \frac{1}{2}m\omega^2\left(x_1^2 + x_2^2 + c(R)\,x_1x_2\right). \tag{2.2}$$

Changing coordinates to $\hat{\rho}_\pm = \frac{1}{\sqrt{2}}\left(\hat{p}_1 \pm \hat{p}_2\right)$ and $\xi_\pm = \frac{1}{\sqrt{2}}\left(x_1 \pm x_2\right)$ decouples the Hamiltonian into two independent harmonic oscillators of frequency $\omega\sqrt{1 \pm c}$.

$$\hat{H} = \left(\frac{\hat{p}_+^2}{2m} + \frac{1}{2}m\omega^2\left(1+c\right)\xi_+^2\right) + \left(\frac{\hat{p}_-^2}{2m} + \frac{1}{2}m\omega^2\left(1-c\right)\xi_-^2\right) \tag{2.3}$$

The ground state energy of the coupled system is, to leading order in c:

$$\begin{aligned} E_0 &= \frac{1}{2}\hbar\omega\left(\sqrt{1+c} + \sqrt{1-c}\right) \\ &\approx \hbar\omega\left(1 - \frac{1}{8}c^2 + O(c^3)\right). \end{aligned} \tag{2.4}$$

Fig. 2.2 shows the ground state probability distribution $\psi^2(x_1, x_2)$ in the

independent ($c = 0$) and correlated ($c > 0$) cases. When c increases, it becomes more probable for x_1 and x_2 to have the opposite sign and less probable for them to have the same sign. Since the energy is proportional to $\int dx_1\, dx_2\, \psi^2(x_1, x_2)\, x_1 x_2\, c(R)$, this correlation leads to the attractive force between two neutral molecules proportional to $-c(R)^2 \sim -R^{-6}$. This is the leading order term in a van der Waals interaction and is the reason the attractive part of the Lennard-Jones potential depends on R^{-6}.

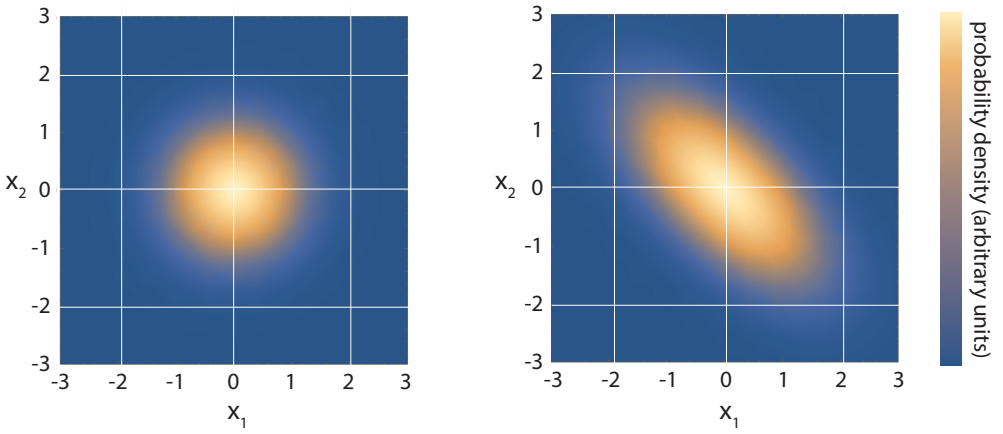

Figure 2.2 *The ground state probability density of two one dimensional quantum harmonic oscillators interacting via a $c(R)x_1x_2$ term. The units on the x_1 and x_2 axes are arbitrary. The left panel illustrates the non-interacting case, with $c(R) = 0$. The right panel illustrates the interacting case, with $c(R) > 0$. The spread of the wavefunction across the diagonal represents the electron correlation that gives rise to attractive van der Waals forces in real systems.*

This analysis shows that even a one dimensional quantum harmonic oscillator can capture the two basic features of long range forces: polarisation and dispersion, at least in the dipole limit. To capture the full set of interactions one has to consider the full three dimensional system.

2.2.2 Full quantum model

A Quantum Drude Oscillator (QDO) is made out of a light, negative particle of charge q connected to a heavy positive centre by a harmonic spring of frequency ω [297]. The bound state of this system is a drudon, with reduced mass m and Hamiltonian:

$$\hat{H} = \frac{\hat{\mathbf{p}}^2}{2m} + \frac{1}{2} m\omega^2 \mathbf{x}^2. \tag{2.5}$$

Perturbing this Hamiltonian via a point charge Q at a distance R gives a first order correction to the energy of zero and a second order correction of [128]:

$$E^{(2)}(R) = -\sum_{l=0}^{\infty} \frac{Q^2 \alpha_l}{2R^{2l+2}}, \tag{2.6}$$

where the polarisabilities α_l are given by

$$\alpha_l = \left[\frac{q^2}{m\omega^2}\right] \left[\frac{(2l-1)!!}{l}\right] \left[\frac{\hbar}{2m\omega}\right]^{l-1}. \tag{2.7}$$

Considering two QDOs separated by a distance R gives a first order correction to the energy of zero and a second order correction of [84, 128]:

$$E^{(2)}(R) = -\sum_{n=3}^{\infty} C_{2n} R^{-2n} \tag{2.8}$$

with

$$\begin{aligned} C_6 &= \frac{3}{4}\alpha_1\alpha_1\hbar\omega, \\ C_8 &= 5\alpha_1\alpha_2\hbar\omega, \\ &\dots \end{aligned} \tag{2.9}$$

Therefore, the full model has a complex and rich set of long range responses, which are replicated with only three parameters. This means the responses are correlated and thus one needs to check whether these correlations are satisfied in real atoms and molecules.

2.2.3 Invariant relationships between response coefficients

As the responses of QDOs depend only on three parameters, these parameters can be eliminated, resulting in the following invariants that can be used to verify

the accuracy of the QDO approximation [128]:

$$\begin{aligned} \sqrt{\frac{20}{9}}\frac{\alpha_2}{\sqrt{\alpha_1\alpha_3}} &= 1, \\ \sqrt{\frac{49}{40}}\frac{C_8}{\sqrt{C_6C_{10}}} &= 1, \\ \frac{C_6\alpha_1}{4C_9} &= 1. \end{aligned} \tag{2.10}$$

Comparing these ratios with the responses of real molecules gives the results shown in Fig. 2.3.

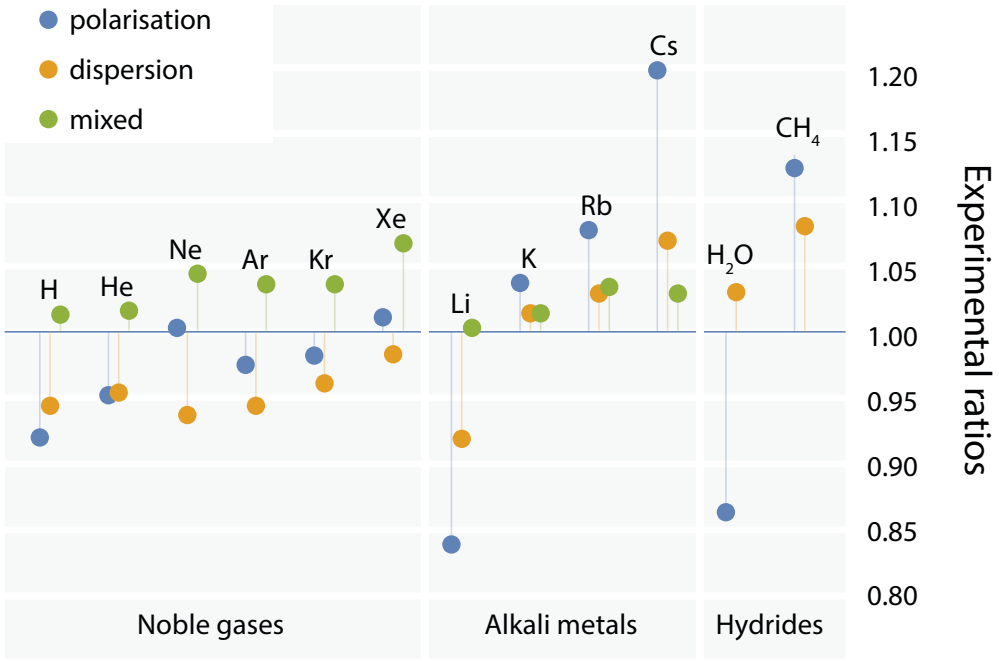

Figure 2.3 *Three types of invariant ratios between polarisation and dispersion coefficients, predicted by Quantum Drude Oscillators. Polarisation ratios involve only polarisabilities and analogously for dispersion ratios. Mixed ratios involve both polarisation and dispersion coefficients. Deviation from theory is shown for three types of atoms and molecules: noble gases, alkali metals and small hydrides. Adapted from Ref. [128].*

The agreement is good for the noble gases, with ratios within 10% of experiment, as their shells are fully filled and thus the distribution of electrons is nearly spherical. The agreement is also within 10% for most alkali metals, for which the last electron contributes mostly to polarisation. Small hydrides such as water and methane agree within 15%. This agreement is due to the electronegativity of atoms such as oxygen, which centres most of the electronic charge on them thus resulting in charge distributions and responses that are close to spherical. For example, the dipole polarisability tensor of water exhibits a 4% deviation from spherical symmetry.

The agreement shows that, in the case of the materials illustrated in Fig. 2.3, QDOs produce a dispersion and induction series that matches experiments and ab initio calculations. This agreement also means that, in real materials, the individual terms in these series are not independent, but related by symmetry constraints, with spherically symmetric materials having responses approximated well by a Gaussian model. However, a spherical model has its limitations. For instance, the dipole hyperpolarizability is identically zero due to the use of the on-site harmonic interactions. In order to move beyond the response of (approximately) spherically symmetric systems, more QDOs can be placed onto the molecular frame to break the symmetry.

2.2.4 Combining rules between dispersion coefficients

Knowing the link between the parameters of a QDO and its dispersion coefficients allows us to go beyond invariants and answer a question in molecular dynamics: how to determine the Lennard-Jones interaction parameters between two unlike species of atoms and molecules.

In practice the Lennard-Jones interaction parameters between different species are assigned using empirical combining rules – functional forms that result in reasonable estimates of the required parameters. Consider a Lennard-Jones interaction between two species i and j of the form:

$$V_{ij} = 4\epsilon_{ij}\left(\left(\frac{r}{\sigma_{ij}}\right)^{12} - \left(\frac{r}{\sigma_{ij}}\right)^{6}\right), \tag{2.11}$$

Two widely used rules to calculate σ_{ij} and ϵ_{ij} from σ_{kk} and ϵ_{kk} are:

1. Lorentz-Berthelot [31, 170]

$$\begin{aligned} \sigma_{ij} &= \frac{\sigma_{ii} + \sigma_{jj}}{2} \\ \epsilon_{ij} &= \sqrt{\epsilon_{ii}\epsilon_{jj}} \end{aligned} \tag{2.12}$$

2. Waldman-Hagler [288]

$$\begin{aligned} \sigma_{ij} &= \left(\frac{\sigma_{ii}^6 + \sigma_{jj}^6}{2} \right)^{\frac{1}{6}} \\ \epsilon_{ij} &= 2\sqrt{\epsilon_{ii}\epsilon_{jj}} \frac{\sigma_{ii}^3 \cdot \sigma_{jj}^3}{\sigma_{ii}^6 + \sigma_{jj}^6} \end{aligned} \tag{2.13}$$

QDOs on the other hand have combing rules which depend directly on the parameters of species A and B [128]:

$$\begin{aligned} C_6^{AB} &= \frac{3}{2}\alpha_1^A \alpha_1^B \frac{\hbar\omega_A\omega_B}{\omega_A + \omega_B} \\ C_6^{A} &= \frac{3}{4}\alpha_1^A \alpha_1^A \hbar\omega_A \\ C_6^{B} &= \frac{3}{4}\alpha_1^B \alpha_1^B \hbar\omega_B, \end{aligned} \tag{2.14}$$

where α_1^i is the dipole polarisation and ω_i is the QDO frequency of species i.

To compare these relationships with the classical empirical ones, begin by eliminating the product $\alpha_1^A\alpha_1^B$ by writing it as a function of the dispersion coefficients:

$$\sqrt{C_6^A C_6^B} = \frac{3}{4}\alpha_1^A \alpha_1^B \hbar\sqrt{\omega_A\omega_B} \tag{2.15}$$

This gives the mixed dispersion coefficient as:

$$C_6^{AB} = 2\frac{\sqrt{C_6^A C_6^B}}{\sqrt{\omega_A\omega_B}} \frac{\omega_A\omega_B}{\omega_A + \omega_B} = 2\sqrt{C_6^A C_6^B} \frac{\sqrt{\omega_A\omega_B}}{\omega_A + \omega_B} \tag{2.16}$$

In the case of the Lennard-Jones potential, $C_6^{ij} = 4\epsilon_{ij}\sigma_{ij}^6$. Substituting in (2.16):

$$C_6^{AB} = 2\sqrt{4\epsilon_{AA}\sigma_{AA}^6 4\epsilon_{BB}\sigma_{BB}^6} \frac{\sqrt{\omega_A\omega_B}}{\omega_A + \omega_B} \tag{2.17}$$

After rearranging,

$$C_6^{AB} = 8\sqrt{\epsilon_{AA}\epsilon_{BB}}\left(\sigma_{AA}^3\sigma_{BB}^3\right)\frac{\sqrt{\omega_A\omega_B}}{\omega_A+\omega_B} \tag{2.18}$$

Since we don't know the form of either ϵ nor σ, this is as far as we can go for QDOs. Can a similar relationship be derived using the empirical rules? Start by calculating C_6^{AB} using the Waldman-Hagler rules:

$$C_6^{AB} = 4\epsilon_{AB}\sigma_{AB}^6 = 8\left(\sqrt{\epsilon_{AA}\epsilon_{BB}}\frac{\sigma_{AA}^3\cdot\sigma_{BB}^3}{\sigma_{AA}^6+\sigma_{BB}^6}\right)\frac{\sigma_{AA}^6+\sigma_{BB}^6}{2} \tag{2.19}$$

Simplifying,

$$C_6^{AB} = 8\sqrt{\epsilon_{AA}\epsilon_{BB}}\left(\sigma_{AA}^3\sigma_{BB}^3\right)\frac{1}{2} \tag{2.20}$$

The two forms for C_6^{AB} are identical except for the coefficient

$$\Lambda_{AB} := \frac{\sqrt{\omega_A\omega_B}}{\omega_A+\omega_B}. \tag{2.21}$$

When $\Lambda_{AB} = \frac{1}{2}$, corresponding to $\omega_A = \omega_B$, the two become identical.

This result gives us an insight into the pairs of species for which the Waldman-Hagler rules work best: it's those with similar QDO frequencies. These frequencies are related to the properties of the outermost electronic shell (those are the electrons that have the most contribution to polarisation), meaning that these combining rules should be valid for elements having similar outermost shells.

Figure 2.4 shows the values of Λ_A as predicted by QDOs between three different types of species: alkali metals, noble gases and simple hydrides. Two predictions emerge. First, the Waldman-Hagler rules apply well to atoms and molecules from the same type. So, noble gases combine well with other noble gases, alkali metals with alkali metals and hydrides with hydrides. Second, Second, alkali metals do not combine well with noble gases nor with hydrides. However, hydrides and noble gases combine surprisingly well with each other.

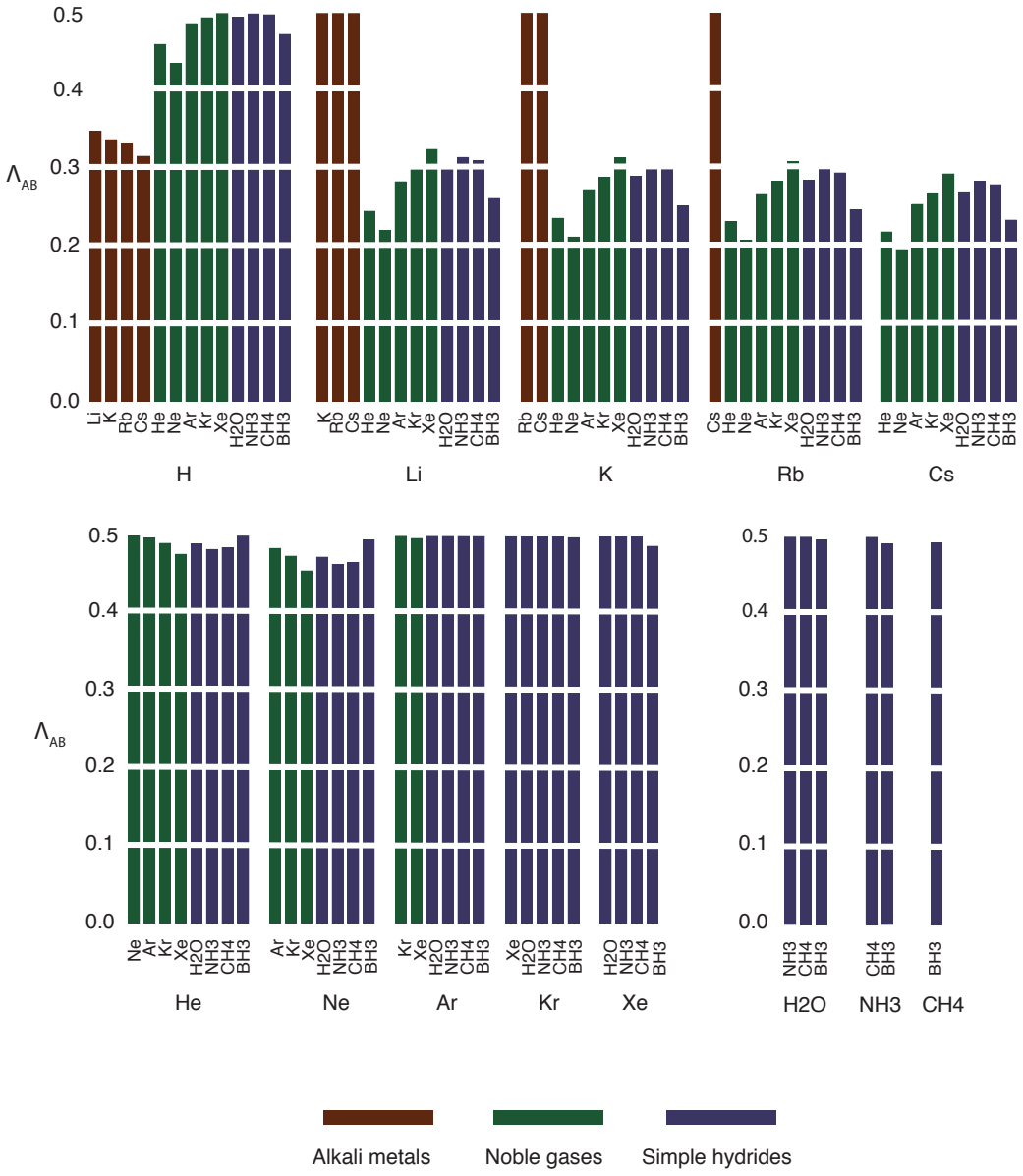

Figure 2.4 *Λ_{AB} calculated form the QDO parameters [128] for various combinations between alkali metals, noble gases and simple hydrides.*

2.2.5 Parametrisation of the full quantum model

The responses of a QDO can be inverted to give its properties as a function of the responses. The relevant relations, used to parametrise a QDO are: [128]

$$\omega = \frac{1}{\hbar}\frac{4C_6}{3\alpha_1^2}, \tag{2.22}$$

$$m = \frac{\hbar}{\omega}\frac{3\alpha_1}{4\alpha_2} \quad \text{or} \quad m = \frac{\hbar}{\omega}\frac{5C_6}{C_8}, \tag{2.23}$$

$$q = -\sqrt{m\omega^2\alpha_1}. \tag{2.24}$$

The resulting parameters are displayed in Table 2.1 and plotted in Figure 2.5. A similar trend arises to what has been seen when discussing the combining rules. Similar species have similar parameters, with exception of hydrogen, which behaves different from all group I elements. There is in general a larger variation of the parameters between the different categories than within a single one. This is indicative of the fact that only the outer-most electron contributes significantly to polarisation and dispersion. Hydrides and noble gases (with the exception of hydrogen) have $q > 1$ which indicates the fact that there is more than one electron in the outer shell. However, q is still close to a single electron's charge, varying between $\sim 0.7\,e$ for hydrogen to $\sim 1.4\,e$ for xenon. This indicates that most of the contribution from polarisation comes from the excitation of a single valence electron. Since group I metals only have a single electron in their unfilled shell $q < 1$, as expected.

Species	$\omega/(E_h/\hbar)$	m/m_e	q/e
H	0.4273	0.6099	0.708
Li	0.0687	1.2545	0.9848
K	0.063	0.8101	0.967
Rb	0.0603	0.7343	0.9274
Cs	0.0531	0.6939	0.895
He	1.0187	0.5083	0.8532
Ne	1.2965	0.3491	1.2494
Ar	0.7272	0.302	1.3314
Kr	0.6359	0.2796	1.3741
Xe	0.5152	0.2541	1.357
H_2O	0.6287	0.3656	1.1973
NH_3	0.5603	0.3541	1.2722
CH_4	0.5794	0.2615	1.2313
BH_3	0.8776	0.1165	1.0793

Table 2.1 *The QDO parameters for various species determined using the QDO parametrisation rules, reproduced from Jones et al [128]. $E_h \approx 27.211\,eV$ is the Hartree energy, $m_e \approx 9.11 \times 10^{-31}\,kg$ is the mass of an electron and $e \approx 1.60 \times 10^{-19} C$ is the electron charge. All of these parameters are electronic in magnitude, with the Hartree energy being twice the ionisation energy of a hydrogen atom.*

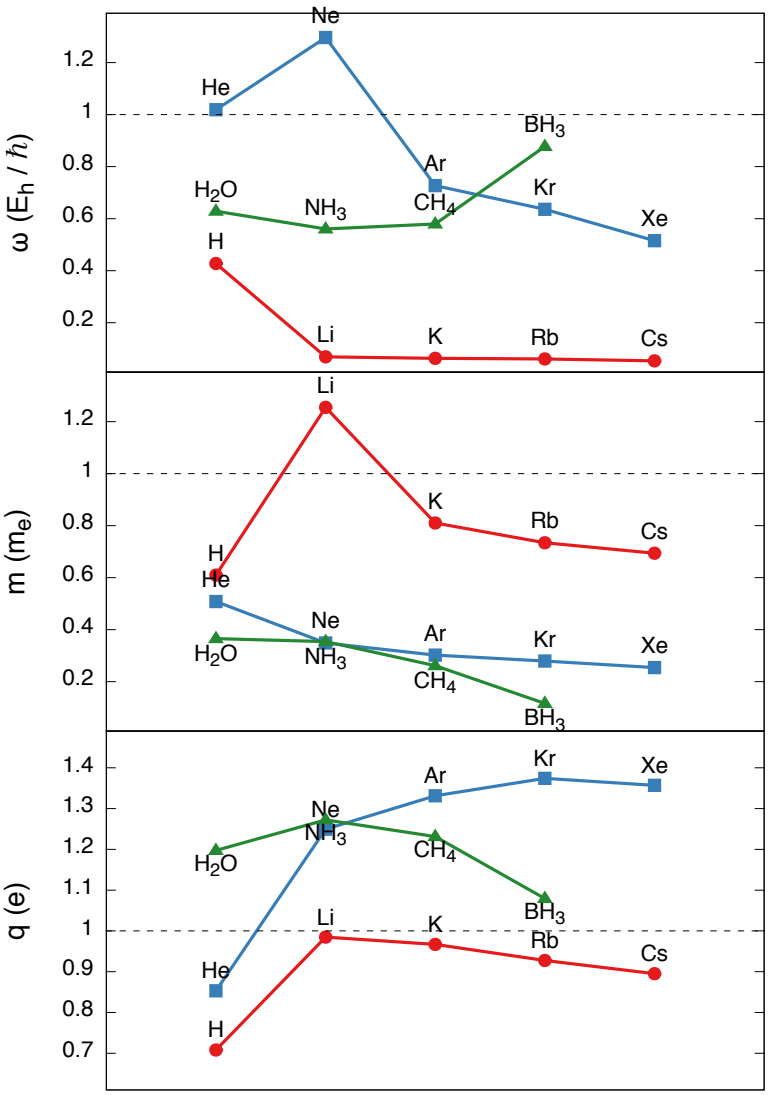

Figure 2.5 *QDO parameters [128] for various noble gases, first row metals and simple hydrides. We expect the model to work well for such insulators, where tight binding type models motivate the QDO coarse graining.*

2.3 Simulating Quantum Drude Oscillators via two temperature path integral molecular dynamics

Path integral molecular dynamics, shortened to PIMD, is a method of sampling a quantum mechanical partition function using classical methods [124, 203, 278, 298]. For bosons or systems of distinguishable particles (such as QDOs), this method achieves a statistical sampling of the quantum state at finite temperature in a way that can scale linearly with the number of particles. If the temperature is sufficiently low with respect to the lowest excitation, PIMD samples predominantly the electronic ground state.

Consider a quantum mechanical system (such as electrons in a potential defined by the Born-Oppenheimer surface of a nuclear configuration), with degrees of freedom $\vec{x}$. The state of this system is described by a density matrix $\rho(\vec{x}, \vec{x}'; \beta_D)$. The partition function at inverse temperature $\beta_D = 1/kT_D$ is thus [80]:

$$Z(\beta_D) = \operatorname{tr} e^{-\beta_D \hat{H}} = \int \mathbf{d}\vec{x}\, \rho(\vec{x}, \vec{x}; \beta_D), \tag{2.25}$$

where $\mathbf{d}\vec{x}$ represents a small volume element in the $\dim(\vec{x})$-dimensional space spanned by the system's degrees of freedom. Since we are interested in the ground state electronic surface of insulators, the inverse temperature β_D associated with the electronic degrees of freedom is taken as large as possible while ensuring the ground state dominates the statistics. For harmonic systems, $\beta_D \hbar\omega > 8$. In general, for insulators of interest to us, $T_D \gg T$.

Since the density matrix is an exponential of the Hamiltonian, it can be factorised into higher temperature (smaller $\tau = \beta_D/P$) slices to give the following path integral representation,

$$Z(\beta_D) = \prod_{i=1}^{P} \int \mathbf{d}\vec{x}_i\, \rho(\vec{x}_i, \vec{x}_{i+1}; \beta_D/P). \tag{2.26}$$

The factorisation is done because a higher temperature (thus a lower τ) results in a more classical density matrix, which is easier to approximate. Thus, the aim is to use the smallest β_D (or largest electronic temperature) that keeps the system close to the ground state.

The next step is to approximate the high temperature density matrices using a

Trotter factorisation [276, 298], where the Hamiltonian $\hat{H}$ is split into a reference $\hat{H}_0$, with known density matrix $\rho_0 = e^{-\tau \hat{H}_0}$, and a perturbation $V(\vec{x})$ such that:

$$\rho(\vec{x}, \vec{x}'; \tau) \approx e^{-\tau V(\vec{x})/2} \rho_0(\vec{x}, \vec{x}'; \tau) e^{-\tau V(\vec{x}')/2} + O(\tau^3). \tag{2.27}$$

In the case of QDOs it is convenient to set H_0 as the Hamiltonian of the isolated oscillator, with the following reference density matrix:

$$\rho_0(\vec{x}, \vec{x}'; \tau) = \left[\frac{\alpha_P(\tau)}{\pi}\right] \exp\left[\alpha_P(\tau)(\vec{x} - \vec{x}')^2 + \frac{\lambda_P(\tau)}{2}(\vec{x}^2 + (\vec{x}')^2)\right]. \tag{2.28}$$

and coefficients $\alpha_P(\tau)$ and $\lambda_P(\tau)$ defined as:

$$\begin{aligned} \alpha_P(\beta) &= \frac{m\omega}{2\hbar \sinh(f)}, \\ \lambda_P(\beta) &= \frac{2m\omega \tanh(f/2)}{\hbar}, \\ f &= \frac{\beta\hbar\omega}{P} \end{aligned} \tag{2.29}$$

In order to motivate sampling schemes, we notice the strong nearest-neighbour coupling between the coordinates $\vec{x}$ and $\vec{x}'$. To treat this coupling, the density matrix is diagonalised to the independent coordinates $\vec{u}_i$ via a staging transformation with unit Jacobian [298], leading to the following form for the partition function:

$$\begin{aligned} Z(\beta_D) &= \prod_{i=1}^{P} \int \mathbf{d}\vec{x}_i \, \rho_0(\vec{x}_i, \vec{x}_{i+1}; \tau) \times \exp\left(-\tau \sum_{i=1}^{P} V(\vec{x}_i)\right) \\ &= \prod_{i=1}^{P} \int \mathbf{d}\vec{u}_i \underbrace{\left(\frac{1}{2\pi\sigma_i^2}\right)^{3N/2} \exp\left(-\frac{\vec{u}_i^2}{2\sigma_i^2}\right)}_{\text{staging coordinates}} \times \underbrace{\exp\left(-\tau \sum_{i=1}^{P} V(\vec{x}_i(\vec{u}_i))\right)}_{\text{external potential}}. \end{aligned} \tag{2.30}$$

The coefficients of the transformation as as follows:

$$\begin{aligned}
\vec{u}_1 &= \vec{x}_1, \\
\vec{u}_i &= \vec{x}_i - \vec{x}_i^*, \\
\vec{x}_i^* &= \frac{\sinh(\tau\hbar\omega)}{\sinh[i\tau\hbar\omega]}\vec{x}_1 + \frac{\sinh((i-1)\tau\hbar\omega)}{\sinh(i\tau\hbar\omega)}\vec{x}_{i+1}\,, \\
x_{P+1} &= x_1 \\
\sigma_1^2 &= \frac{\hbar}{2m\omega\tanh(\beta\hbar\omega/2)}\,, \\
\sigma_i^2 &= \frac{\hbar\sinh[(i-1)\tau\hbar\omega]\sinh(\tau\hbar\omega)}{m\omega\sinh[i\tau\hbar\omega]}\,.
\end{aligned} \tag{2.31}$$

One step remains in order to make the partition function isomorphic to a fictitious classical system: the addition of conjugate momenta $\vec{p}_i$ with corresponding faux masses $\tilde{m}_i$. This transforms the partition function to:

$$\begin{aligned}
Z(\beta_D) = &\prod_{i=1}^{P}\int \mathbf{d}\vec{u}_i \left(\frac{1}{2\pi\sigma_i^2}\right)^{3N/2} \exp\left(-\frac{\vec{u}_i^2}{2\sigma_i^2}\right) \times \exp\left(-\tau\sum_{i=1}^{P} V(\vec{x}_i(\vec{u}_i))\right) \\
&\times C\int \mathbf{d}\vec{p}_i \exp\left(-\tau\frac{\vec{p}_i^2}{2\tilde{m}_i}\right),
\end{aligned} \tag{2.32}$$

were $C = \prod_i \left(\frac{2\pi\tilde{m}_i}{\tau}\right)^{-\frac{3}{2}}$ is a normalisation constant required to make the momentum integral unity. This final transformation generates a form for the partition function with the effective classical Hamiltonian $H^{(\text{faux})}$, which can be sampled via existing methods used to sample classical systems [278, 297, 298].

$$H^{(\text{faux})} = \sum_{i=1}^{P}\frac{\vec{p}_i^2}{2\tilde{m}} + \frac{\vec{u}_i^2}{2\sigma_i^2\tau} + \frac{V(\vec{x}_i(\vec{u}_i))}{P}. \tag{2.33}$$

When adding the motion of the nuclei, the adiabatic principle needs to be invoked and the fictitious mass $\tilde{m}$ of the the electronic degrees of freedom selected such that they evolve on a time scale a factor of γ smaller than that of the nuclear degrees of freedom. This selection of masses results in two effects: it allows the electronic degrees of freedom to be thermostatted at a higher temperature than the nuclei, and reduces energy transfer between the hot electrons and cold nuclei, allowing the dynamics of these two subsystems to be evolved simultaneously [124, 278, 297, 298]. Further energy transfer between the two subsystems can be

reduced by using an adaptive thermostat that dissipates excess heat induced by Brownian motion [126]. It is important to recognize that the canonical ensemble must be generated for the electronic degrees of freedom (and thus the need for a thermostat) in order for the model to have physical meaning, since the path integral method is explicitly derived to sample the canonical ensemble.

The computational cost of sampling the effective classical Hamiltonian depends on the method used to treat long-range interactions. In molecular dynamics, this can be done using Particle Mesh Ewald summation [65] for an $O(N \log N)$ method or cell multipole methods for an $O(N)$ method to treat long-range interactions [97].

2.4 A note on software

The results that follow were produced using QDrude 2, a custom software of our group that is used to simulate interactions between Quantum Drude Oscillators. The software was written by Dr. Andrew Jones during his thesis [125] before development was taken over by Dr. Vlad Sokhan and Prof. Glenn Martyna. The following features are available:

1. The ability to simulate two classes of molecules, independently of each other: water or noble gases. The QDO parameters for noble gases are given in Table 2.1 while those for water are discussed in the next chapter.

2. Two different sampling algorithms: Norm Conserving Diffusion Monte Carlo (DMC) [127] with fixed nuclei and Path Integral Molecular Dynamics (PIMD) [297, 298] with either fixed or moving nuclei.

3. Two thermodynamic ensembles for PIMD: NVT (isochoric-isothermal) and NPT (isobaric-isothermal). The temperature is kept constant using multiple Adaptive Nosé-Hoover chain thermostats [126] applied to both the nuclear and bead degrees of freedom. The thermostats are designed to dissipate the excess heat transferred from the bead to the nuclear degrees of freedom.

4. Parallelism over both atomic and bead degrees of freedom for PIMD. Parallelism over the independent walkers used to sample the ground state distribution for DMC. Both are implemented using MPI.

5. Treatment of long range interactions via Particle Mesh Ewald [65] summation, giving a scaling of $O(N \log N)$
6. Separation of timescales using the RESPA algorithm [277].
7. The following outputs: pressure tensor, trajectory, energy (multiple low variance estimators [298]), density and, multipole moments of the simulation box and molecular multipole moments.

The resulting trajectories were analysed using the trajectory analysis software `qdrude-analysis`, which I wrote for this thesis and is available on my repository at `bitbucket.org/flaviu/qdrude-analysis`. It totals around 7500 lines of Scala code and can calculate the following quantities:

1. Radial distribution functions
2. Potential of mean force
3. Instantaneous and average density, dipole moment and charge density profiles through a simulation box
4. Probability of hydrogen bonding motifs
5. Molecular orientation distributions
6. Nearest neighbour distance statistics at the surface of the liquid
7. Polarisation density
8. Order parameters: tetrahedrality and local structure index
9. The probability distribution of the nearest neighbours

Chapter 3

An electronically coarse grained model of water

Electronically coarse-grained model for water
Jones, Cipcigan, Sokhan, Crain, Martyna. PRL 110 (22) 2013.

Water is the simplest complex liquid. Its condensed phase behaviour is essential for both life on Earth and for creating environmentally friendly technologies. Its dynamics and thermodynamics are challenging to simulate, with hundreds of molecular models of water, employing various degrees of physics – from all-electron simulations of small water clusters [8, 93, 94, 173, 248, 269], to DFT simulations of small periodic systems [12, 92, 95, 162, 238, 241] to fixed-charge empirical models [1, 55, 98, 118, 119, 281, 283, 284] and coarse grained simulations where each water molecule is treated as a single particle [172, 178, 184, 245, 282, 286, 313]. These simulations have given us insights into how water's condensed phase properties emerge from its molecular structure, emphasising the importance of the competition between the tetrahedral structure favoured by hydrogen bonds and the close-packed structure favoured by dispersion interactions. The balance between these two environments, one driven by polarisation and one driven by dispersion, combined with the lack of a near-quantitative molecular model for such an important substance inspired the creation of QDO-water, a molecular model of water using Quantum Drude Oscillators.

3.1 Why water?

In the beginning there was water The Earth formed 4.5 billion years ago [62]. Shortly after its formation, Earth already had water. We know this from the faint traces it left onto fossilised rocks. Ancient zircon crystals dated back to 4.4 billion years ago [300] have ratios of oxygen-18 to oxygen-16 that indicate they formed when hot magma was cooled by a cold liquid ocean. Traces of water droplets can even be seen as tiny craters onto sediments, the shape of which can be used to estimate the speed of the droplets and thus the density of the atmosphere [256].

Water as a biomolecule From its formation, through the transition from unicellular to multicellular life and the subsequent evolution to terrestrial lifeforms, water has played an essential role in supporting life.

Shortly after the earliest oceans, life formed. Zircon crystals dated 4.1 billion years ago [24] have ratios of carbon-12 to carbon-13 consistent with the existence of life. The initial spark for the creation of the earlies biomolecules was given by lighting [180] or sunlight [220] , which provided the energy to synthesize them from their basic constituents: hydrogen, oxygen and carbon.

As life evolved, it became encoded by DNA, whose double helical shape is stabilised by surrounding water molecules [7]. The resulting proteins, synthesized as chains of amino acids from the genetic code of the DNA, are again supported by the presence of water molecules. The process through which these amino acid chains fold into their functional form is driven by their hydrophobic and hydrophilic patches. The energy landscape of folding resembles a funnel, with a stable ground state and an abundance of local minima on the way to this ground state. The location of the ground state and the smoothness of the path to it are both determined by the presence of water. Indeed, without water, the energetic funnel has an abundance of intermediate metastable minima, which lengthen the process of folding [57].

As life evolved to multicellular organisms, water become important not just for the structure of an organism but for its function. For example, plants use water as a source of hydrogen [20], splitting it using the energy of incident sunlight.

Water as a tool Fast-forward to our era, water is becoming increasingly important in the creation of environmentally friendly technologies.

Learning a lesson from nature, water can be used as a way of storing solar energy. Plants use the splitting of water as a step in the process of converting sunlight into organic molecules, prehistoric forms of which come to us in the form of coal and petrol. As our energy consumption is now far greater than what the planet can renew each year, we must invent technologies that speed up the process of converting sunlight into energy. The prospects are however promising: the energy needs of a person for a year can be satisfied by splitting a single pool full of water into oxygen and hydrogen [60, 265].

Water can also be employed at the molecular level in catalysing chemical reactions. One of the most striking example is the speed-up of the Diels-Alder cycloaddition at the surface of water, caused by the dangling hydrogen bonds present there [194]. Another example is the production of Cl_2 from chlorofluorocarbons (CFCs), responsible for the depletion of ozone in the stratosphere. The reaction that produces molecular chlorine, Cl_2, from hydrochloric acid and chlorine nitrate is catalysed by the surface of ice particles from of polar stratospheric clouds [274].

Understanding how water influences life and how to use that influence to create new technologies relies on tools to understand the structure and dynamics of water at the molecular level. Computer simulations are a powerful such tool, giving us a virtual microscope into the physics of water. The accuracy of this microscope is determined by the models used, which, for water, can at times prove challenging.

3.2 Existing water models

Water's structure arises due to a competition between directional hydrogen bonds, which favour an open ice-like local structure and van der Waals forces, which favour a close-packed local structure. This competition makes modelling of water challenging since many-body polarization and dispersion interaction are key to distinguishing the dominant motifs [188].

Hydrogen bonds are known to be cooperative, meaning that their interaction strength changes depending on environment thus leading to the emergence of a wide variety of motifs. A simple reporter of this cooperation is the molecular dipole moment, which changes from a value of 1.85 D in the gas phase to an

estimated value of 2.5–3.6 D in the condensed phase [123, 136], where four hydrogen bonded motifs are dominant.

Dispersion interactions are also important in water. Including these responses is essential to generate even the basic structure of water at room temperature. An illustrative example of this balance is the overstructuring of room-temperature water by local approximations to DFT [162], where including the electron correlations that lead to accurate van der Waals interactions is absent (although, there have been promising results using the similar technique of embedded quantum harmonic oscillators at the dipole level [272]).

In addition, three-body effects account for as much as 25% of the binding energy of water, according to the estimates of Ojamaee and Hermansson calculated at the MP2 counterpoise-corrected level of theory [199]. Thus, monatomic two-body potentials for the water molecule can only reproduce water's condensed phase properties if their parameters are allowed to vary with state point [47, 122]. Even a full-atom description of water cannot be transferable if its electrostatics is fixed. Vega and Abascal [280] showed that a nonpolarisable model of water cannot simultaneously reproduce the melting temperature and temperature of maximum density.

With these considerations about the structure of water, let's look at the modelling approaches that have been used and their successes and places where they can be improved.

What distinguishes all approaches of simulating water is how much physics to include at which level of theory. Ab initio simulations include the effects of electrons (at least the valance ones when pseudopotentials are used) while empirical models go via one guiding principle: reproduce short-ranged structure by using long-range classical potentials. Further approximations can be done by limiting the interaction between particles to short-ranged potentials and even discarding the structure of the water molecule and replacing it with a single particle.

3.2.1 Water from the quantum up: ab initio models of water

Ab initio simulations of water are challenged by the computational expense of treating electron correlation accurately. This limits the simulations to small

clusters [93, 94, 173]. Nonetheless, recent advances such as the use of embedded fragments [96] have enabled accurate coupled cluster calculations to be applied to the condensed phase [303].

In the case of Density Functional Theory (DFT), local, gradient corrected (such as PBE) and hybrid functionals (such as B3LYP) all overstructure liquid water [162], with a melting point of around 400 K [311]. To achieve a more realistic structure dispersion interactions have to be included, using techniques such as van der Waals corrected functionals [139, 302], the Tkatchenko-Scheffler embedded oscillators method [237, 271, 272] or hybrid functionals [27].

Despite the challenge, ab initio simulations revealed interesting insights into the physics of water. Cluster-based simulations are important in creating accurate benchmarks for the parametrisation of empirical models [173] and could even be used to interpret ultrafast experiments using nanodroplets consisting of a few thousand water molecules. DFT simulations are essential in interpreting experimental results of x-ray spectroscopy, which probes the change in electron ionisation energies as a function of different environments [10, 197]

Ab initio simulations also reveal insights about the nature of the hydrogen bond. For example, DFT simulations show, via an energy partition scheme, that water molecules have on average one strong acceptor and one strong donor bond, uncovering a fluctuating asymmetry in water's local structure [143].

3.2.2 Fixed charge models

The majority of simulations of water models have used an approach where water molecules are modelled as a combination of three elements: fixed point charges arranged to reproduce the electrostatic moments of the molecule, Lennard-Jones R^{-6} interactions to reproduce dispersion and an R^{-12} or exponential repulsion. This approach is conceptually simple, computationally cheap and has reproduced the bulk properties of liquid water with good accuracy.

Such models can be characterised by the number of interaction sites, ranging from three to six, as summarised in Figure 3.1. A few years after resolving the molecular structure of water, Bernal and Fowler [30] proposed the first molecular model of water. It was a four-site model, resembling the now well-known TIP4P family, with two positive charges placed on the hydrogen atoms and a negative

charge on the bisector of the HOH angle.

Computer simulation of water begun in the late 60s to early 70s, with Barker and Watts [21] and Rahman [216] performing the first Monte Carlo and molecular dynamics simulations of liquid water. The 80s saw the creation and parametrisation of an increasing number of water models. Some followed the philosophy of Bernal and Fowler [30] and employed four interaction sites, leading to the TIP4P family of models [129]. Others used only three sites, leading to the TIP3P [129] and SPC [28] families. Others created a model incorporating the lone pair orbitals, resulting in five interaction sites and the ST2 family of models [262].

The 2000s saw an increase in optimised parametrisations of these families of models, seeing the birth of models such as TIP4P/Ew [113], optimised for use with Ewald summation techniques, TIP4P/Ice [3], optimised to reproduce the phases of ice and TIP4P/2005 [1], optimised to give the best overall fit to the whole phase diagram of water.

All of these models assume that the interaction sites need to be placed on atomic sites. However, this choice is not optimum for reproducing the ground state electrostatic properties of real water. Recently, Izadi et al. [119] has shown that relaxing this assumption leads to a better reproduction of the electrostatic moments of the water molecule and to two models, OPC (4-site) and OPC3 (3-site) that achieve a better fit to liquid water's condensed phase properties than the TIP4P and TIP3P families.

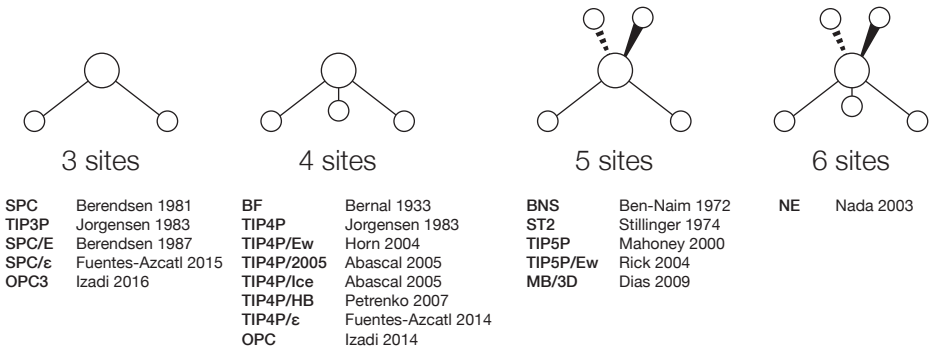

Figure 3.1 *Various parametrisations of classical, rigid, fixed-charge models using three sites [28, 29, 88, 118, 129], four sites [1, 3, 30, 87, 113, 119, 129, 205], five sites [26, 69, 174, 226, 262] and six sites [191]. The figure was inspired by a presentation given by Molinero [183].*

Models such as OPC have reached the limit of what is achievable with fixed charge models. In order to go further in both reproducing the properties of bulk water and those of water in heterogeneous environments, two other effects are to be taken into consideration: polarisation and flexibility.

3.2.3 Including the effects of polarisation and flexibility

Empirical models are great for reproducing the effects of bulk water. However, they fail to provide a realistic representation of the water molecule, since they do not include electronic effects such as polarisation, many-body dispersion and molecular flexibility.

These effects become important far from the region of parametrisation and in heterogeneous environments. For example, a non-polarisable water model cannot reproduce simultaneously the temperature of maximum density and melting temperature [283], likely due to the increased molecular dipole moment in the ice phase. Polarisation also enhances order at the surface of C_{60} fullerene [51] and the structure of water molecules around proteins [25], where the local environment quickly alternates between polar and nonpolar regions.

Including polarisation to water models has been done using four main approaches: fluctuating charges [225, 228], charge-on-a-spring models [18, 148, 152, 312], point polarisable multipoles [4, 38, 63, 211, 223, 290] and hybrid approaches that mix the three components [77, 227, 262].

Recent attempts to add polarisation to existing potentials, resulted in models such as TIP4P-pol [49] and SWM4-NDP [151]. However, these early attempts did not improve considerably over existing fixed charge models [98]. This lack of improvement could be caused by the inaccurate electrostatic field produced by the model being amplified by the polarisation. Further attempts parametrised models independently of a pre-existing reference, using methods such as ab initio calculations. This resulted in a better replication of the properties of real water.

Another way of bringing molecular models closer to real water is to include flexibility [307]. However, this can also prove tricky. The vibrational frequencies of real water are high, meaning that the intramolecular vibrations retain a quantum character even at room temperature. The qualitative predictions of classically flexible models, such as a decrease of the HOH angle in the liquid

phase differ from those of real water, where the HOH angle actually increases due to partial charge transfer through the hydrogen bond [217]. This explains the prevalence of rigid models, which is a strategy also adopted in the development of QDO-water. This approach can be rationalized by noting that the entropy of water's bend and two stretch modes is close to zero, like in a rigid model.

3.2.4 Many-body effects

All the models discussed so far are based on two-body interactions, namely electrostatic forces between fixed charges and R^{-6} Lennard-Jones interactions to model dipole-dipole dispersion. In real substances, three- and many-body forces can give significant contributions to the energies. Indeed, as we've already seen, 25% of the binding energy of water comes from three-body effects, which consist of a combination of polarisation and many-body dispersion. Hermann et al. [105, 106] arrive at a similar estimate for the binding energy of water clusters using a coupled-cluster many-body expansion of the interaction energy. Further, by decomposing the energy into electron correlation and Hartree–Fock components, they show that the Hartree–Fock energy does have a significant three-body contribution, while the correlation energy can be decomposed into two-body terms. This result seems to justify the traditional approach in modelling water, where many-body terms are introduced via polarisation while dispersion interactions are limited to two-body Lennard–Jones terms. However, the authors considered a limited number of clusters comprising 7 water molecules. These clusters are not necessarily representative of all environments of water molecules in the liquid state.

In rare gas crystals, where long range forces are purely dispersion, the binding energies change by 6-10% when three-body dispersion is considered [230]. More complex systems also show strong many-body effects. Around 50% of the binding energy of bilayer graphene is three-body, with some biomolecules having 10–20% of their binding energy being three-body [285].

Atomistic simulations don't usually consider these many-body forces. All widely used, nonpolarisable, water models are two-body effective potentials. Same is true for biomolecular force fields. The main reason is computational cost – three body effective potentials such as the Axilrod–Teller dispersion [16] are conceptually easy to understand but computationally expensive to implement.

3.2.5 Ab initio parameterised potentials

Instead of fitting a potential to the *condensed phase* properties of water, one can fit to the energies of clusters and test whether such an approach generalises to the liquid. Such an approach requires including at least dipolar polarisation to be effective. Hypotheses range from traditional charge-based models [5] to neural network potentials attempting to reproduce the many-body potential energy surface of water [187]. These potentials typically match the target parametrisation but are limited by the accuracy of the ab initio method used to generate the training set and to the environments included in the training set.

3.2.6 Dismissing long-range interactions

Rather than optimise for quantitative agreement, another approach is to optimise for computational cost while still keeping the universal properties of water's structure, such as its tetrahedral structure.

One limiting factor in simulations is the inclusion of long-range interactions. These interactions can be removed without affecting the qualitative results. This leads to potentials such as the short-ranged three- and four-site water models [120]. Taking this approach further leads to the removal of intramolecular structure, such as done with the mW potential [184], where every molecule is replaced by a single particle with short-ranged interactions that favour a tetrahedral structure. These fast potentials are typically employed to study phenomena that depend on rare events and thus need long sampling times, such as freezing of supercooled water [185], which requires crystal nucleation.

3.3 A new water model based on Quantum Drude Oscillators

Quantum Drude Oscillators (QDOs) unite the missing elements from fixed charge models into a single framework. They reproduce closely the electrostatic responses and many-body dispersion interactions between molecules at a computational cost that scales near-linearly with the size of the system. Thus, QDOs can provide the missing building block to water models that brings their properties in near-quantitative agreement to those of real water.

To construct a water model using a QDO, one needs three elements: a rigid molecular frame with embedded point charges to replicate the lowest order electrostatic moments, a QDO to replicate electronic responses and a short-range, pairwise repulsion potential to treat Pauli repulsion. These elements are shown in Fig. 3.2 with their respective parameters given in Table 3.1.

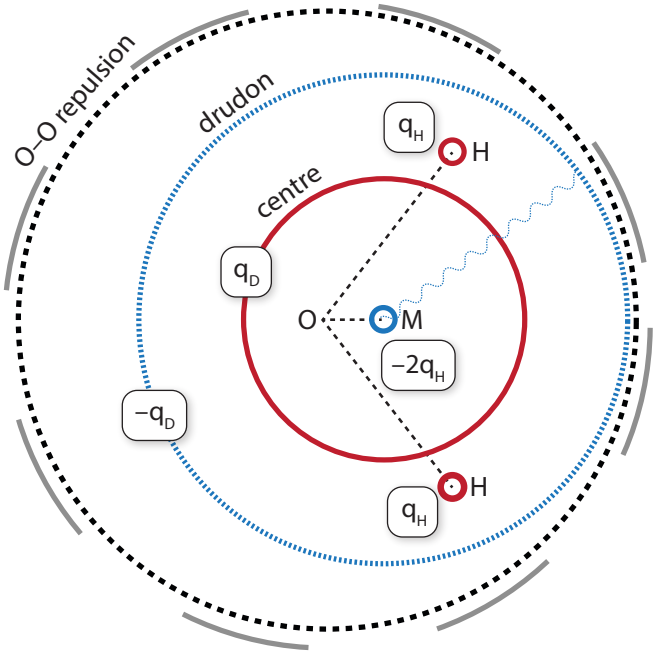

Figure 3.2 *Schematic of QDO-water.*

Parameter	Value	Parameter	Value
Molecular geometry		**Coulomb damping**	
R_{OH}	0.9572 Å	$\sigma_D = \sigma_H = \sigma_M$	$0.1\,a_0$
$\angle$HOH	104.52°	σ_C	$1.2\,a_0$
Ground state electrostatics		**Short range repulsion**	
q_{H}	$0.605\,e$	κ_1	$613.3\,E_h$
R_{OM}	0.2667 Å	λ_1	$2.3244\,a_0^{-1}$
Quantum Drude Oscillator		κ_2	$10.5693\,E_h$
m_{D}	$0.3656\,m_e$	λ_2	$1.5145\,a_0^{-1}$
ω_D	$0.6287\,E_h/\hbar$		
q_{D}	$1.1973\,e$		

Table 3.1 *The free parameters of QDO-water. $E_h \approx 27.211\,eV$ is the Hartree energy, $a_0 \approx 0.5292\,Å$ is the Bohr radius and $e \approx 1.60 \times 10^{19}\,C$ is the electron charge*

Frame The frame is fixed in the experimental molecular geometry of the isolated molecule, with an HOH angle of 104.52° and an OH distance of 0.9572 Å[1]. Two positive charges of magnitude $q_{\mathrm{H}} = +0.605\,e$ are placed on the H site and a negative $-2q_{\mathrm{H}}$ charge placed on the M site, on the bisector of the HOH angle at a distance $R_{\mathrm{OM}} = 0.2667$ Å from the oxygen. The distances and the charges are fixed to generate the dipole moment of the isolated molecule (1.85 D) and give the best fit to the quadrupole moment components.

QDO To create a responsive model, a QDO is centred on the M site. Its parameters are determined using the dipole and quadrupole polarisabilities and the C_6 dispersion coefficient using equation (2.24) on page 14. The reference values of the multipole moments and dispersion coefficients are taken from Millot et al. [181], who report a mix of ab-initio calculations and experiment.

Repulsive potential The repulsive potential is fit by calculating one slice through the dimer energy surface using the coordinates shown in Figure 3.3. The calculation was done at the CCSD(T) level, with the aug-cc-pVTZ basis set using ACESIII 3.0.7 [171] giving the energy shown in Figure 3.3. The equivalent energy of the repulsion-free model (frame + QDO) was calculated using norm-conserving diffusion Monte Carlo with 1000 walkers. The difference between ab initio energies and repulsion-free model were fit to a double exponential $\phi^{(rep)}(r) = \kappa_1 e^{-\lambda_1 r} + \kappa_2 e^{-\lambda_2 r}$.

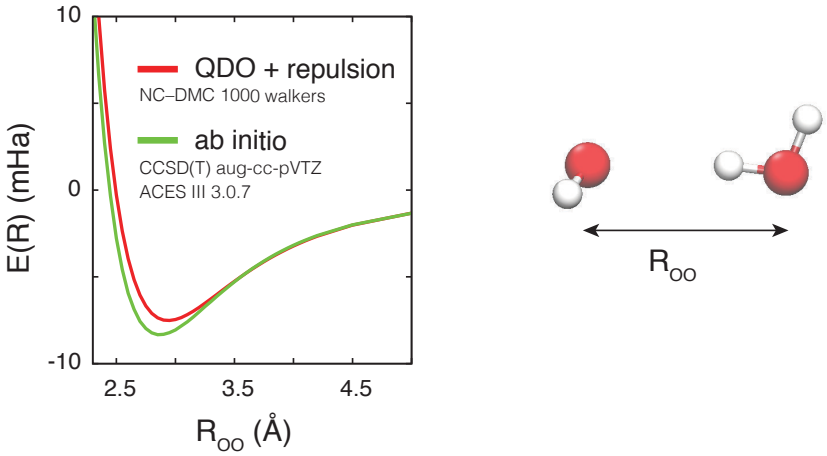

Figure 3.3 *(left) A cut through the dimer energy surface calculated via ab initio methods (CCSD(T) aug-cc-pVTZ ACES III 3.0.7) and frame + QDO + repulsion (norm-conserving diffusion Monte Carlo with 1000 walkers). Figure reproduced from Sokhan et al. [255]. (right) The coordinates used to calculate the cut through the dimer energy surface.*

Coulomb damping In order to avoid unphysical energies associated with a diverging interaction, the Coulomb potential between two charges was regularised by replacing it by a Gaussian distribution of width σ_i. This is equivalent to damping the Coulomb potential using an erf function:

$$\sigma_{12}^2 = \sigma_1^2 + \sigma_2^2 \tag{3.1}$$

$$\phi(r_{12}) = \frac{q_1 q_2 \,\mathrm{erf}(r/\sqrt{2}\sigma_{12})}{r} \tag{3.2}$$

The Gaussian widths of each charge are given in Table 3.1. For the bead (the PIMD sampler), hydrogen and M site they are 0.1 Bohr radii, small in comparison to the dimensions of the molecule. For the centre charge of the QDO, the Gaussian width is 1.2 Bohr radii, which is comparable with the size of the molecule. This choice was done so that the centre charge provides a background of positive charge inside the molecule, making the ground state of the QDO more uniformly neutral and reproducing some of the screening.

3.4 Cluster energies of QDO-water: a basic benchmark

In order to assess how the energetics of QDO-water extrapolate beyond the single cut through the dipole energy surface, a simple quantity to calculate is the energies of various water clusters. The reference energies and geometries were taken from the Benchmark Energy and Geometry DataBase [224] and were calculated at the CCSD(T)/CBS noCP level of theory by Temelso et al. [269], which is a comparable level of theory to what was used to parametrise the model.

Since the reference geometries were optimised via ab initio calculations (at the MP2/aug-cc-pVDZ noCP level of theory), they had to be adapted to fit the rigid frame of QDO-water. To do so, the oxygen atom of QDO-water was placed in the position of the oxygen atom in the reference geometry. The bisector of the model's frame was then aligned with the bisector of the reference geometry and the positions of the hydrogen atoms were then generated. The model's hydrogen atoms were close to the reference ones, with the OH distances changing by a few percent. This is consistent with a fairly rigid OH bond. The rearrangement had to be done since the energetics of QDO-water were parametrised with reference to a fixed geometry. The ab initio energies were not recomputed and hence quantitative agreement cannot be expected.

Figures 3.4 to 3.7 shows a comparison of the binding energies per molecule for 38 clusters between QDO-water and ab initio calculations. The agreement between QDO-water and ab initio is excellent. The energies differ by few percent, with 68% of the QDO-water clusters having energies 2% away form the ab initio reference and almost all (97%) with an energy 5% away from the ab initio reference. The only large deviation was the 3UUU trimer, where all of the three hydrogen are pointing in the same direction, with a deviation of 9.3%. It would be interesting to add the CP correction to the ab initio results and estimate the contribution of 3-body repulsion, which is neglected in the QDO model.

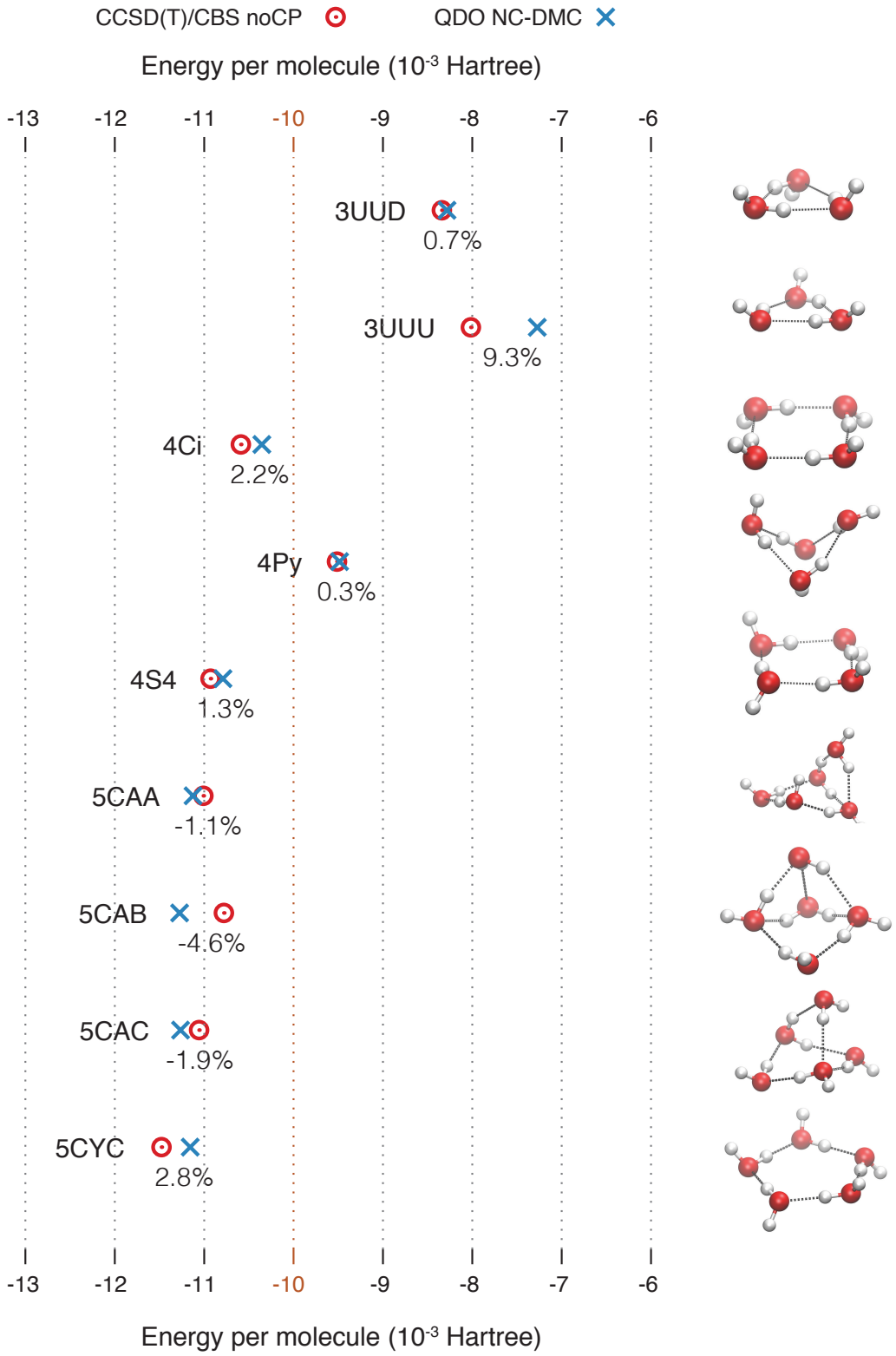

Figure 3.4 *(multipart figure 1/4) Energies per molecule of water clusters calculated using QDO-water, compared with a CCSD(T)/CBS noCP reference [224, 269]. Note that the axes in the first two parts of this figure are different than in the last two parts. The change in position of the orange line at 10 mHartree indicates this change.*

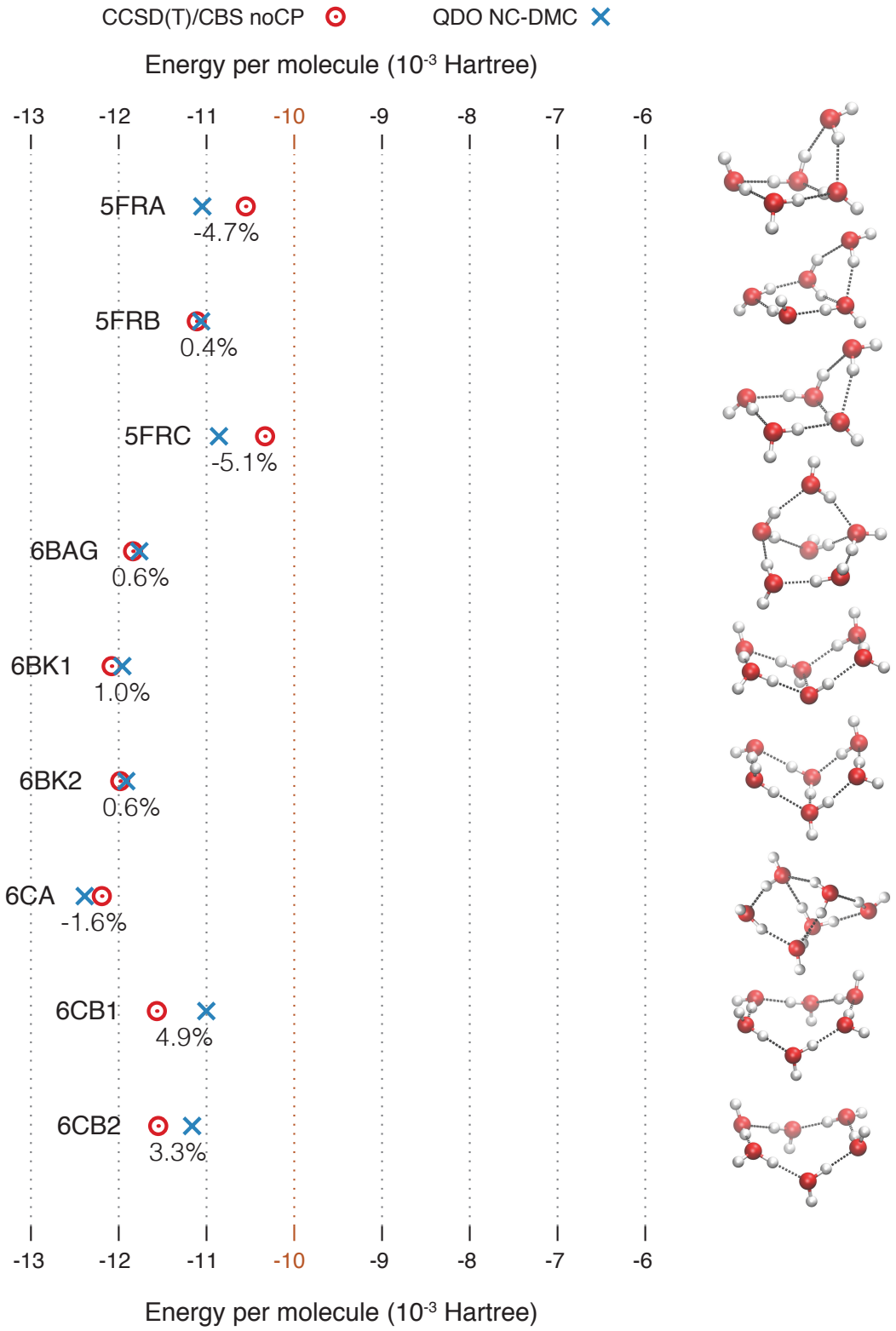

Figure 3.5 *(multipart figure 2/4) Energies per molecule of water clusters calculated using QDO-water, compared with a CCSD(T)/CBS noCP reference [224, 269]. Note that the axes in the first two parts of this figure are different than in the last two parts. The change in position of the orange line at 10 mHartree indicates this change.*

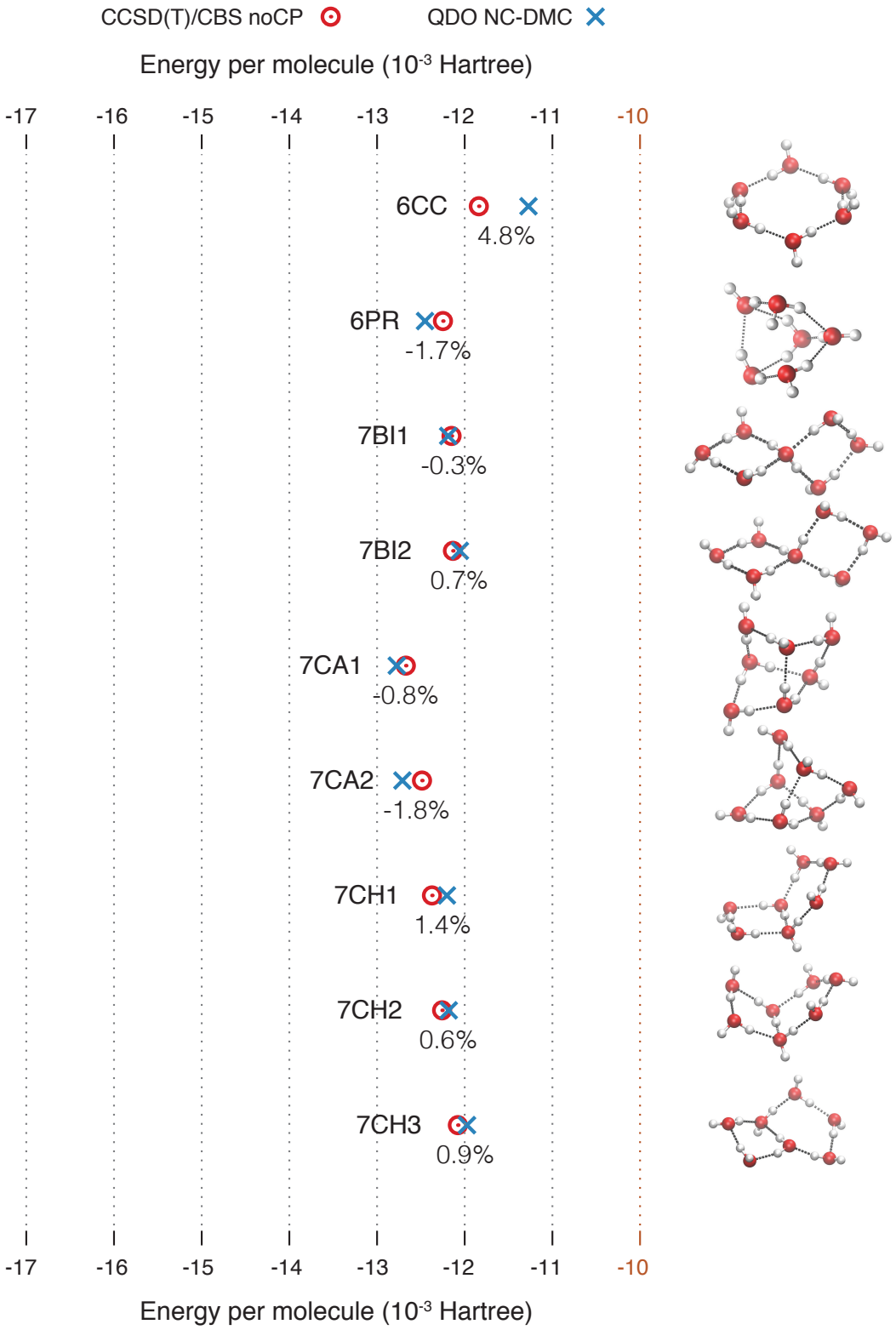

Figure 3.6 *(multipart figure 3/4) Energies per molecule of water clusters calculated using QDO-water, compared with a CCSD(T)/CBS noCP reference [224, 269]. Note that the axes in the first two parts of this figure are different than in the last two parts. The change in position of the orange line at 10 mHartree indicates this change.*

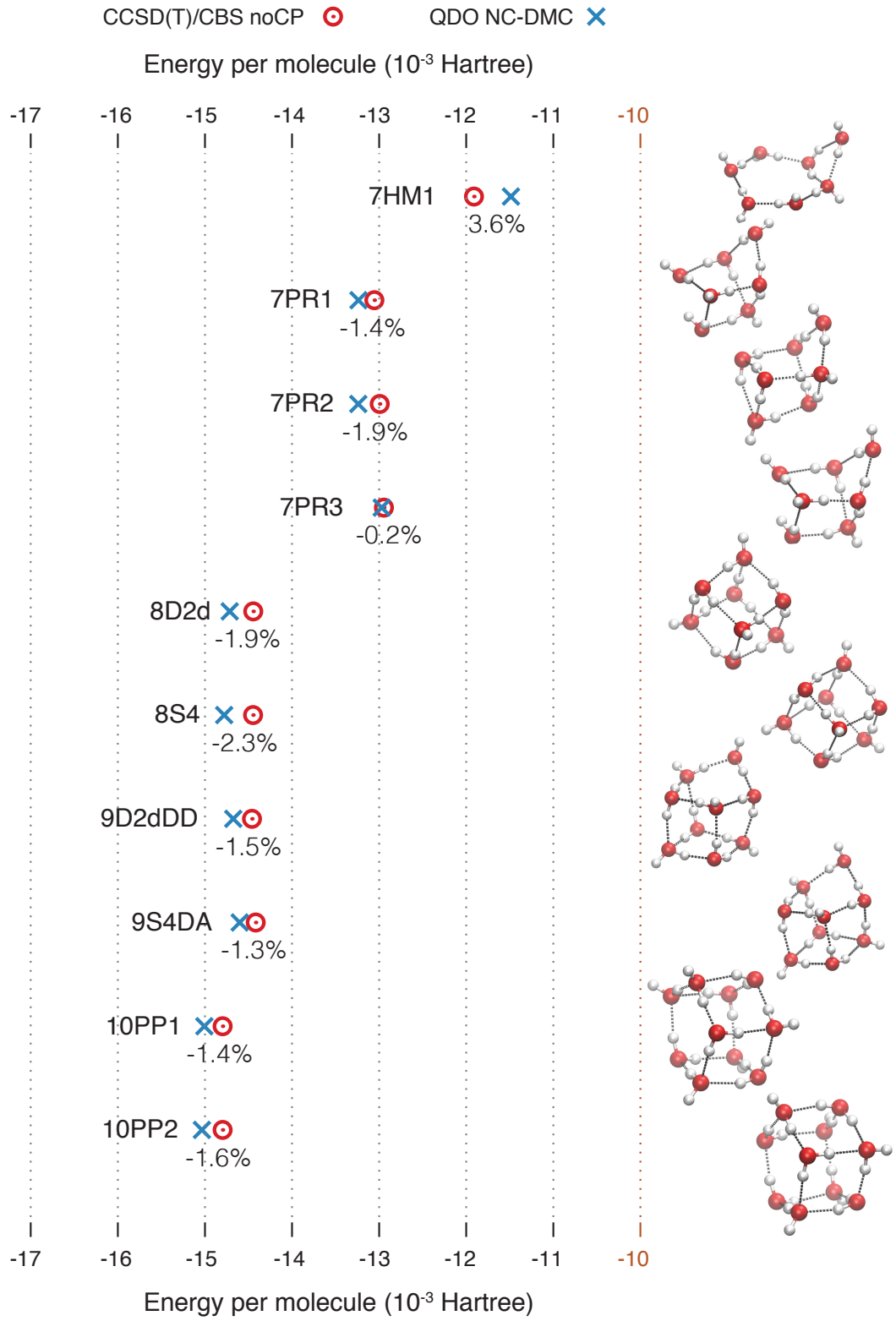

Figure 3.7 *(multipart figure 4/4) Energies per molecule of water clusters calculated using QDO-water, compared with a CCSD(T)/CBS noCP reference [224, 269]. Note that the axes in the first two parts of this figure are different than in the last two parts. The change in position of the orange line at 10 mHartree indicates this change.*

Chapter 4

Ice II: low pressure proton ordered ice

Signature properties of water: Their molecular electronic origins
Sokhan, Jones, Cipcigan, Crain, Martyna. PNAS 112 (20) 2015.

4.1 A quick tour of ice phases

Water is unique on Earth since it is abundant in all three phases: ice, liquid and vapour. Ice covers 10% of Earth's surface [252] and plays an important role in regulating the climate, reflecting Sun's rays and thus cooling the ground it covers. Ice is also an exquisite archive of the atmosphere's past, trapping air bubbles as it freezes and preserving them for possibly millions of years. The best source of these ancient bubbles is Antarctica. Its ice cap formed 44.5 million years ago [74] and is over three kilometres thick. The oldest ice drilled there dates back to 800,000 years ago [15] and lead to the reconstruction of a complete climate record from that time to today. Other regions of Antarctica contain fragments of ice more than one million years old [32] and modelling has identified possible sites with ice cores spanning the past 1.5 million years [81].

Ice found on Earth is predominantly a single phase:[1] ice Ih, formed from open motifs of hydrogen-bonded water molecules arranged in a tetrahedral cage. At high pressures, the same tetrahedral motifs remain, but the cages arrange in an assortment of phases [23, 206], summarised in Figure 4.1.

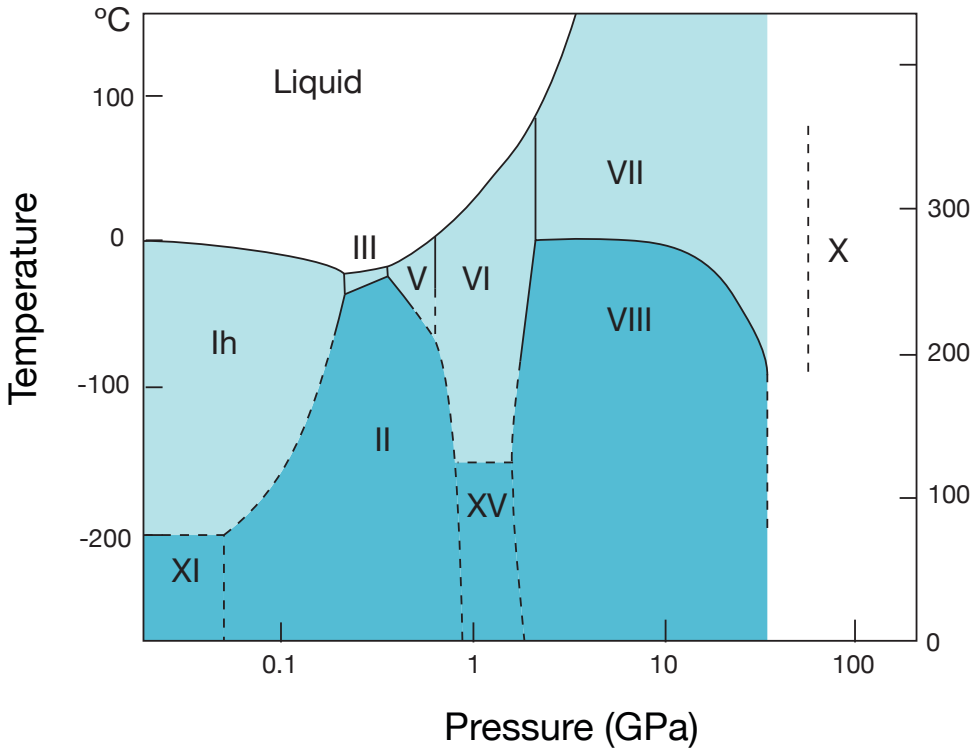

Figure 4.1 *The phase diagram of stable ice phases, adapted from Bartels-Rausch et al. [23]. Light blue regions mark proton-disordered ices (where the hydrogen atoms are free to move according to the Bernal-Fowler ice rules [30]). Dark blue regions mark proton-ordered ices, where the hydrogen atoms are on fixed lattice sites. Ice X is symmetric – the protons are half-way between two oxygen atoms. The pressure axis is logarithmic. Dashed lines are approximate phase transition boundaries.*

At atmospheric pressure, terrestrial ice (ice Ih) is formed. The slope of the transition line in the pressure-temperature plane is negative, reflecting ice Ih's lower density than liquid water's. Ih is interesting among solids since it is proton-disordered: while the oxygen atoms are fixed to lattice sites and have four tetrahedrally-coordinated neighbours, the hydrogen atoms can arrange in

[1] At least as a first approximation. Ice Ic is a metastable cubic form of ice Ih that may be found in high clouds. Furthermore, ices have trapped air bubbles (that give them the milky colour) and various crystal defects.

any configuration that preserves the bonds and the geometry of the molecule (satisfying what are known as the Bernal-Fowler rules [30]). This increased entropic contribution makes Ih stable at relatively high temperatures. The proton-ordered form of ice Ih is ice XI [153], which only becomes stable below 72 K. Ice XI is called so due to the historical convention put forward by Bridgman [37] of naming ice phases in the order of their discovery.

Increasing the pressure generates four more proton-ordered phases each occupying the following approximate pressure ranges: ice III [37, 169, 266] (300 MPa to 500 MPa), V [37, 166] (500 MPa to 1.1 GPa), VI [132, 146] (1.1 Gpa to 3 GPa) and VII [121, 140, 146] (3 GPa to $\sim$ 60 GPa). Each of these phases has a proton-ordered sibling, occupying a similar pressure range: VII proton orders into VIII [146, 195, 295] and VI into XV [235]. However, despite what the phase diagram might suggest, V and III do *not* order into II. Ice II is a distinct, proton-ordered crystal structure [131] that has no experimentally known disordered phase. Simulations suggest that the proton-disordered ice II, ice IId, would only be favoured at temperatures above the melting point of ice III and V and thus thermodynamically unstable with respect to the liquid [193]. Instead of ice II, the proton-ordered siblings of V and III are XIII [233] and IX [169] respectively; both are metastable with respect to ice II.

XIII and IX are not the only metastable forms of ice. Proton-disordered ice XIV [233] and its proton-ordered sibling ice XII [233] are both metastable in the ice V–VI region of the phase diagram, being formed at around 800 MPa. Ice IV [234] and Ic [179] are two further metastable ices, with no known ordered form. Ice IV is metastable in the III–V–VI pressure range and ice Ic in the Ih pressure range.

Alongside crystalline metastable ices, water can also be vitrified by cooling the liquid quickly, depositing the vapour on a cold plate or quickly pressurising ice Ih [89]. Vapour deposition and fast cooling at atmospheric pressure create low density amorphous ice (LDA), with a glass transition temperature of around 160 K. Increasing the pressure of either LDA or Ih to around 0.20 GPa creates high density amorphous ice, with what looks to be a first order transition between the two phases. Recently, a third form of amorphous ice has also been proposed: very high density amorphous (VHDA), formed at pressures of around 1.15 GPa and having a seemingly continuous transition from HDA [89].

Metastable forms of ice also occur in two other situations: at negative pressure and as a precursor for freezing into stable counterparts. Simulations have

proposed a two-step process for homogeneous nucleation of supercooled water into ice Ih and Ic, where a new metastable form of ice, ice 0, acts as a precursor for the stable ice phases [232]. At negative pressure, simulations proposed that empty clathrates might be the preferred solid phases [58, 116]. This has been recently put to the test by emptying clathrates and recovering the resulting ice phase, resulting in the synthesis of the first negative pressure ice: ice XVI [76].

Extremely high temperatures and pressures may also yield exotic phases of ice. The only such phase known is ice X [176]: a symmetric ice, with hydrogen atoms lying in the middle of the line separating two neighbouring hydrogen atoms.

From the assortment of ice phases, I chose to concentrate on one as an initial application of QDO-water: ice II. It is proton-ordered, removing the need for sampling the slow dynamics linked with proton disorder. It is also stable in a balanced region of the phase diagram, with relatively high temperature and low pressure, thus increasing the chance for well-equilibrated sampling. Finally, ice II is a favourite of modellers, being one of the ices used in parametrising models such as TIP4P/2005 [1]. All these attributes made ice II the first step in testing the transferability across water's phase diagram of QDO-water, a model parametrised using no condensed phase data.

4.2 Ice II

4.2.1 Structure

Ice II is a proton ordered ice with the structure illustrated in Figure 4.2. Its unit cell consists of two hexagonal rings with distinct hydrogen bonding motifs [131]. These rings are staggered and connected by hydrogen bonds both vertically and horizontally, resulting in a structure resembling nanotubes of water molecules. The structure is determined by two parameters: a is proportional to the size of each ring and c is proportional to the separation between the rings.

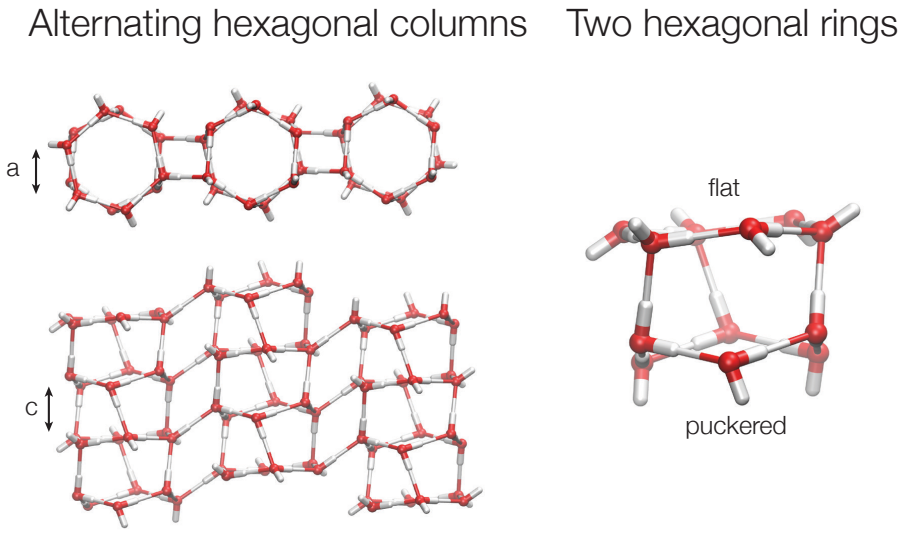

Figure 4.2 *The unit cell of ice II and the resulting hexagonal columns of the condensed phase. The unit cell is defined by two rings, flat and puckered, arranged in a stacked pattern.*

The primitive cell of ice II has 12 molecules and is rhombohedral with parameters (at $T = 123$ K and $P \sim 0$ GPa) [131]:

$$a = b = c = 7.78\text{Å} \quad \alpha = \beta = \gamma = 113.1^\circ \tag{4.1}$$

The simulation cell contained 3×3×3 primitive unit cells with 324 water molecules in the TIP4P geometry (same geometry as QDO-water); note that the OH length and HOH angle does change in ices versus the liquid by a few percent [296], but this change cannot be captured by a rigid model. The simulation cell was obtained from Buch et al. [40, 41]. Its parameters are:

$$a = b = c = 23.34 \text{ Å} \quad \alpha = \beta = \gamma = 113.1^\circ \tag{4.2}$$

The box matrix, containing the unit cell vectors as columns, is then [138]:

$$\begin{aligned} h_0 &= \begin{pmatrix} a & b\cos\gamma & c\cos\beta \\ 0 & b\sin\gamma & -c\cos\alpha^*\sin\beta \\ 0 & 0 & 1/c^* \end{pmatrix} \\ c^* &= \frac{bc\sin\alpha}{V} \\ \cos\alpha^* &= \frac{(\cos\beta\cos\gamma - \cos\alpha)}{\sin\beta\sin\gamma} \\ V &= abc\sqrt{1 + 2\cos\alpha\cos\beta\cos\gamma - \cos^2\alpha - \cos^2\beta - \cos^2\gamma} \end{aligned} \tag{4.3}$$

This box matrix uses the convention where the x axes of both the crystal and cartesian coordinate systems coincide. Substituting $a = b = c$ and $\alpha = \beta = \gamma$ gives h_0 as:

$$h_0 = \begin{pmatrix} a & a\cos\alpha & a\cos\alpha \\ 0 & a\sin\alpha & a\frac{\cos\alpha^2 - \cos\alpha}{\sin\alpha} \\ 0 & 0 & a\frac{\sqrt{1-3\cos\alpha^2+2\cos alpha^3}}{\sin\alpha} \end{pmatrix} \tag{4.4}$$

4.2.2 Experimental benchmarks

Ice II was first discovered in 1900 by Tammann [266]. The first detailed x-ray study was performed by Kamb [131] who used the displacement in the position of the oxygen atoms to deduce that ice II was proton-ordered, being the first confirmed example of a proton-ordered ice.

The 90s led to more diffraction experiments such as those of Gagnon et al. [91], Lobban et al. [165] and Fortes et al. [86]. Together, they provide the density of ice II versus pressure at 237.65 K, 200 K and 225 K, for pressures up to 0.5 GPa. The isotherms corresponding to these experiments are shown in Figure 4.3.

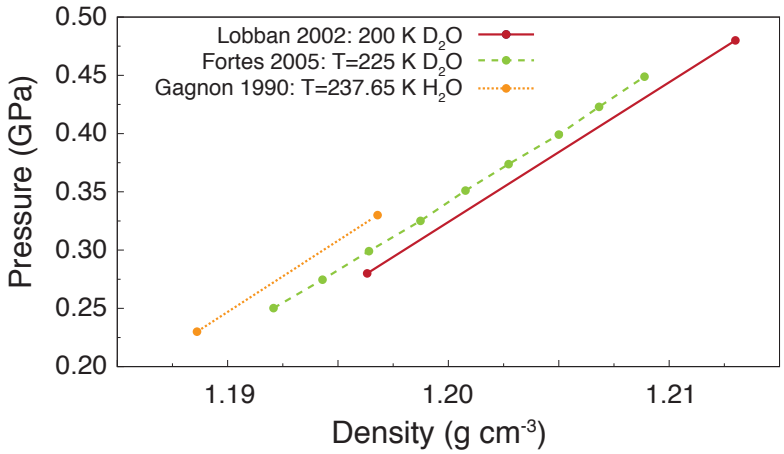

Figure 4.3 *Experimental isotherms of ice II at three temperatures: 200 K [165], 225 K [86] and 237.65 K [91]. The first two experiments were performed on D_2O samples while the latter used H_2O.*

In order to compare the four density measurements with the atmospheric pressure isobar reported by Fortes et al. [86] and the single atmospheric pressure point reported by Kamb [131], the measurements of Gagnon et al. [91] and Lobban et al. [165] were fit using a linear and Birch-Murnaghan functions [33, 190], with the results plotted in Figure 4.4.

There is a considerable spread of measurements: the density reported by Kamb [131] and the one calculated from his lattice constants are considerably lower than those of Fortes et al. [86] (even if the former are used to parametrise some empirical models). This be caused by the isotope effect, as Kamb used H_2O while Fortes et al. [86] used D_2O. However, Gagnon et al. [91] also used H_2O and his value is *higher* than the extrapolation of the results of Fortes et al. [86]. Another effect that will increase the uncertainty of the measured density is the absorption of helium. The open channels of ice II are large enough for a helium atom to penetrate, which will affect the structure, as discussed by Lobban et al. [165]. However, the measurement of Gagnon et al. [91] used dioctyl sebacate as a pressuring medium [90] since it's a gas that does not form clathrates with ice, so the measurements should not suffer from this problem.

Given the spread in measurements, the data provided by Fortes et al. [86] will be used as a reference in this work since it is the most recent and most comprehensive dataset and it provides lattice constants in addition to densities. The only caveat with this dataset is its isotope effect – the authors used D_2O ice.

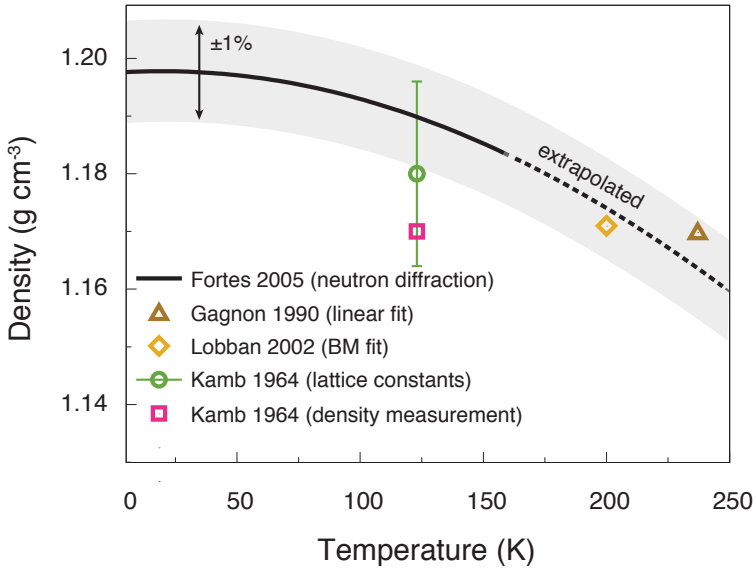

Figure 4.4 *Experimental densities at atmospheric pressure of ice II as a function of temperature. The solid grey line marks the measurements of Fortes et al. [86] performed on D_2O ice II. The dashed line is an extrapolation of these measurements while the grey band marks a region within 10% of the experiments of Fortes et al. [86]. The square and circle mark the experiments of Kamb [131] using direct measurement of the density (square) and an estimation from the measured lattice constants (circle). The rest of the points are estimates of the atmospheric pressure density in the experiments of Gagnon et al. [91], Lobban et al. [165] by using a linear interpolation or a Birch-Murnaghan (BM) fit [33, 190].*

4.3 Results

4.3.1 Isotherms and bulk modulus

A simulation cell of ice II prepared as described in Section 4.2.1 was sampled in the NVT ensemble at the three temperatures with available experimental data: 123 K, 200 K and 237.65 K. The resulting pressures as a function of unit cell volume were fit to the third order Birch-Murnaghan equation of state [33, 190]:

$$p(\epsilon) = \frac{3B_0}{2}\left[\left(\frac{\xi}{\epsilon}\right)^7 - \left(\frac{\xi}{\epsilon}\right)^5\right]\left[1 + \frac{3}{4}(B_0' - 4)\left(\left(\frac{\xi}{\epsilon}\right)^2 - 1\right)\right], \qquad (4.5)$$

where B_0 is the zero pressure bulk modulus and B_0' is the first derivative of the bulk modulus with respect to volume at zero pressure. Volumes are relative, measured with respect to the reference volume[2] V_{ref} of the experimental unit cell at 123 K. ξ is the zero pressure relative dilation at a given temperature and ϵ is the dilation at pressure $p(\epsilon)$. They are both defined as:

$$\xi = \left(\frac{V_0}{V_{\text{ref}}}\right)^{\frac{1}{3}}$$
$$\epsilon = \left(\frac{V(\epsilon)}{V_{\text{ref}}}\right)^{\frac{1}{3}}$$

The pressure in equation (4.5) was taken to be the isotropic pressure, which is the average of the trace of the instantaneous pressure tensor, taken over the course of a sampled trajectory. In the simulation, the volume was controlled by scaling the box matrix by an extra factor of

$$h = \begin{pmatrix} \epsilon & 0 & 0 \\ 0 & \epsilon & 0 \\ 0 & 0 & \epsilon \end{pmatrix} \tag{4.6}$$

Figure 4.5 shows the resulting isotherms at 123 K, 200 K, 237.65 K (points) along with the result of fitting (lines). Fitting gave a value of B_0' close to 6. To improve subsequent fits, B_0' was fixed to 6, as also used by Fortes et al. [85].

The values of ξ and B_0 are shown in Table 4.1. Sampling was performed for ~ 15 ps at $T = 200$ K and ~ 30 ps at $T = 123$ K and $T = 237.65$ K. The values that have equivalent experimental data are marked in bold. These values match the experiments within a few percent [85].

However, note the rapid increase of the bulk modulus upon cooling, with the value at 123 K (27.44(15) GPa) being almost double the value at 200 K (15.35(14) GPa) This is in contrast with ice Ih, which stiffens by ~ 2 GPa when cooled from 240 K to absolute zero [215]. Indeed, these calculations are also in contrast with ab initio calculations using the PW91 GGA functional, which obtain an absolute zero bulk modulus of 16.18(12) GPa [85] – a stiffening of ~ 1 GPa from the value at 200 K. The large increase in QDO-water may be caused by nuclear quantum effects, which become increasingly important in low temperature ice [202].

[2] V_{ref} corresponds to a density of $\rho(123K) = 1.17\,\text{g cm}^{-3}$ measured by Kamb [131]

T (K)	ξ	B_0 (calculated, GPa)	B_0 (measured, GPa)
123	**1.0039(2)**	27.44(15)	-
200	1.0102(3)	15.35(14)	-
237.65	1.0138(4)	**12.06(14)**	$\sim$ 12.7 [85]

Table 4.1 *The zero pressure dilations and bulk moduli of QDO-water in the ice II phase at 123 K, 200 K and 237.65 K.*

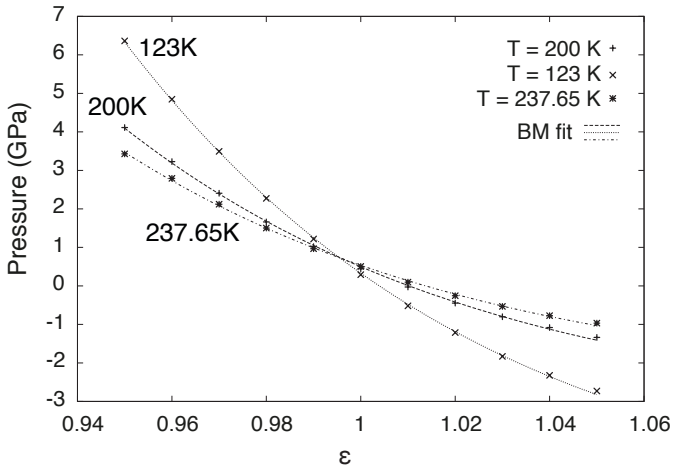

Figure 4.5 *Isotherms of Ice II at three temperatures: 123 K, 200 K and 237.65 K, plotted as a function of the dilation parameter* $\epsilon = \left(\frac{V}{V_{ref}}\right)^{\frac{1}{3}}$. *The reference volume* V_{ref} *is the experimental volume at 123 K and atmospheric pressure. Points represent calculated values while lines are fits to the Birch-Murnaghan equation of state.*

4.3.2 Isobars at atmospheric pressure

Isobars at atmospheric pressure were sampled at four temperatures: 100 K, 120 K, 140 K and 160 K. The parameters of interest were the density as a function of temperature and the a and c hexagonal lattice parameters. To assess how these quantities vary as a function of model parameters, their behaviour was converged with respect to the number of PIMD beads and the timescale of the simulation.

Convergence

The cumulative average of the density $\rho_{\mathrm{C}}(n\Delta t)$ as a function of time $n\Delta t$ is:

$$\rho_{\mathrm{C}}(n\Delta t) = \frac{1}{n}\sum_{i=1}^{n}\rho(i\Delta t), \tag{4.7}$$

where Δt is the simulation timestep and $\rho(i\Delta t)$ represents the instantaneous density at timestep i.

Since each sample of the density is correlated with its temporal neighbour, an accurate calculation of the error in the cumulative density needs an estimation of the correlation time. This is done by using block averaging [9]. Let $S_1 = \{x_i \mid i = \{1..n\}\}$ be a set of n measurements sampled from a given population with an unknown correlation between successive measurements. Define the block averaged set of measurements S_b with block size b as follows:

$$S_b = \left\{ \frac{1}{b-1}\sum_{i=j}^{j+b-1} x_i \,\middle|\, j \in \{1, 2, ...n-(b-1)\} \right\} \tag{4.8}$$

Then, an estimator of the standard deviation of the population of S_1 is:

$$\sigma_{\mathrm{pop}} = \max_{b\in\{1,2,..n/2\}} \sigma(S_b) \tag{4.9}$$

Figure 4.6 shows the cumulative average of the density as a function of simulation time with the standard error on the mean calculated using block averaging. In all three cases presented – 64, 96 and 192 beads – the density converges on a timescale of 10 ps. After discarding the first 10 ps, the average density and lattice parameters a_r and α_r of the rhombohedral unit cell are used to calculate the a_h and c_h parameters of the hexagonal cell as follows:

$$a_h = a_r\sqrt{2(1-\cos\alpha_r)} \tag{4.10}$$

$$c_h = a_r\sqrt{3(1+2\cos\alpha_r)} \tag{4.11}$$

The values of these parameters is plotted in Figure 4.6 as a function of the bead number P. In order to estimate their value for an infinite number of beads, their values were fit to a $1/P$ functional form:

$$y(P) = y_\infty - \frac{\epsilon}{P} \tag{4.12}$$

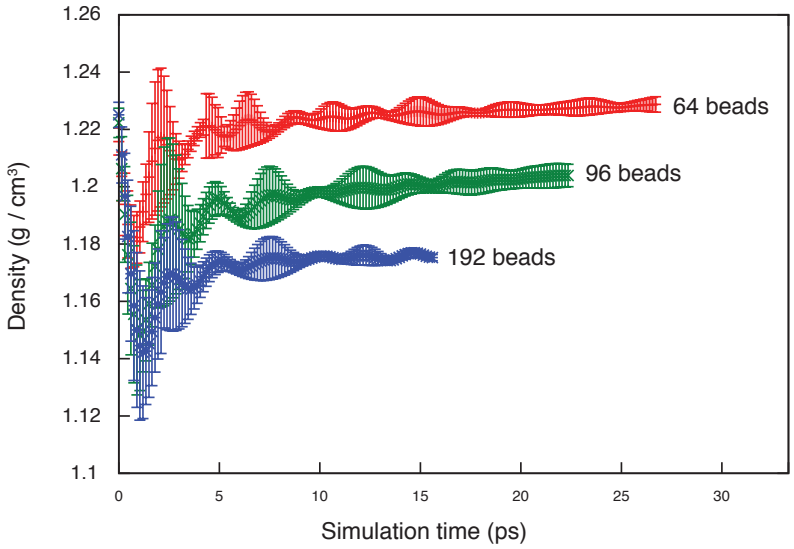

Figure 4.6 *A cumulative average of the density as a function of simulation time with increasing number of beads. The error bars are assigned via a block averaging method.*

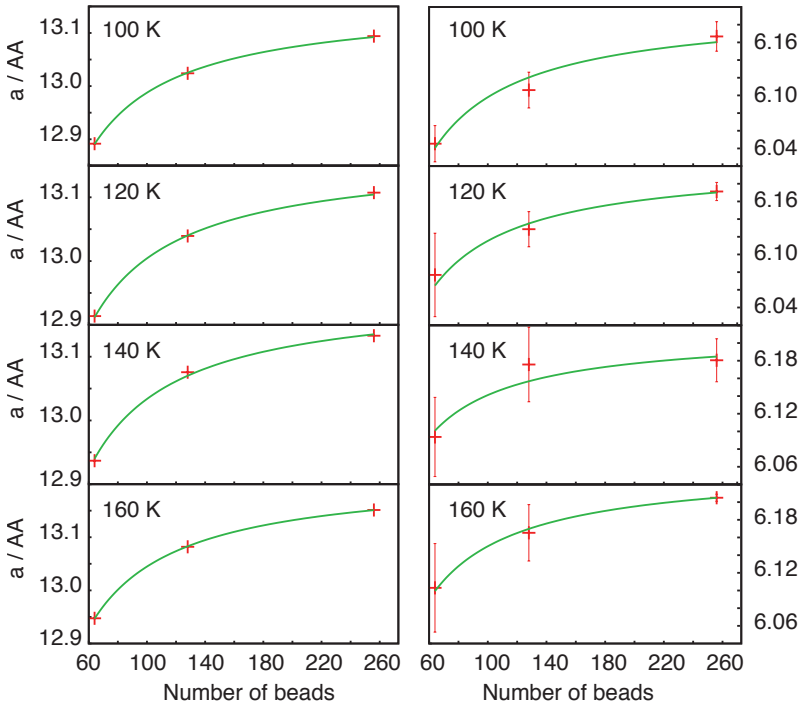

Figure 4.7 *Convergence of the lattice constants of ice II at atmospheric pressure as a function of number of beads P at temperatures between 100 K and 160 K. The red markers represent calculated values together with error bars assigned via a block averaging method. The green line represents a fit to an $1/P$ functional form.*

Lattice parameters

The lattice parameters, converged with respect to simulation time and extrapolated to infinite number of beads are presented in Figure 4.8 as a function of temperature. They show a good match: c is less than 1% away from experiment while a is 2% lower than experiment. Taking into consideration that the experimental data shows similar spread, this is a good match.

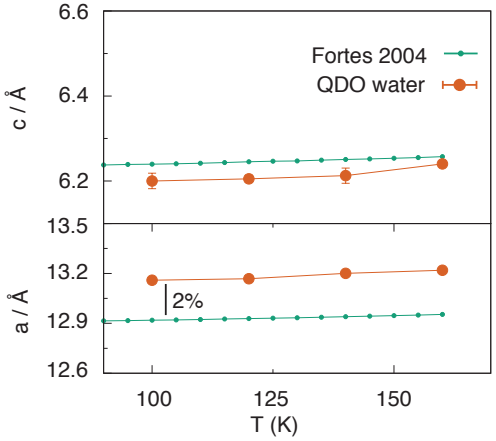

Figure 4.8 *The lattice parameters a and c extrapolated to the number of beads $p \to \infty$ compared with the experimental measurements of [86] (D_2O ice II).*

4.3.3 Polarisation density

Quantum Drude Oscillators are unique in providing an anisotropic polarisation to a model, allowing us to visualise the distribution of electrons in a given structure. The polarisation density is constructed by binning the number of beads in a three-dimensional grid, calculating the resulting charge density and subtracting the ground state charge distribution, which is a Gaussian centred on the M site.

Figure 4.9 shows the polarisation density, with blue regions depicting depletion of electronic charge and red regions enhancement. These regions show that regions close to oxygen atoms gain electronic charge while regions close to hydrogen atoms lose electric charge – this is expected, with the charge density in lone pairs being enhanced due to hydrogen bonding. There is also a qualitative difference between the two rings of ice II. The flat ring (right) has a more connected polarisation density than in the case of the puckered ring.

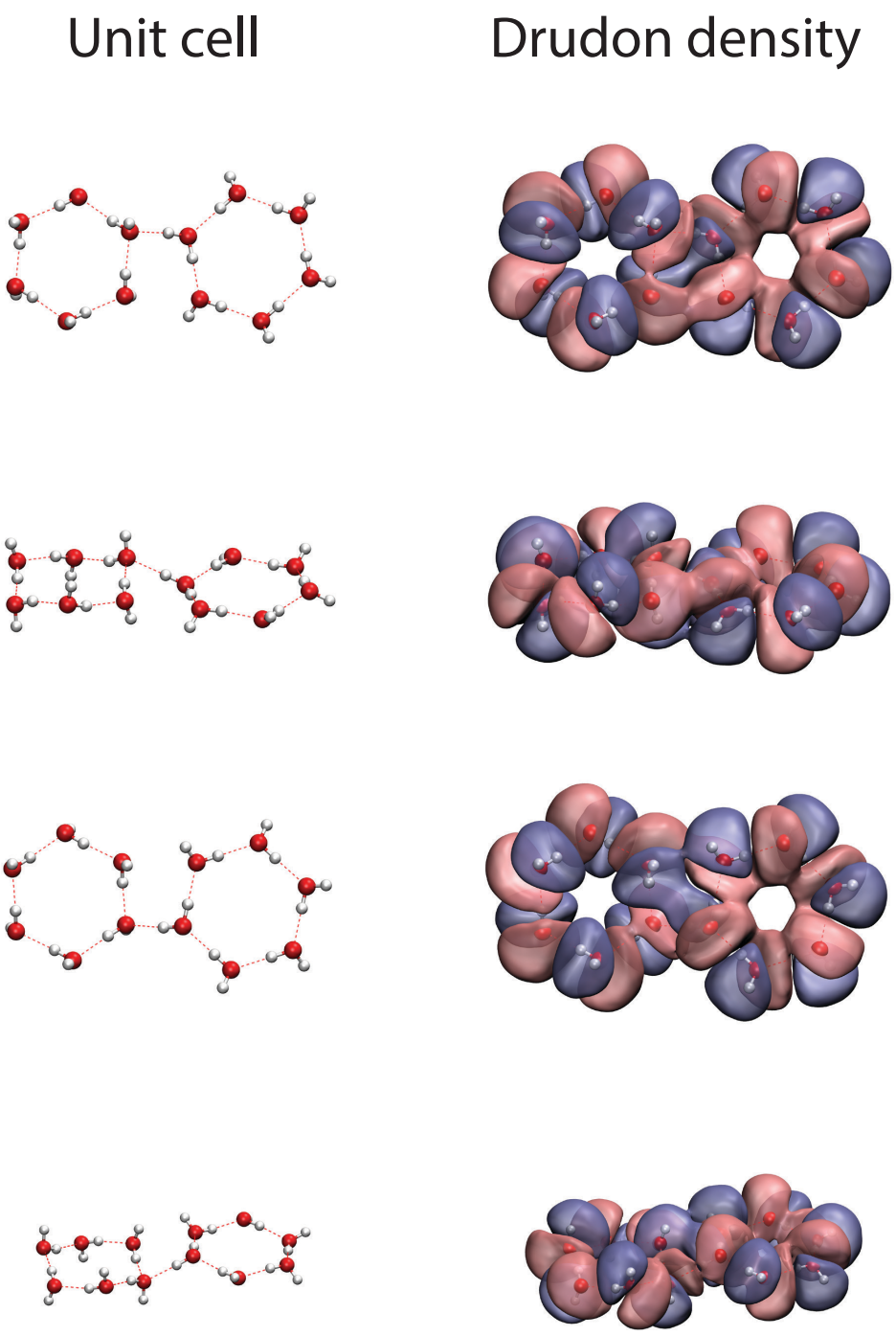

Figure 4.9 *The polarisation density of a unit cell of ice II at different angles. Blue regions represent depletion of electronic density relative to the case of an isolated molecule while red regions represent enhancement. The isosurfaces are drawn at a constant density of 0.014 beads/Å^3.*

4.4 Conclusion

Calculations of the lattice constants and bulk modulus of ice II using QDO-water were presented. The results are a good match to experiment: the bulk modulus at 237.65 K is within 1% of experiment, and the a and c hexagonal lattice constant are within 2% once converged with respect to the number of beads. The polarisation density reveals a complex pattern of polarisation that differs between the two rings of ice II, reveals the various degrees of cooperativity in different local environments of the water molecule and shows that the model does indeed polarise in an anisotropic manner.

Chapter 5

Liquid-vapour interface

Hydrogen bonding and molecular orientation at the liquid-vapour interface of water. Cipcigan, Sokhan, Jones, Crain, Martyna. PCCP 17 (14) 2015.

5.1 Why study the liquid-vapour interface

The liquid-vapour interface is important both fundamentally, as a basic model for biologic interfaces, and technologically. For example, one application is on-water catalysis. Experiments show that certain chemical reactions, such as the Diels-Alder cycloaddition, can be enhanced by as much as a factor of 1000 when occurring at the surface of water rather than in the bulk [130]. The prevailing hypothesis is that free OH groups at the surface of water stabilise intermediates and thus accelerate the reactions.

Fundamentally, the liquid-vapour interface is among the simplest heterogeneous systems water can form in nature. At this interface, the hydrogen-bonded network that binds the liquid is abruptly truncated in a manner that is still of debate for both simulation and experiment. Our knowledge about this interface comes from a combination of surface-specific sum frequency generation (SFG) spectroscopy [14, 71, 196, 208, 221], x-ray absorption spectroscopy [43, 304, 305] and simulations [145, 149, 150, 299, 306]. Before proceeding with an investigation of the liquid-vapour interface using QDO-water to demonstrate its transferability and discover new physics, I will review the existing knowledge and highlight the following open questions:

1. How do water molecules prefer to orient at the liquid-vapour interface?

2. Hydrogen bonds can be of two types: acceptor (connecting an oxygen atom to a hydrogen), and donor (connecting a hydrogen atom to an oxygen). Is there a preference for truncating one type of bond over the other? Are there any acceptor-only species at the interface?

3. What is the decay length of the dipole moment and how does it compare to that of the density?

4. What is the physical origin of the observed surface orientation?

Let's start with experiments. SFG spectroscopy uses a two-photon process to probe the second-order nonlinear susceptibility of a medium, $\chi^{(2)}$. Since the second-order polarisation is

$$P = \chi^{(2)} E^2, \tag{5.1}$$

any medium with inversion symmetry will have that:

$$-P = \chi^{(2)}(-E)^2 = P. \tag{5.2}$$

This relation is only satisfied when $\chi^{(2)} = 0$, meaning that the second order nonlinear susceptibility is nonzero only where inversion symmetry is broken, such as at a surface.

Choosing to combine a visible and an IR photon and to couple them to $\chi^{(2)}$ produces a signal tuned to probe the stretch frequency of the OH intramolecular bond. In the gas phase, the signal resonates at 3700 cm^{-1}. The presence of a hydrogen bond redshifts the signal due to slight charge transfer through the bond. At the surface of liquid water, the SFG signal shows a sharp peak centred at approximately 3700 cm^{-1}, corresponding to a free OH and a broad feature between 3100 and 3500 cm^{-1} corresponding to a hydrogen-bonded OH (Figure 5.1) [71]. The structure of this broad feature indicates that the hydrogen bonds have a different character at the surface than in bulk while its existence indicates that *each molecule participates in at least one donor bond*, meaning a negligible population of acceptor only bonds.

An alternative surface-specific method is Total Ion Yield X-Ray Absorption Spectroscopy (TIY-XAS) [304, 305]. The method works by exciting a core electron of a molecule, which results in its ionisation. In an electric field the ionised molecule escapes the sample, creating an ionic photocurrent. Due to the

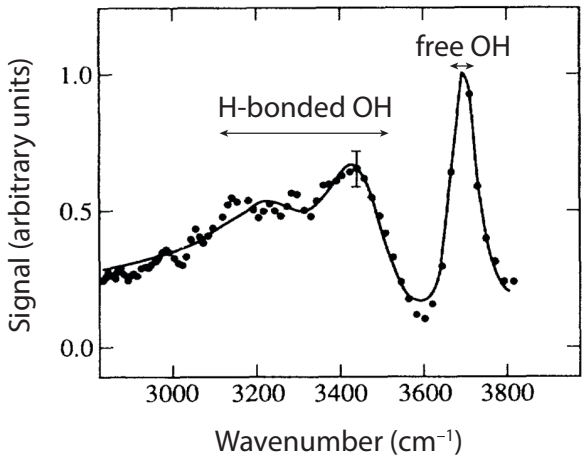

Figure 5.1 *The SFG spectrum of water. Reproduced from Du et al. [71]*

size of the ions, TIY-XAS is believed to be surface-specific, probing a sample down to an escape depth of around 5Å. The technique led to two observations: an expansion of the nearest neighbour oxygen–oxygen distance of 5.6% at the surface and the presence of acceptor-only species. This latter observation is in disagreement with SFG measurements. However, the TIY-XAS observations were latter retracted by the same group that first made them [43], citing evidence that the TIY-XAS spectrum is indistinguishable to a bulk spectrum. Thus, it couldn't have been a reliable probe of the surface.

The liquid-vapour interface has also been studied by simulation, which is able to directly access molecular detail. The main conclusion from these studies is that the results depend strongly on both the model used and the definition of a hydrogen bond. For example, only polarisable models and ab initio simulations are able to reproduce the experimentally measured surface expansion [299]. Furthermore, classical polarisable models disagree with ab initio simulations on the speed of decay of the interfacial dipole moment, with classical models having a higher interfacial dipole moment than DFT studies [299].

Hydrogen bonds are also an issue models disagree on. The DFT based simulations of Kuo and Mundy [150] predict a sizeable fraction of acceptor-only molecules in agreement with TIY-XAS experiments. On the other hand, Kühne et al. [145] report no such species and agrees with SFG experiments, highlighting the importance of choosing an unbiased method of assigning a hydrogen bond.

In light of these experiments and simulations, in this chapter I will directly address

both the orientation of water molecules at the surface and nature of hydrogen bonds at the liquid-vapour interface of water, via simulations of QDO water. These simulations served to both test the transferability of the model to the liquid phase and a heterogeneous environment and to discover new physics about the structure of water. I start with demonstrating that the model produces a realistic interface.

5.2 Validation of the liquid-vapour interface of QDO-water

5.2.1 Simulation setup

Two sets of simulations, with their initial conditions illustrated in Figure 5.2 were ran to investigate the coexistence between the liquid and the vapour: one aimed at simulating the bulk liquid and vapour phases and one aimed at directly equilibrating a liquid-vapour interface.

To investigate the individual liquid and vapour phases, a cubic unit cell was initialised and simulated in the NPT ensemble at the experimental coexistence pressure of the liquid and gas respectively [154]. Simulations of 300 molecules were performed at temperatures between 300 and 600 K in steps of 50 K, and at 620 and 630 K (the temperature step was reduced above 600 K due to the approach to the critical point).

To directly equilibrate a liquid-vapour interface, the lamella geometry was used. A unit cell with the z dimension larger than the x and y dimensions was seeded with a liquid centre of 576 molecules and left to equilibrate. The number of molecules is higher than for the bulk phases in order to create a liquid centre of thickness large enough to ensure that interfacial correlations decay. The pressure was monitored and the simulation was deemed to have equilibrated when the cumulative average of the pressure converged. The equilibrated system, when periodically reproduced represents an infinite arrangement of parallel liquid layers. These layers are separated by half the z dimension and are replicated infinitely in the z direction.

5.2.2 Liquid-vapour coexistence densities and the critical point

For two phases, at each temperature, there is a pressure at which they can coexist. This pressure and the corresponding density of each phase trace the *coexistence curve*, which ends at a critical point. For the liquid-vapour transition of water, this critical point occurs at $\{T_C = 647.096\text{K}, \rho_C = 0.322\text{g/cm}^3\}$ [287]. The first step to validate the predictions of QDO-water for the liquid-vapour interface is to

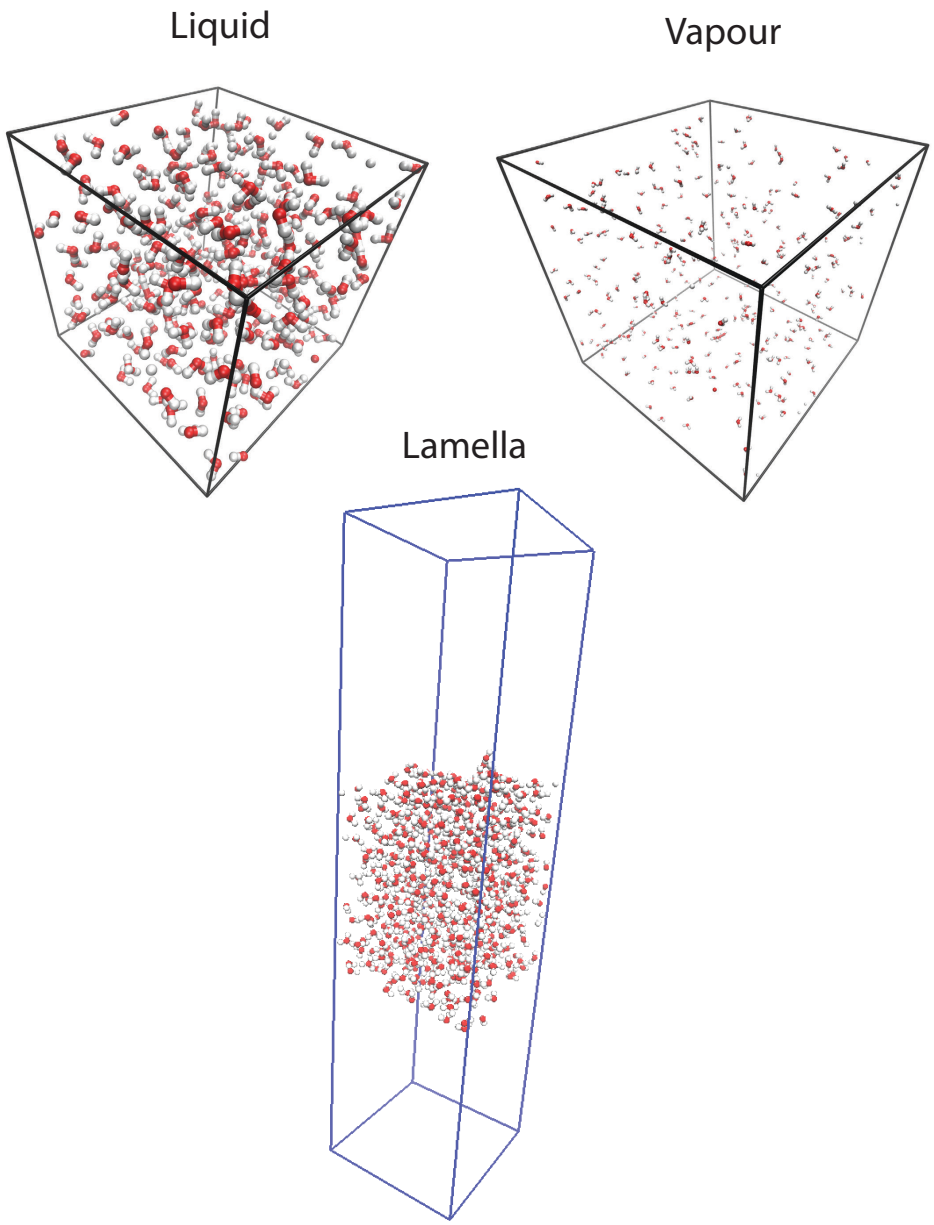

Figure 5.2 *The unit cells for three types of simulation: liquid branch, vapour branch and lamella. The scale changes between the figures. The liquid and vapour branches were simulated in the NPT ensemble at a pressure equal to the coexistence pressure, with the aim of calculating the coexistence density. The lamella was simulated in the NVT ensemble using an elongated box, with the aim of directly equilibrating a liquid-vapour interface.*

verify that its coexistence curve matches experiment. This verification was done using the first set of simulations, in the NPT ensemble, with the pressure fixed to the experimentally measured coexistence pressure. At each temperature, a unit cell prepared at the experimental density was equilibrated and then sampled for 80-100 ps. The density was checked for convergence with respect to the timestep, with the resulting average densities shown in Figure 5.3.

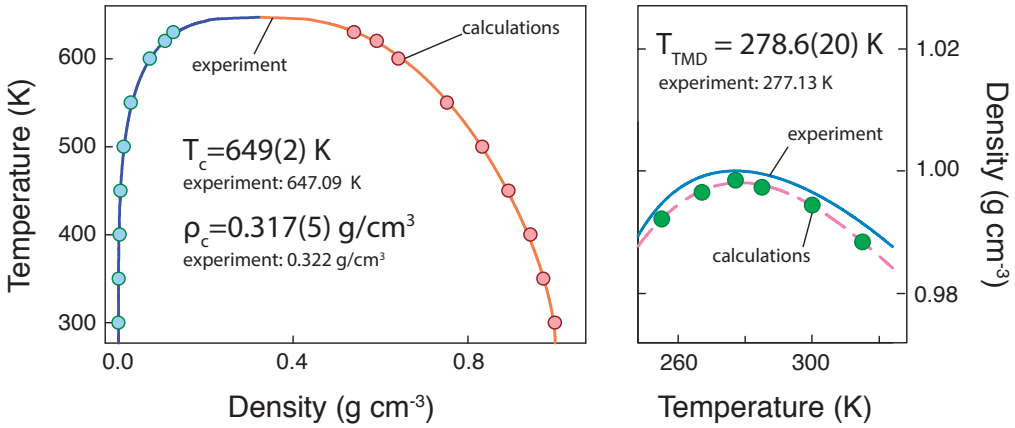

Figure 5.3 *The calculated liquid and vapour branches of the coexistence curve (dots) compared with experiment [154, 287] and the temperature of maximum density. The critical temperature was calculated by fitting the difference between the liquid and the vapour densities to the Wegner expansion [293]. Figure adapted from Sokhan et al. [255].*

The critical point was calculated from a fit to the Wegner expansion [293], which expresses the difference between the liquid density ρ_l and vapour density ρ_v as $\rho_l - \rho_v = A_0\tau^{\beta} + A_1\tau^{\beta+\Delta}$, with $\tau = 1 - T/T_c$. Since water's liquid-vapour transition is in the same universality class as the Ising model, $\beta \approx 0.325$ and $\Delta = 0.5$. The results of the fit $\{T_C = 649(2)\text{K}, \rho_C = 0.317(5)\text{g/cm}^3\}$ agree within one error bar with the experimental values of $\{T_C = 647.096\text{K}, \rho_C = 0.322\text{g/cm}^3\}$ [154, 287].

5.2.3 Structure of the liquid

The structure of a disordered phase can be quantified by its radial distribution function (RDF) $g(r)$. Since water is a multi-atom molecule, it will have three radial distribution functions: oxygen–oxygen, oxygen–hydrogen and hydrogen–hydrogen.

Figure 5.4 shows the evolution of the three RDFs of the liquid branch as a function of temperature, from 300 K to the critical point. The RDF at 300 K is compared with the experimental benchmark of Soper [258], who combined independent neutron and x-ray scattering studies into one comprehensive dataset. The RDF of QDO-water matches this experimental benchmark well. In particular, the peaks of the oxygen–oxygen RDF are close to the experimental value, with the second shell being at smaller radii than experiment.

The RDFs also reveal the evolution of water's structure as the system is heated. At 300 K, the oxygen–oxygen radial distribution function shows three well-developed shells at distances smaller than 10 Å. As the system is heated up to 450 K and beyond, the second and third shell disappear, while the space between them becomes populated with a new second shell. This shows that the structure of high-temperature liquid water is different than that of ambient water, with ambient water having a structure closer to ice than to an isotropic (ideal) liquid.

The same story is visible in the oxygen–hydrogen and hydrogen–hydrogen radial distribution functions. The first two peaks correspond to the first coordination shell, with the structures beyond ~ 4 Å bearing a fingerprint of the second and third shells. The first shell persists as the temperature is increased, with the second and third shells merging into one, again revealing the different character of high temperature water.

Matching the experimental RDFs alone does not necessarily mean the model is realistic since a model can match the structure exactly yet badly predict all other quantities. For example, one such model is a one-particle water molecule, interacting with its neighbours via the potential of mean force $W(r) = -kT \log g(r)$. However, the structure combined with the correct prediction of the liquid-vapour coexistence curve shows that QDO-water does indeed predict a realistic liquid from ambient temperature to the critical point, alongside a realistic ice II demonstrated in the previous chapter.

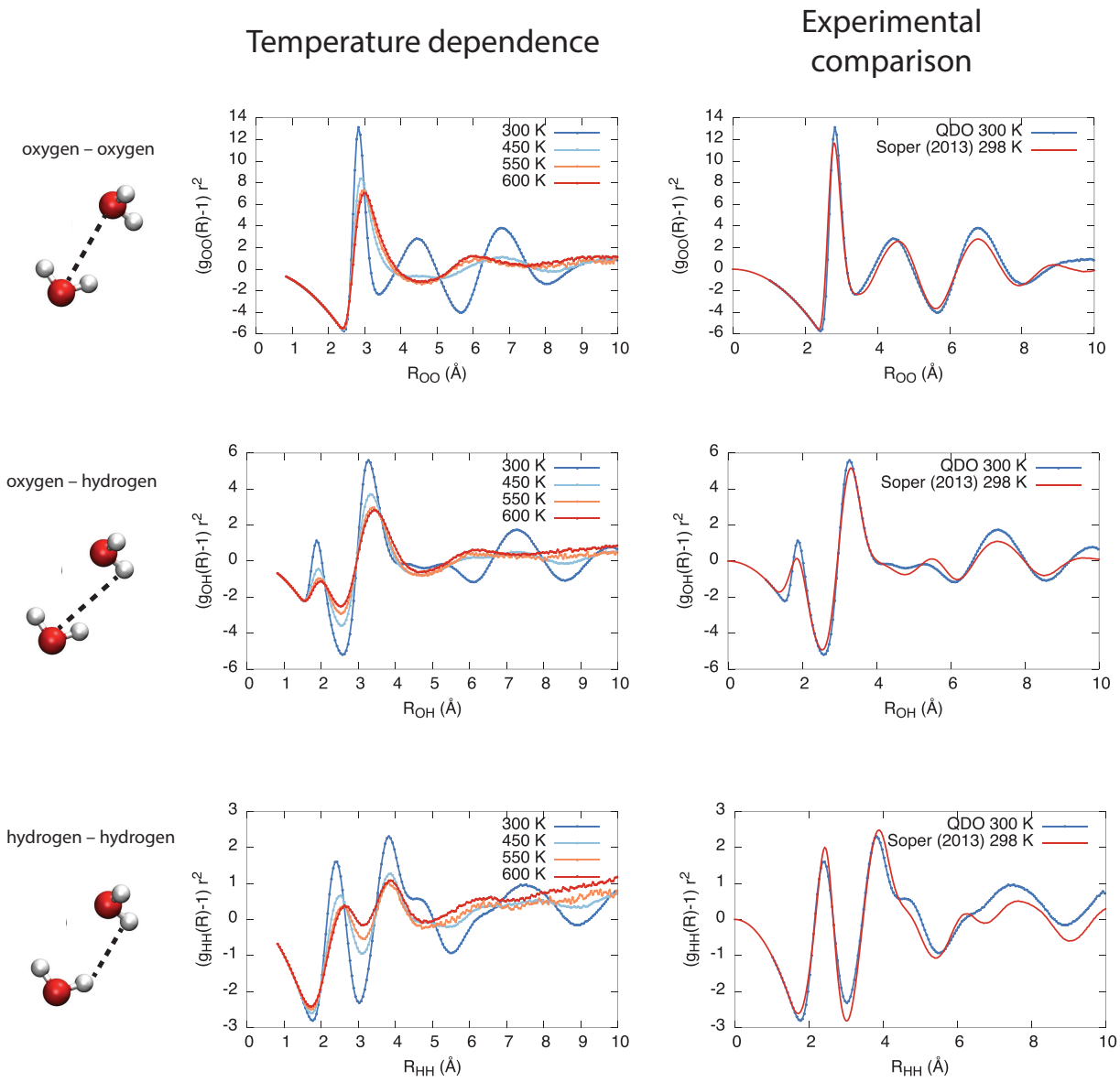

Figure 5.4 *The oxygen–oxygen, oxygen–hydrogen and hydrogen–hydrogen radial distribution functions. In order to see the shells beyond the first, instead of plotting $g(r)$, we plot $r^2(g(r) - 1)$, which is proportional to the density of particles in a shell at radius r.*

5.2.4 Surface tension

A further indicator of the accuracy of describing a surface is the surface tension γ. It is related to the pressure in a unit cell by the following formula:

$$\gamma = L_z \frac{p_n - p_t}{2} \tag{5.3}$$

where where L_z is the z extent of the unit cell and p_n, p_t are the normal and tangential components of the pressure tensor, respectively. Using this formula, the surface tension at 300 K is 70.3 mN m^{-1}, within 2% of the experimental value of 71.7 mN m^{-1} [154]. The temperature dependence is shown in Figure 5.5, which again shows a good match to experiment. Close to the critical point, large fluctuations result in longer sampling times needed to obtain for accurate results, explaining in deviation of the calculations at temperatures above 600 K from the experimental reference. Linearly extrapolating the surface tension versus temperature to 0 gives a second estimate of the critical temperature of 656(6) K, 1.5 standard errors away from the experimental value of 647.096(10) K [287] and 1 standard error away from the estimate based on fitting to the Wegner expansion, 649(2) K.

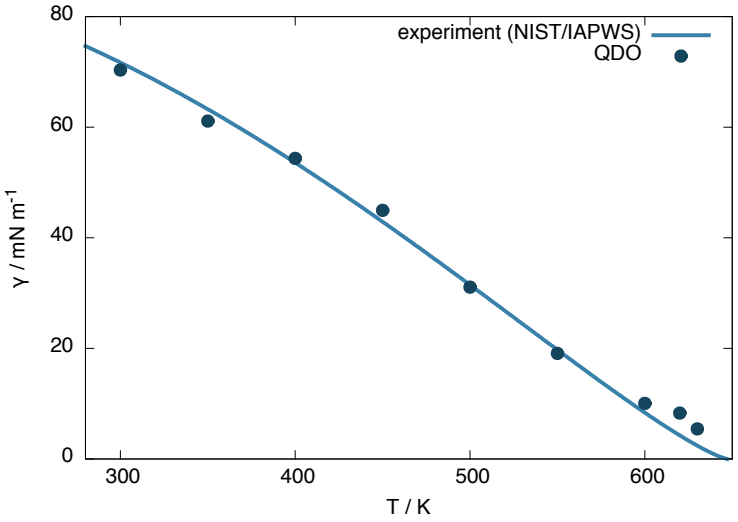

Figure 5.5 *Surface tension of QDO water as a function of temperature compared with NIST/IAPWS experimental data [154]. Linearly extrapolating the surface tension to 0 gives a critical temperature of 656(6) K. This critical temperature does not change by more than one error bar if the points above 600 K are removed from the extrapolation.*

5.3 Molecular structure of the liquid-vapour interface of QDO-water

5.3.1 Defining the surface of the liquid

Before analysing the molecular structure of the surface, we must define what a surface is. To do so, consider the 300 K lamella. The unit cell is $23.36 \times 23.36 \times 93\,\text{Å}^3$, with a liquid centre that is left to equilibrate, forming two interfaces. The density as a function of z position, measured relative to the centre of mass of the lamella is shown in Figure 5.6 alongside the dipole moment as a function of z.

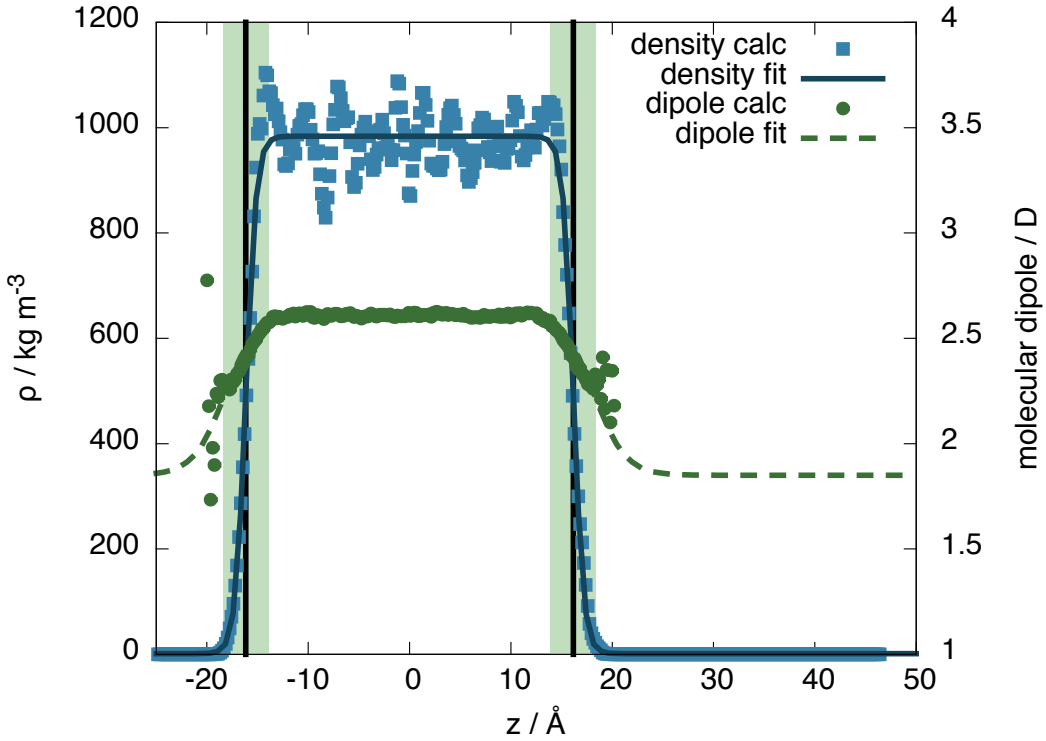

Figure 5.6 *The density and molecular dipole moment as a function of position in the unit cell. The dots are calculated values and the lines are fits to a hyperbolic tangent function. The surface region is denoted by the light coloured band, centred around the black vertical line marking the Gibbs dividing surface.*

To define a surface, the density profile is fit to a hyperbolic tangent function

$$\rho(z) = \frac{\rho_L - \rho_V}{2}\left[1 + \tanh\left(-\frac{|z| - z_g}{\delta}\right)\right] + \rho_V \tag{5.4}$$

which gives the interior (liquid) density as $\rho_L = (984 \pm 3)$ kg m^{-3}, within 1% of the density of the liquid at coexistence pressure (997 kg m^{-3}) [154] and the exterior (vapour) density as $\rho_V = (1 \pm 2)$ kg m^{-3}, within one standard error of the density of the vapour at coexistence pressure (0.025590 kg m^{-3}) [154]. This shows that the liquid-vapour coexistence densities predicted by independent liquid and vapour simulations are reproduced when the two phases coexist, increasing the confidence in that the model really does predict a realistic interface.

The Gibbs dividing plane is defined as the point where $\rho(z) = \frac{1}{2}(\rho_L - \rho_V)$ and lies at $z_g = 16.2$ Å. This results in an interfacial decay length of $\delta = 1.01$ Å. Following the usual literature convention, the mean field interfacial region is defined as the region between 90% and 10% liquid density, with the interior region lying above 90% liquid density. With these definitions, the interfacial width is 2.22 Å, or about one molecule thick. The interior region is $2(z_g - \delta) = 30.2$ Å thick.

Note the periodic fluctuations in density throughout the lamella. In order to confirm these fluctuations are a real effect and not a consequence of sampling, longer simulations are needed, where fluctuations of the interface are averaged over the length of the trajectory. However, a layering effect has been confirmed when considering the *instantaneous* interface [137], defined using the criterion given by Willard and Chandler [301].

With an interior region that is about 10 molecules thick, we need to check whether it is indeed a bulk liquid. Figure 5.7 shows a comparison of the oxygen–oxygen radial distribution functions between the interior region, equivalent bulk liquid simulations at coexistence pressures and experiment [258]. The interior region is slightly overstructured with respect to both the independent liquid simulations and experimental data, consistent with the lower density. Similar simulations using 4000 molecules give an interior region with a local structure and density ($\rho_L = (987 \pm 2)$ kg m^{-3}) closer to that of a bulk liquid (Figure 5.8), showing that indeed, the interior properties of a slab of 30.2 Å thickness are still influenced by the surface. However, since simulation times are prohibitive to obtain a full temperature sweep for 4000 molecules, we chose to focus on the 576 molecule lamella, as the radial distribution function is still realistic for the smaller system.

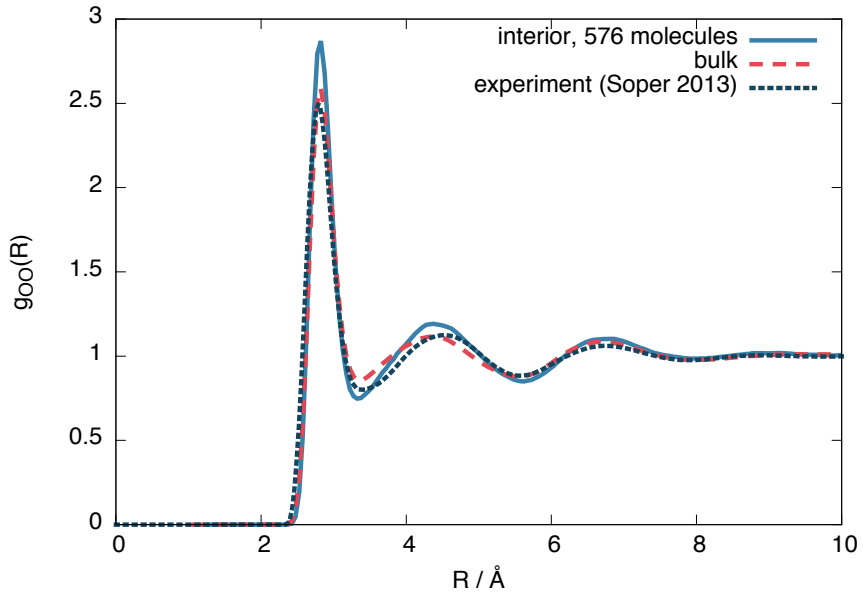

Figure 5.7 *The interior, bulk and experimental [258] oxygen–oxygen radial distribution functions for a 576-molecule lamella.*

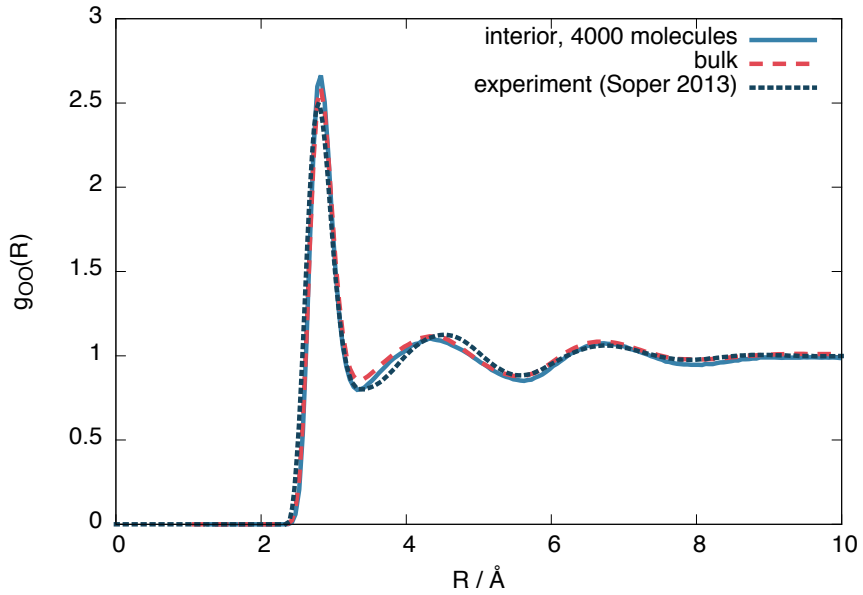

Figure 5.8 *The interior, bulk and experimental [258] oxygen–oxygen radial distribution functions for a 4000-molecule lamella.*

5.3.2 Interfacial molecular dipole moment

Since the density changes at the surface, so should the dipole moment. Figure 5.6 shows, alongside the density, the magnitude of the molecular dipole moment.

Fitting its value to a similar functional form to the density

$$\mu(z) = \frac{\mu_L - \mu_G}{2}\left[1 + \tanh\left(-\frac{|z| - z'_g}{\delta'}\right)\right] + \mu_G \tag{5.5}$$

with the vapour phase dipole fixed to $\mu_G = 1.85$ D gives a molecular dipole moment in the liquid phase of $\mu_L = 2.6$ D. This value is equal to the early estimates of Coulson and Eisenberg [59], who calculated the enhancement in dipole moment of a water molecule in an ice lattice based on the polarising field of its neighbours. The value is also within one error bar of the experimental estimate of 2.9(6) D [19]. However, it is smaller than the ab initio estimate of 3.0 D [247], which is based on partitioning the DFT charge density into individual molecular contributions using maximally localised Wannier functions. Since QDO-water generates the local structure of the liquid accurately, the relative enhancement of DFT may be due to the overstructuring of the liquid present in DFT simulations [175] or charge transfer through a hydrogen bond.

The z coordinate where the dipole moment has decayed to half the difference between liquid and vapour lies at $z'_g = 18.3$ Å, a coordinate where the density has decayed to 1.6% the bulk liquid's density. The dipole's decay length is also larger than that of the density's, with $\delta' = 3.06$ Å. Furthermore, over the surface region the dipole moment's magnitude varies between 2.34 and 2.52 D, with an average value of 2.44 D (94% of the interior value of 2.6 D). Therefore, as a consequence of this slow decay of the dipole moment into the vapour, the surface molecules are electrostatically similar to those in the bulk, in line with the surface's large cohesive energy.

This is the first prediction of the model answering one of the questions we set out to answer: the decay length of the dipole is slower than that of the density, with a surface not much different than the bulk in terms of the charge distribution of the molecule. This result also shows why fixed charge models reproduce a close-to-realistic surface while their electrostatics are parametrised to match the values of the bulk phase.

5.3.3 Surface structure

To reveal the surface structure, the interior and surface oxygen–oxygen radial distribution functions (RDFs) are compared in Figure 5.9. From this comparison, we conclude that the free surface is expanded relative to the bulk liquid. This is

the second prediction that answers one of the questions we set to answer.

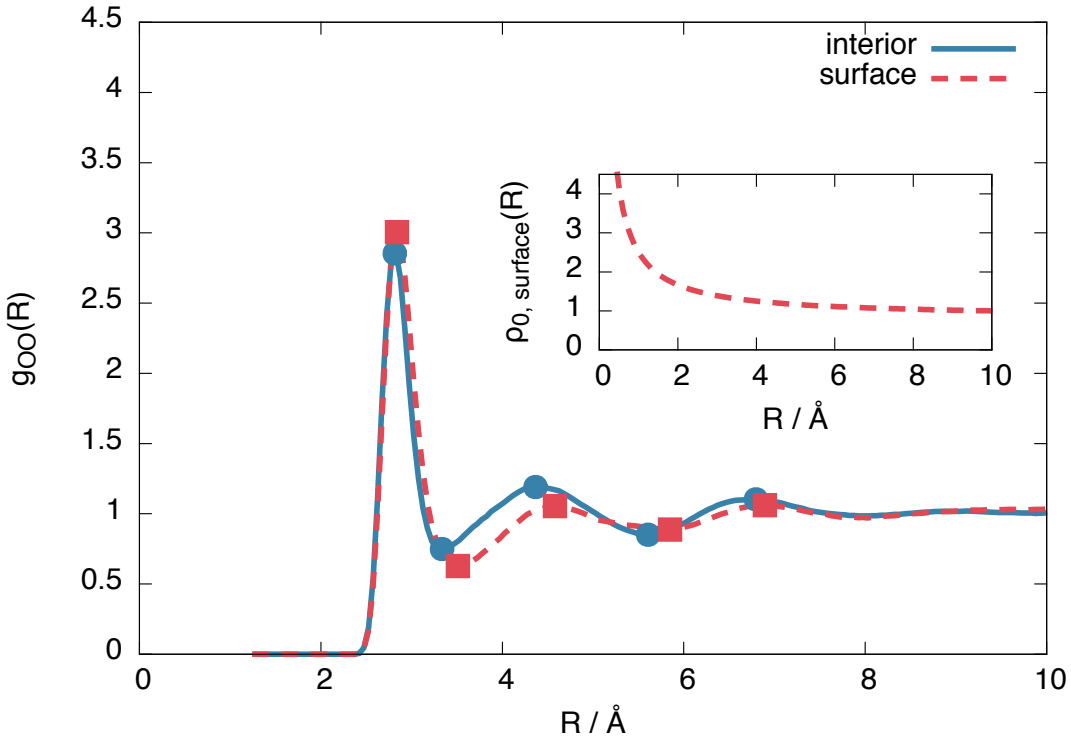

Figure 5.9 *The surface and interior oxygen–oxygen radial distribution functions of the 576 molecule layer, showing a surface expansion of the nearest neighbour oxygen–oxygen distance at the surface. The inset shows the radius–dependent normalisation applied to the surface radial distribution function, as described by equation* (5.7).

To make the expansion quantitative, we numerically calculated the second derivative of both RDFs using a smooth noise robust differentiator [110] and calculated its R intercepts to give the extrema. These extrema show the first shell expanding by 0.9% at the surface while the second shell expanding by 4.9%. The average distance between instantaneous nearest neighbours also increases at the surface by around 1.3%. This is in qualitative agreement with recent XAS experiments, which predict a surface expansion of 6% [305] and ab initio simulations, predicting a more modest surface expansion of 1% [145], but in contrast with point charge models, which predict a surface contraction [149].

The radius dependent normalisation of the surface radial distribution function is an artefact of the calculation method. To understand this artefact, consider an infinitely sharp interface between an uniform fluid of density ρ_0 and a vapour of density ~ 0 (Figure 5.10).

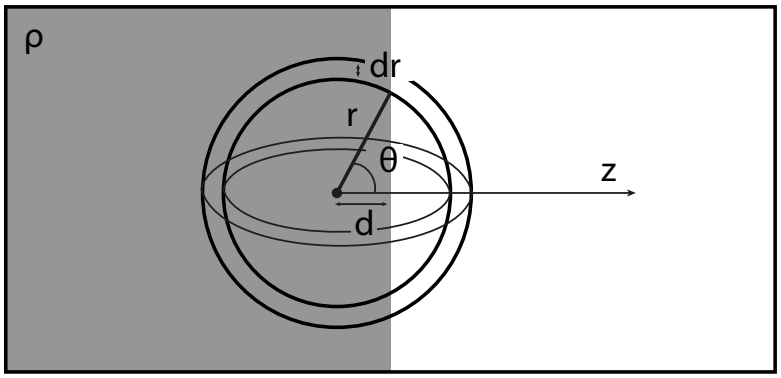

Figure 5.10 *An infinitely sharp interface and a spherical shell of radius r and width dr, centred at distance d away from the interface.*

If $d >> r$, all of a spherical shell of radius r and width dr contains fluid. However, when $d \sim r$, the amount of fluid enclosed in the sphere will depend on r. To calculate this dependence, let z be normal to the interface. The total fluid volume enclosed is then:

$$\begin{aligned} dV &= r^2 dr \int_0^{\frac{\pi}{2}} d\phi \int_{\cos^{-1}(\frac{d}{r})}^{\pi} sin(\theta)\, d\theta \\ &= 4\pi R^2 dR \frac{1}{2}\left[1 + \frac{d}{R}\right] \end{aligned} \tag{5.6}$$

In practice, the surface radial distribution function is normalised with the following radial dependent density:

$$\rho_{\text{surface}}(R) = \rho_{0\,\text{surface}}(R)\left(1 + \frac{d}{R}\right)\left(1 + \frac{d}{\xi}\right) \tag{5.7}$$

where $\rho_{0\,\text{surface}}(R)$ is the average surface density. The free parameters were chosen as $d = 2$ Å (roughly the size of the surface) and $\xi = 10$ Å (the largest R considered). We note that the surface expansion is qualitatively unaffected by small variations in d and ξ.

5.3.4 Hydrogen bonding

We now move on and look at the molecular structure at the interface. We begin with defining a hydrogen bond using the prescription of Kumar et al. [147].

Let the O–O separation between two molecules be R and the H-O–O angle be β (see Figure 5.11). These coordinates then have a corresponding potential of mean force, $W(R, \beta) = -kT \ln(g(R, \beta))$, which is shown in Figure 5.12 for the interior and surface regions.

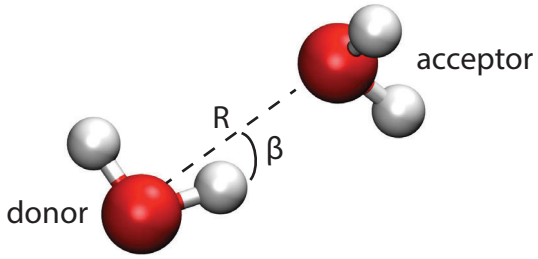

Figure 5.11 *The coordinates of the potential of mean force.*

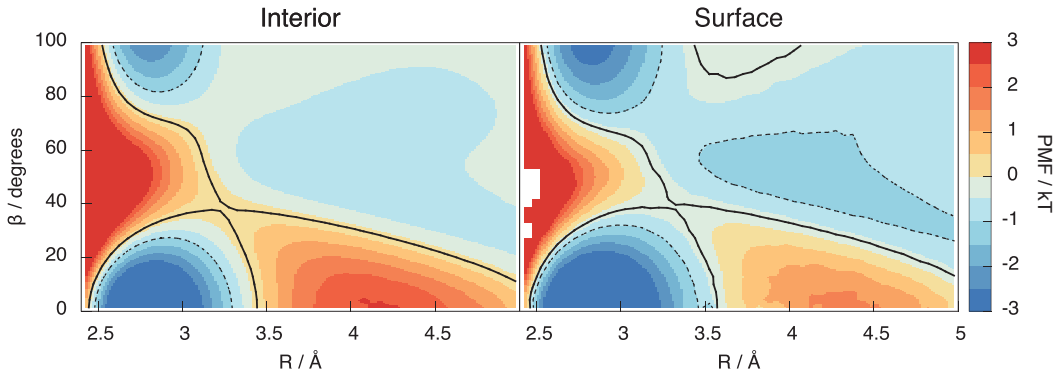

Figure 5.12 *The potential of mean force in the interior (left) and surface (right) regions of the lamella at 300 K. The black lines are the contour passing through the saddle point, with a hydrogen bond being identified as all (R, β) configurations within the bottom contour. The dotted line is a more restrictive contour at -1 kT used to confirm the 5 H-bonded configurations were not an analysis artefact.*

Two molecules are hydrogen-bonded (abbreviated as H-bonded from now on) when their (R, β) coordinates lie inside the contour passing through the saddle point at around 3.5 Å and 40° (black line in Figure 5.12). The molecule containing the participating hydrogen is the donor, with the other being the acceptor of this H-bond. The molecules are then categorised based on the number of donors and acceptors, writing a D for each donor and an A for each acceptor. For example, DDAA represents the traditional 4 coordinated tetrahedral cage of water with 2 donor bonds and 2 acceptor bonds.

Using the criterion given in the previous paragraph, the average number of H-bonds per molecule is 3.77 in the interior region and 3.25 in the surface region, for a 576 water molecule layer. The number decreases to 3.71 and 3.16 respectively for a 4000 molecule layer. The values agree the ab intio calculations of Kühne et al. [145] in the interior region (where they report 3.7 H-bonds per molecule) yet are greater when considering the surface: 3.16 for 4000 molecules of QDO-water versus 2.9 for ab initio. Using the same criteria and 576 TIP4P/2005 molecules, gives 3.69 H-bonds per molecule in the interior region and 3.11 H-bonds per molecule at the surface. These results show that, as long as we use a consistent H-bonding criterion, there is little variation in the number of hydrogen bonds per molecule between empirical models. However, all these results are slightly larger than the experimental estimates of 3.4 (interior, based on the enthalpy of sublimation of ice) [204] and 3.0 (based on SFG measurements) [71] respectively. Figure 5.13 summarises the average number of H-bonds predicted by the different models.

In the interior region, the total number of acceptor and donor bonds balance to within 0.3%, as expected; each bond is an acceptor to one molecule and a donor to another. However, at the surface, there is a 6% increase of donor bonds over acceptor bonds. This increase shows a preference of acceptor bonds to be broken when forming the interface, leaving extra donor bonds to be formed with molecules from the interior region, to satisfy water's propensity for four-fold coordination.

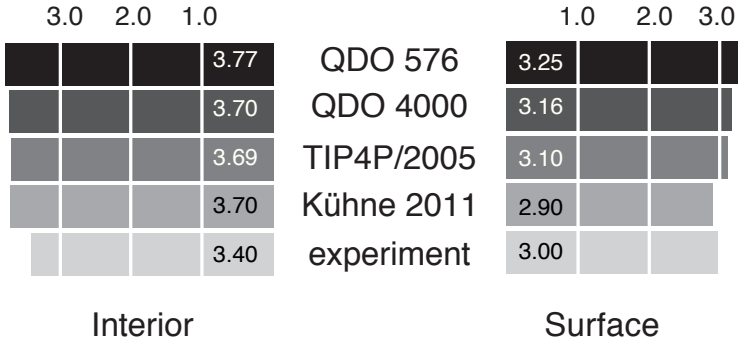

Figure 5.13 *Average number of hydrogen bonds per molecule in the interior region predicted by QDO-water (576 and 4000 molecules), TIP4P/2005 (576 molecules), ab initio [145] and experiment [71, 204].*

5.3.5 Hydrogen bond populations

To look in depth at hydrogen-bonding, the frequency of each H-bonded configuration in the interior and surface regions of the lamella is computed, as shown in Figure 5.14. To verify the calculations, the frequencies of configurations with no donor bonds (A, AA), one donor bond (D, DA, DAA), and two donor bonds (DDA, DDAA, DDAAA) are added to calculate the percentage of acceptor only (nD), single donor (sD) and double donor (dD) bonds, which have been previously reported in the literature. The interior region contains 1% nD, 13% sD and 86% dD bonds, in agreement with the ab intio simulations of Kühne et al. [145] and with TIP4P/2005. Similarly, the surface region contains 2% nD, 29% sD and 68% dD. Thus, QDO-water has a 10% larger population of dD bonds than TIP4P/2005 (3% nD, 39% sD and 57% dD), balanced by a 10% lower population of sD bonds. The surface of QDO-water also shows more structure than the results obtained by Kühne et al. [145] (however, I chose a larger interfacial region than Kühne et al. [145]).

This answers a third question: QDO-water shows no significant population of acceptor-only species at the liquid-vapour interface, in agreement with SFG measurements.

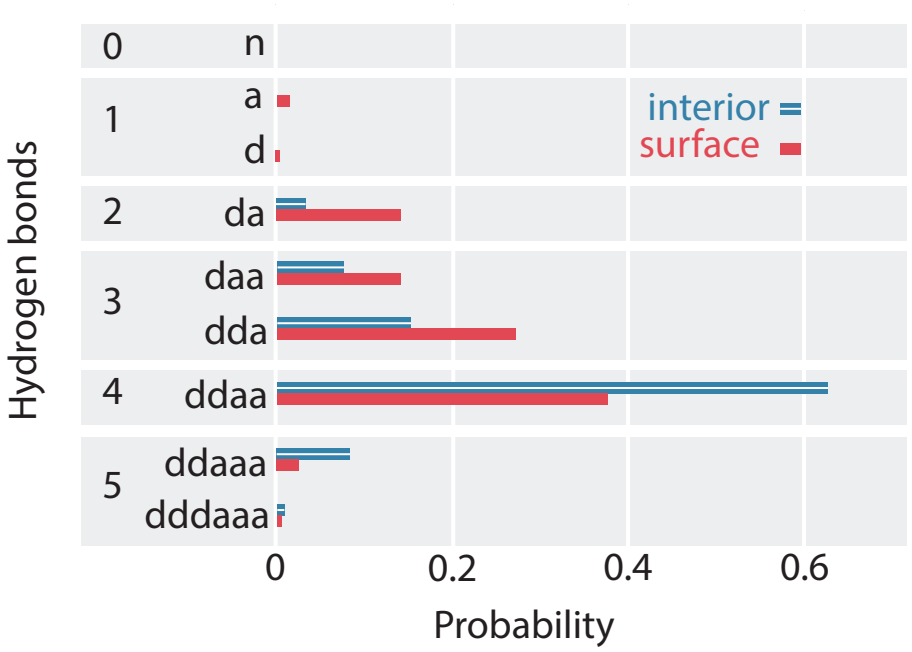

Figure 5.14 *The probability of each H-bond configuration in the surface and interior regions of the lamella.*

At the surface, the overall preference for forming donor bonds over acceptor bonds is revealed to be a preference for forming DDA over DAA H-bonded configurations. However, it is notable that this preference remains in the interior region, where DDA still dominates over DAA.

To balance donor and acceptor bonds, the interior region contains a small but statistically significant (8%) population of 5 H-bonded configurations (DDAAA), an example of such being shown in Figure 5.15. To my knowledge, these motifs have not been reported before. To test whether the motifs could be an artefact of the method, the PMF contour is reduced to -1 kT (the dotted region in Figure 5.12). While this reduction decreases the number of 5 H-bonded configurations, they are still present. An analysis of TIP4P/2005 also shows this motif.

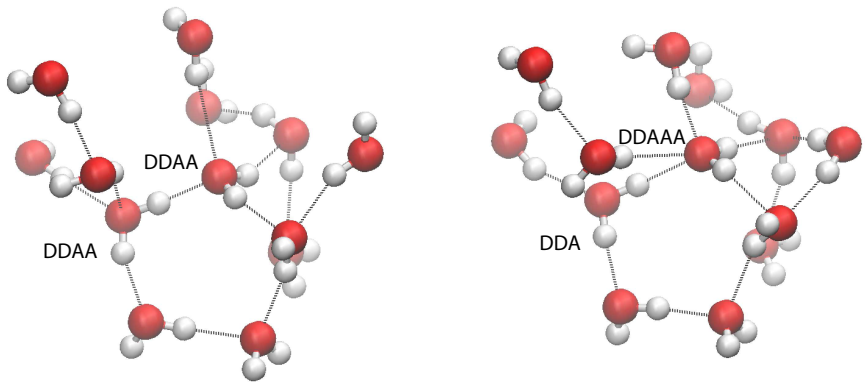

Figure 5.15 *(left) A snapshot of two DDAA molecules evolving into a 5 hydrogen-bonded configuration. (right) A snapshot of a 5 hydrogen bonded configuration.*

A possible mechanism for the creation of 5 H-bonded species is as follows. Imagine two neighbouring 4-coordinated DDAA molecules (see Figure 5.15) sharing an H-bond. In the liquid, fluctuations perturb the structure and those perturbations tend to decrease the volume (since 2xDDAA is a low density structure). One such fluctuation involves a molecule losing an acceptor bond (becoming DDA), with that bond being immediately transferred to the second molecule, which becomes DDAAA.

5.3.6 Surface orientation

Since at the surface, the broken hydrogen bonds are more likely to point towards the vapour phase, the preference of breaking acceptors over donors will result in a preferential surface orientation. Quantifying this orientation and understanding its physical origins will answer the final questions we set to answer in this chapter. The orientation is quantified using a joint distribution function of two angles. To define these angles, let $\mathbf{c}$ be the C_{2v} symmetry axis of the water molecule (bisecting the H-O-H angle) and $\mathbf{b}$ be the HH axis, which is a undirected (so $\pm\mathbf{b}$ represents the same vector). Also, let $\mathbf{n}$ be the surface normal.

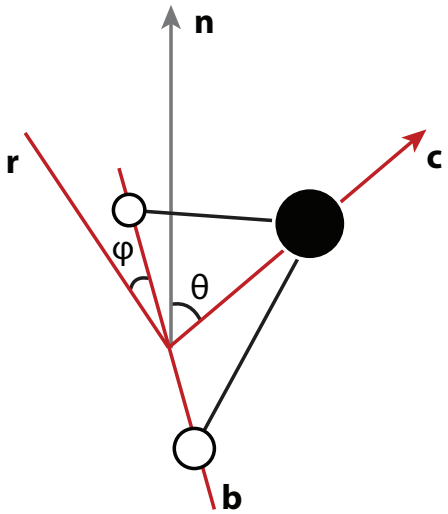

Figure 5.16 *Illustration of the angles used to define the surface orientation.*

Define θ (ranging from 0 to 180°) as the angle between $\mathbf{c}$ and the surface normal:

$$\theta = \text{acos}\left(\frac{\mathbf{n}\cdot\mathbf{c}}{|\mathbf{n}||\mathbf{c}|}\right) \tag{5.8}$$

As the angle between $\mathbf{b}$ and the surface normal depends on the orientation of the molecular plane, define the *roll axis* $\mathbf{r}$ as:

$$\mathbf{r} = \mathbf{c} - \frac{|\mathbf{c}|^2}{|\mathbf{n}\cdot\mathbf{c}|}\mathbf{n} \tag{5.9}$$

This axis is in the plane spanned by $\mathbf{c}$ and $\mathbf{n}$, perpendicular to $\mathbf{c}$. Define ϕ as the

angle between **b** and this roll axis:

$$\phi = \mathrm{acos}\left(\left|\frac{\mathbf{b}\cdot\mathbf{r}}{|\mathbf{b}||\mathbf{r}|}\right|\right) \tag{5.10}$$

The dot product is taken in absolute value to constrain the range of ϕ betweeen $0°$ (**b** is in the plane spanned by **c** and **n**) and $90°$ (**b** is perpendicular to the plane spanned by **c** and **n**).

Having these two angles, define the *orientational distribution function* (ODF) as the number $n(\theta, \phi)$ of molecules with angles between $[\theta, \theta + d\theta]$ and $[\phi, \phi + d\phi]$ normalised by the corresponding area of a unit sphere with θ taken as the polar angle and ϕ as the azimuthal angle

$$\mathrm{odf}(\theta, \phi) = \frac{n(\theta, \phi)}{\sin\theta \, d\theta \, d\phi} \tag{5.11}$$

Calculating the orientational distribution function for all surface molecules and breaking it down by number and type of hydrogen bonds gives the distributions shown in Figure 5.17. Blue areas depict depletion with respect to uniform interior distribution (which is shown in yellow) while red areas portray enhancement. Figures 5.18 and 5.19 show the same data at a lower resolution, superimposed over a representation of the corresponding molecular orientation, to help interpret Figure 5.17. Here, the results for the 576 molecule layer are reported since this layer has better statistics than the 4000 molecule layer. The shape of the orientational distribution does not change considerably between the two system sizes.

Overall, the surface shows a depletion of θ larger than around $120°$, meaning that the molecules arrange in such a way that at least one hydrogen atom points towards the liquid phase. However, the picture is rather more complex when ϕ is taken into account. The broadest distribution of θ occurs at $\phi = 90°$, with the distribution becoming narrower as ϕ decreases. To understand the surface orientation in more detail, Figures 5.18 and 5.19 break it down by the type of hydrogen bonds a molecule forms with its neighbours.

When a molecule comes to the surface, it is mostly 4 coordinated (DDAA) and would like to remain so. The surface can still accommodate 4 H-bonded molecules by having the molecular plane parallel to the surface ($\theta \sim 90°$ and $\phi \sim 90°$). The molecule forms two donor bonds and one acceptor bond in the plane of the

surface, while the other acceptor bond is made towards the liquid. Figure 5.17 shows this trend by means of an enhancement of the ODF of DDAA close to $(\theta, \phi) = (90°, 90°)$. Figure 5.17 also shows the θ extent of DDAA's depletion region increasing to lower angles as ϕ decreases. In other words, the closer the molecular plane becomes to being perpendicular to the surface, the more large values of θ are suppressed, aligning the donor bonds towards the liquid phase.

When the molecule breaks a bond to become 3 H-bonded, the alignment is strongly influenced by whether that bond is an acceptor or a donor. If the molecule breaks an acceptor bond, it becomes a DDA, with (θ, ϕ) peaking at around $(60°, 90°)$; i.e. with the molecule arranged such that the hydrogen atoms point towards the liquid and the oxygen towards the vapour.

In the case of a DAA, the situation is reversed: one hydrogen and the oxygen are pointing towards the liquid, one hydrogen towards the vacuum. It is here we see the close link between hydrogen-bonding and surface orientation – if DDA didn't dominate over DAA, the overall surface ODF would have had a second peak in the region around $(\theta, \phi) = (120°, 0°)$.

Finally, the existence of the DDA-DAA asymmetry in both the interior and surface regions strongly suggests that it is the molecular scale mechanism for the surface orientation of water. In other words, hydrogen bonds are intrinsically asymmetric. This underlying asymmetry manifests itself in two ways. In the bulk, it leads to 5 H-bonded, DDAAA species. At the surface, it preferentially orients the water molecules in such a way that the oxygen is predominantly pointing towards the gas phase, to satisfy the propensity for breaking acceptor bonds.

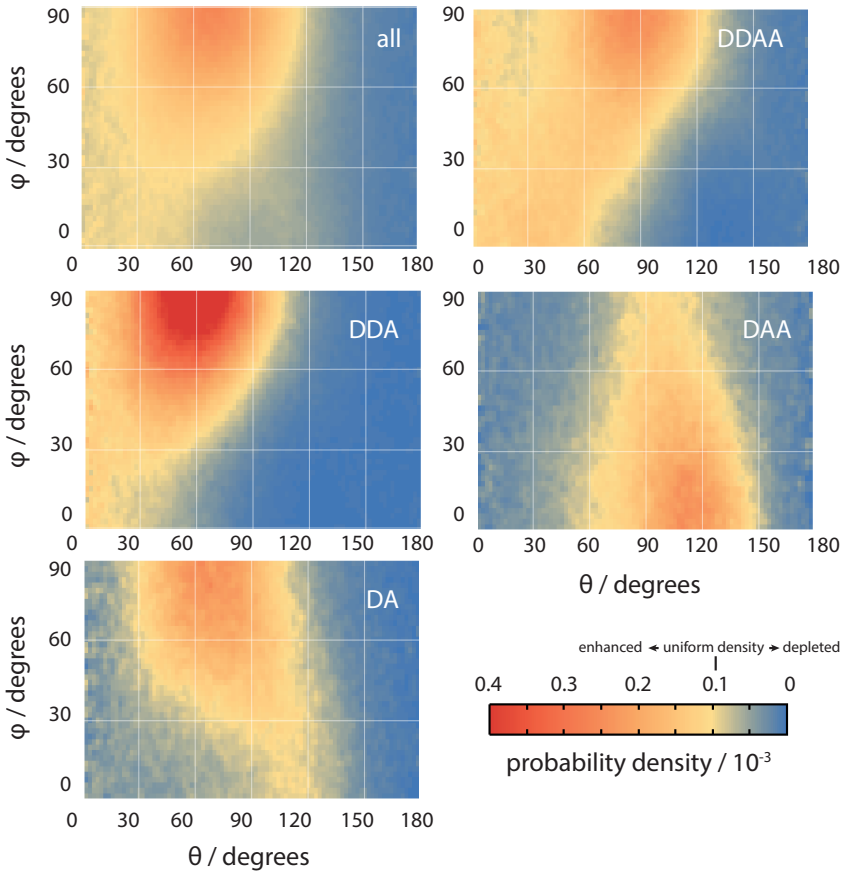

Figure 5.17 *The orientational distribution function of all surface molecules (top left) and of molecules with various hydrogen bonding configurations (labelled by DDAA, DDA, DAA and DA). Yellow represents uniform probability, orange and red represent enhancement and blue depletion.*

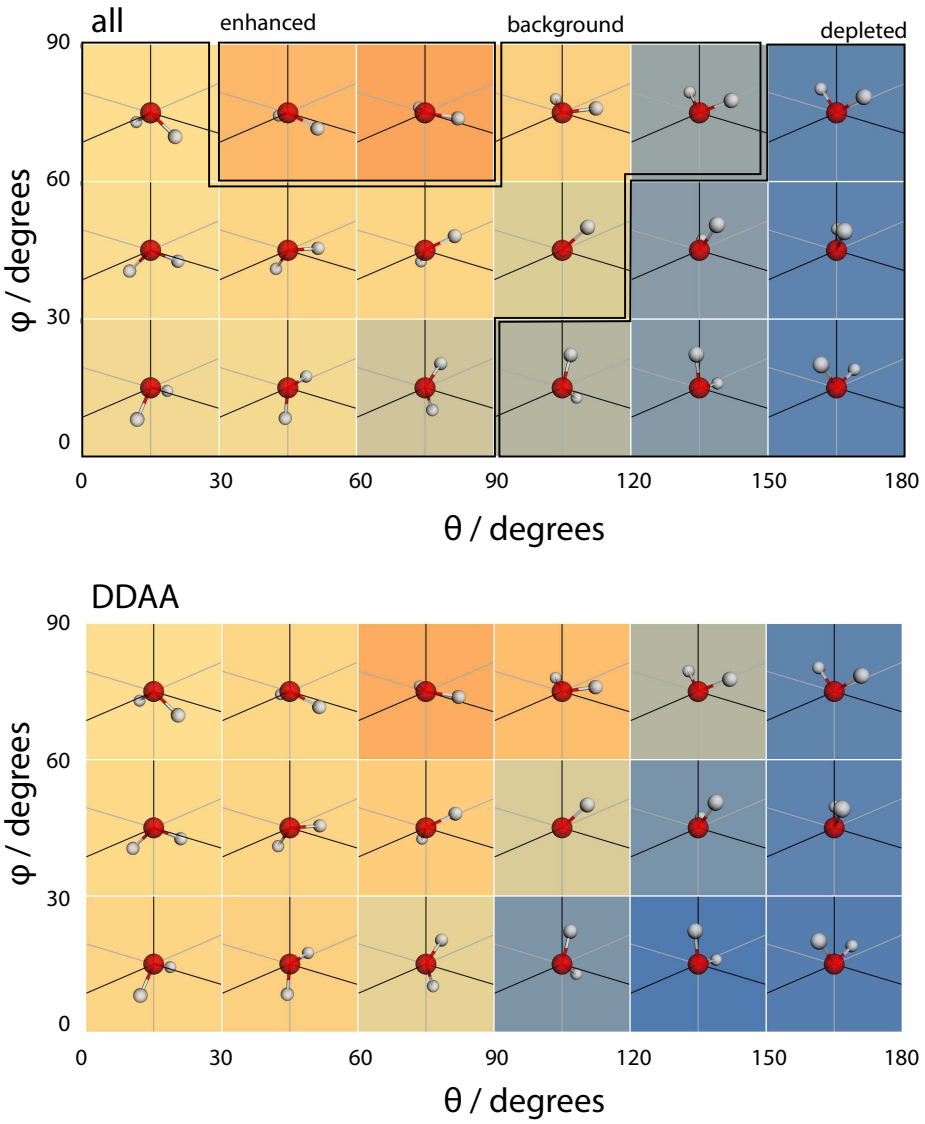

Figure 5.18 *A coarse version of the orientational distribution function (for all molecules and DDAA configurations) superimposed over illustrations of the orientation of water molecules at the given* (θ, ϕ) *pairs.*

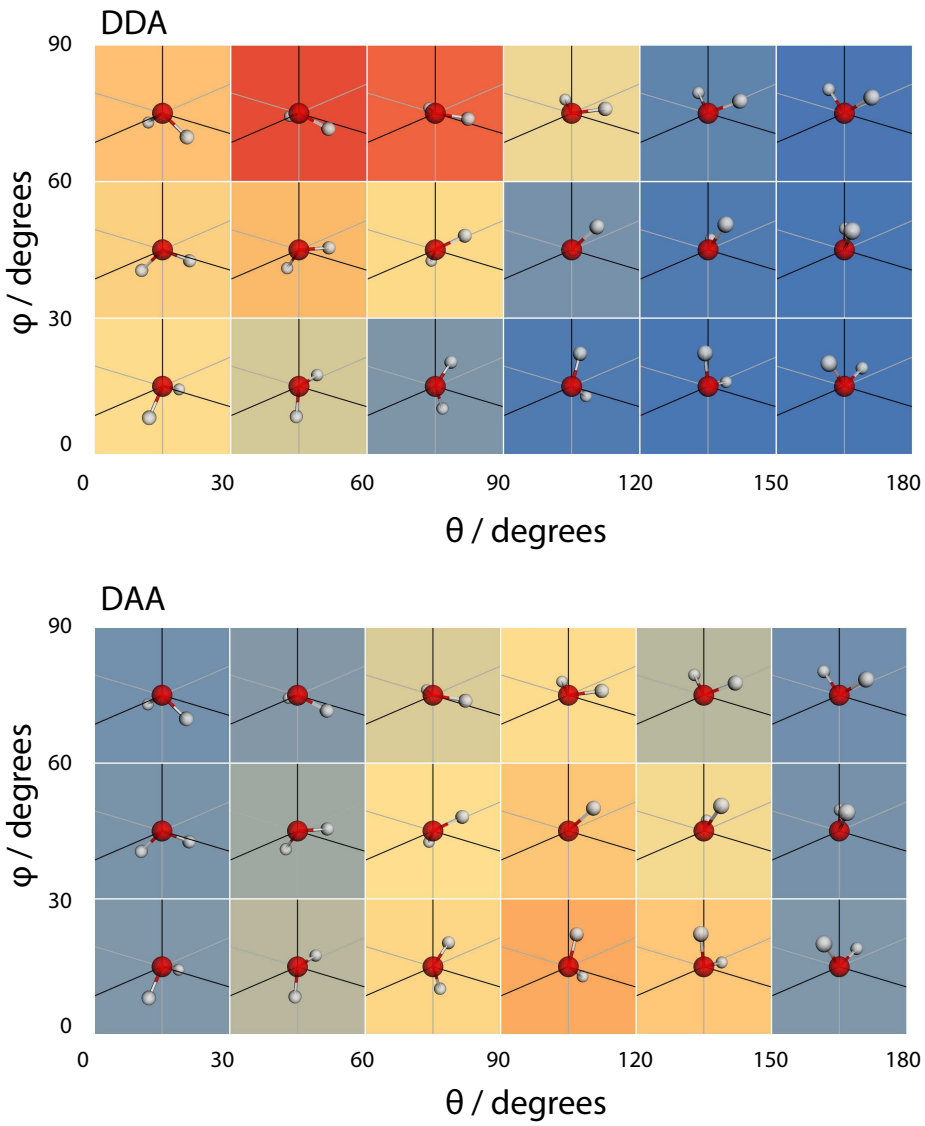

Figure 5.19 *A coarse version of the orientational distribution function (for DDA and DAA configurations) superimposed over illustrations of the orientation of water molecules at the given (θ, ϕ) pairs.*

5.3.7 Surface potential

A preferential orientation of water molecules at the liquid-vapour interface will result in a change in electrostatic potential between the liquid and the vapour phase. The value of the surface potential is important since it influences the chemical potential of any particle traversing the interface. In this section, the surface potential of QDO-water is calculated and compared with experiment.

Calculating the charge distribution

Assume a collection of classical point charges q_i,[1] at positions $z(q_i)$. The charge density $\rho(z_n)$ is defined over a lattice, with each z_n corresponding to the z coordinate of the centre of a slice. Assuming the simulation box ranges from $-z_{\max}$ to $z_{\max}$ with n_{slices} slices, the thickness of each slice is:

$$dz = \frac{2z_{\max}}{n_{\text{slices}}}$$

and

$$z_n = -z_{\max} + \left(n + \frac{1}{2}\right) dz$$

with n ranging from 0 to $n_{\text{slices}} - 1$.

Under these assumptions, define the piecewise averaged charge density to be

$$\rho(z_n) := \frac{1}{V_{\text{slice}}} \sum_i q_i \left[|z(q_i) - z_n| \leq \frac{dz}{2} \right] \tag{5.12}$$

where $[S]$ is the Iverson bracket defined as:

$$[S] = \begin{cases} 0 & \text{if } S \text{ is false} \\ 1 & \text{if } S \text{ is true} \end{cases}, \tag{5.13}$$

and V_{slice} is the volume of each slice (assumed constant).

We'll begin by assuming a continuous charge distribution $\rho(z)$ and then adapt the final results to the discrete function $\rho(z_n)$.

[1] Note that the QDO charges have a certain Gaussian width. Therefore, to be completely correct we should include that width in the calculation. Kathmann et al. [135] show that the charge width does influence the value of the surface potential. In our case though, as long as the bins are larger than the charge widths, assuming point charges should not influence the result by much.

Start with Poisson's equation in vacuum (we have no medium since all the charges are explicitly taken into the calculation).

$$\nabla^2\phi(z) = -\frac{\rho(\mathbf{r})}{\epsilon_0} \tag{5.14}$$

The charge density varies only along z, so Poisson's equation reduces to:

$$\frac{d^2\phi(z)}{dz^2} = -\frac{\rho(z)}{\epsilon_0} \tag{5.15}$$

Integrating once from $-z_{\max}$ to z' gives:

$$\left.\frac{d\phi(z)}{dz}\right|_{z'} - \left.\frac{d\phi(z)}{dz}\right|_{-z_{\max}} = -\frac{1}{\epsilon_0}\int_{-z_{\max}}^{z'} dz''\ \rho(z'') \tag{5.16}$$

Assuming that $-z_{\max}$ is far away from the surface, the electric field $E(-z_{\max}) = \left.\frac{d\phi(z)}{dz}\right|_{-z_{\max}} \equiv E_0$ is close to zero. However, at high temperatures, when the density of the liquid and gas phases approach each other, this boundary condition can't be guaranteed. We'll get back to this point when we look at the temperature dependence of the surface potential. For now, set $E_0 = 0$, giving:

$$\left.\frac{d\phi(z)}{dz}\right|_{z'} = -\frac{1}{\epsilon_0}\int_{-z_{\max}}^{z'} dz''\ \rho(z'') \tag{5.17}$$

Integrating again,

$$\phi(z) - \phi(-z_{\max}) = -\frac{1}{\epsilon_0}\int_{-z_{\max}}^{z} dz' \int_{-z_{\max}}^{z'} dz''\ \rho(z'') \tag{5.18}$$

Setting our reference (vacuum) potential at $-z_{\max}$ gives $\phi(-z_{\max}) = 0$. Thus,

$$\phi(z) = -\frac{1}{\epsilon_0}\int_{-z_{\max}}^{z} dz' \int_{-z_{\max}}^{z'} dz''\ \rho(z'') \tag{5.19}$$

Defining the surface potential

We define the surface potential as the potential drop between the liquid and the gas phases. Assuming that the point $z = 0$ is inside the liquid phase and $z = \pm z_{\max}$ is inside the gas phase, the surface potential is:

$$\chi = \phi(0) - \phi(-z_{\max}) = \phi(0)$$

since we've set our reference point at $-z_{\max}$.

In theory, the electric potential throughout the liquid phase should be constant (as long as the coarse graining length is larger than the typical molecule), since there are no electric fields over length scales larger than a typical molecule. However, due to sampling errors, the electric potential will vary. Thus, in practice, χ is calculated as an average over the liquid-like region of the lamella, with z coordinates ranging between $-z_{\text{cutoff}}$ and z_{cutoff}.

$$\chi = \frac{\sum_n [z_n > -z_{\text{cutoff}}] \cdot [z_n < z_{\text{cutoff}}] \ \phi(z_n)}{\sum_n [z_n > -z_{\text{cutoff}}] \cdot [z_n < z_{\text{cutoff}}]} \tag{5.20}$$

An aside about units

Let $\tilde{x}$ be the unit-less value of a physical quantity x. In our case:

$$\begin{aligned} z &= \tilde{z}\,\text{Å} \\ \rho &= \tilde{\rho}\,\frac{\tilde{e}\text{C}}{\text{Å}^3} \\ \epsilon_0 &= \tilde{\epsilon}_0 \frac{\text{C}}{\text{Vm}} \\ \tilde{e} &= 1.60217657 \times 10^{-19} \\ \tilde{\epsilon}_0 &= 8.85418782 \times 10^{-12} \end{aligned} \tag{5.21}$$

Thus,

$$\begin{aligned} \phi(z) &= -\frac{\tilde{e}}{\tilde{\epsilon}_0}\frac{\text{Vm}}{\text{C}}\text{Å} \times \text{Å} \times \frac{\text{C}}{\text{Å}^3} \int_{-\tilde{z}_{\max}}^{\tilde{z}} d\tilde{z}' \int_{-\tilde{z}_{\max}}^{\tilde{z}'} d\tilde{z}''\ \tilde{\rho}(\tilde{z}'') \\ &= (-180.9513\,\text{V}) \int_{-\tilde{z}_{\max}}^{\tilde{z}} d\tilde{z}' \int_{-\tilde{z}_{\max}}^{\tilde{z}'} d\tilde{z}''\ \tilde{\rho}(\tilde{z}'') \end{aligned} \tag{5.22}$$

Numerical integration

Now's the time to recognise that $\rho(z)$ is defined over a discrete lattice, with $\rho_k \equiv \rho(z_k)$. We'll use the trapezium rule to carry out the integrals and check convergence with respect to $dz = z_{n+1} - z_n$ (or alternatively, with n_{slices}):

$$\int_{-z_{\max}}^{z_n} \rho(z)\, dz \simeq \frac{1}{2} \sum_{k=0}^{n} (z_{k+1} - z_k)\, (\rho_{k+1} - \rho_k) \tag{5.23}$$

Symmetrising the charge distribution

In order to reduce the sampling errors, $\rho(z)$ was symmetrised (due to the geometry of the simulation, $\rho(z) = \rho(-z)$):

$$\rho(z) = \rho(-z) = \frac{1}{2} (\rho(z) + \rho(-z)) \tag{5.24}$$

Convergence of the numerical integration

Figure 5.20 shows the effect of increasing the number of slices on the electrostatic potential, which is superimposed over the density profile. We can see that $\phi(z)$ stays approximately the same when increasing the number of slices from 500 to 1000, indicating that the numerical integration has converged.

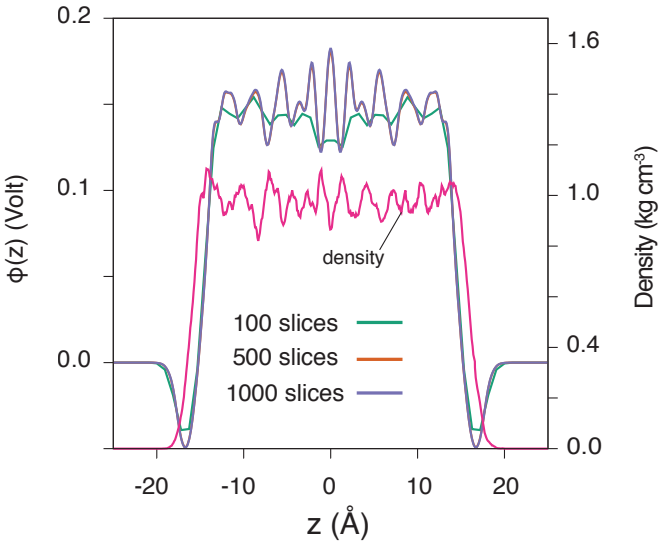

Figure 5.20 *Convergence of the potential $\phi(z)$ as a function of the number of z slices, at 300 K.*

We note that Figure 5.20 shows periodic fluctuations of both density and electrostatic potential. In a short simulation, a molecule cannot sample the entirety of the periodic box. Treating particles as point charges, their mass and charge will be localised in a single bin. With bin sizes around 0.1 Å, this localisation creates the observed fluctuations. Longer simulation combined with larger bin sizes should smooth the fluctuations. Indeed, this is the case for 100 slices where the fluctuations in electrostatic potential are considerably reduced.

The surface potential χ is calculated by averaging $\phi(z)$ in the region $[-10, 10]$, with the error estimated as the standard error of the mean associated with this calculation. Figure 5.21 shows the variation of χ with increasing n_{slices}, showing that its value has indeed converged by the time n_{slices} reaches 1000. This results in the best estimate for $\chi(300\,\text{K})$ of:

$$\chi(300\,\text{K}) = 0.1499(9)\,\text{V} \tag{5.25}$$

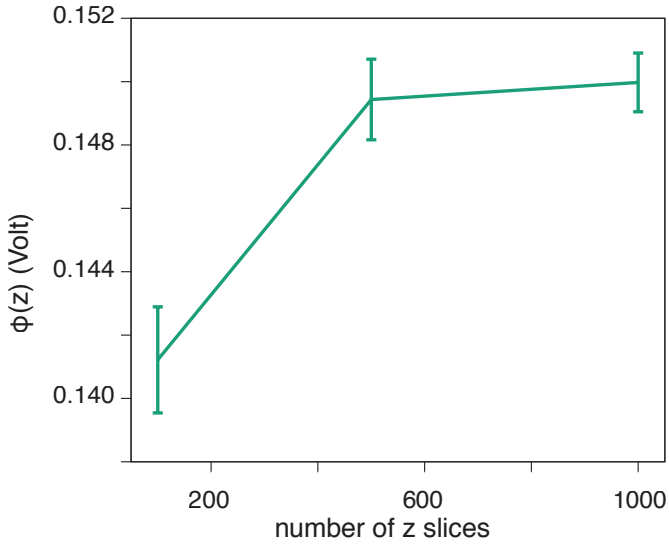

Figure 5.21 *Convergence of the surface potential as a function of the number of z slices, at 300 K.*

Temperature dependence

Now that it's established that the surface potential converges when using 500 slices and the charge density needs symmetrisation, let's look at the variation of the potential with temperature. Figure 5.22 shows the electric potential throughout the sample as a function of temperature.

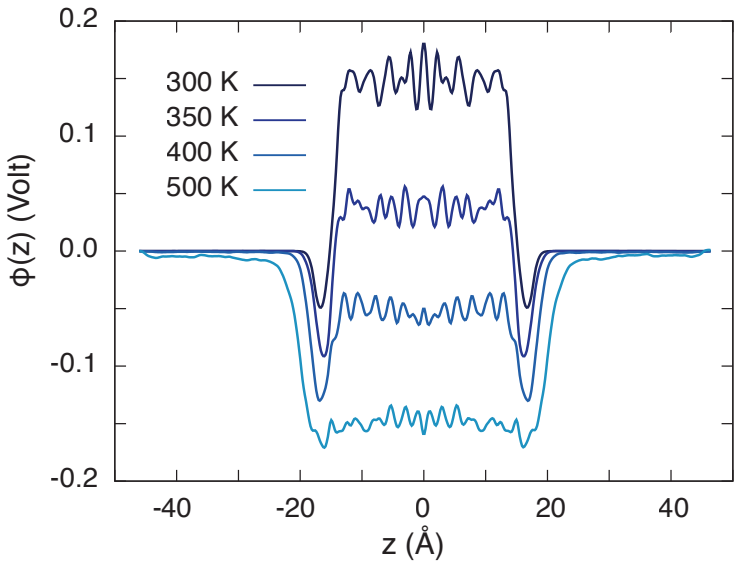

Figure 5.22 *Temperature dependence of the potential $\phi(z)$.*

To calculate the surface potential as a function of temperature, we average $\phi(z)$ between -5 and 5 Å in order to smooth out the variations of the potential in the bulk phase, giving the results shown in Figure 5.23

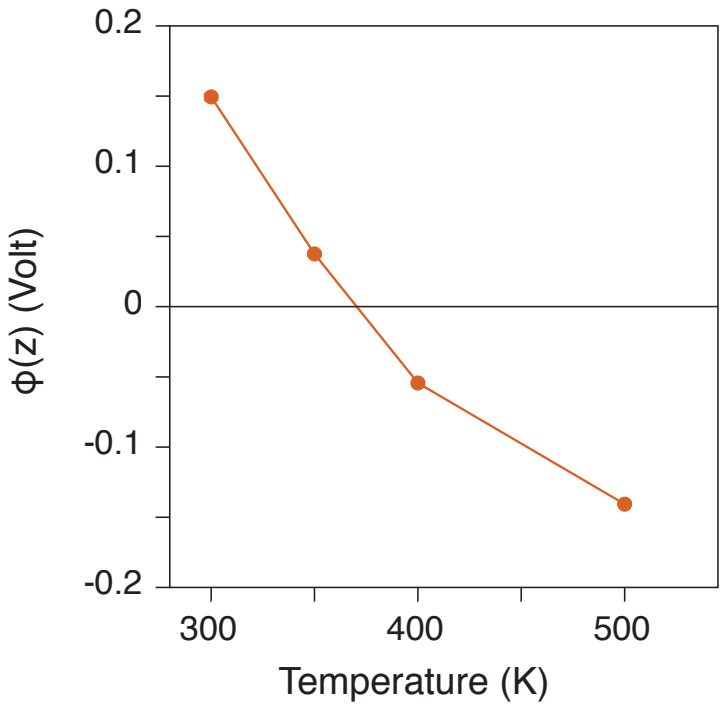

Figure 5.23 *Temperature dependence of the surface potential.*

One observation about Figure 5.23 is that the surface potential seems to change sign close to the boiling point of water. By fitting a straight line to the $T = 300$ K and $T = 400$ K points, we can calculate that:

$$\phi(T = 371 \text{ K}) = 0 \tag{5.26}$$

temperature that is within 1% of the boiling point of water. Despite looking interesting, this observation is likely an artefact of the nature of the model, as discussed in the next section.

Comparison with experiment and calculation

In the previous section, we showed that the surface potential of QDO-water ranges between -0.15 V and 0.15 V at temperatures between 300 K and 500 K. How does this compare with experiment and previous calculations? Figure 5.24 shows the values of the surface potential previously measured and calculated using various techniques.

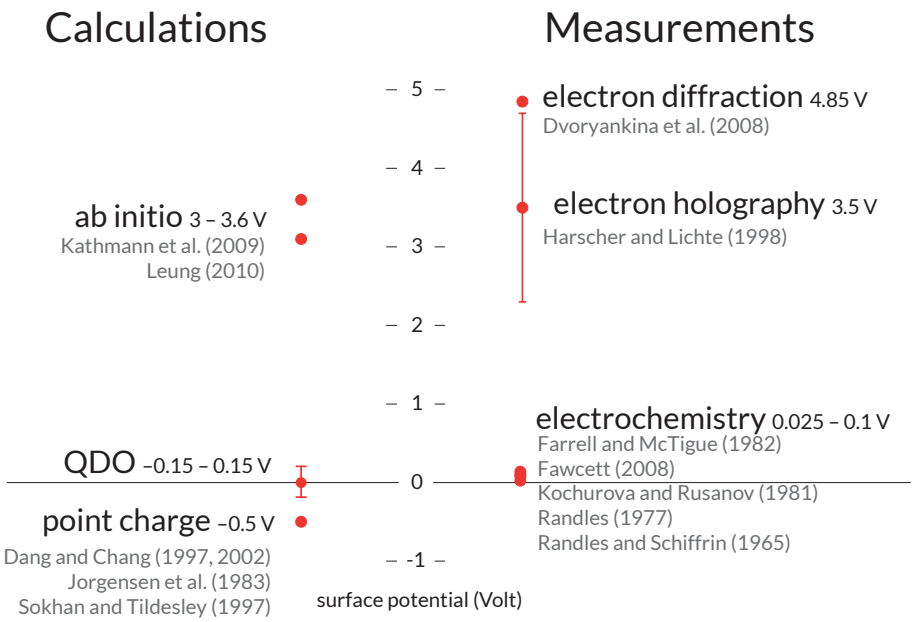

Figure 5.24 *Experimental and calculated values of the surface potential, including ab initio calculations [134, 155], point charge models [63, 64, 129, 253], electrochemical measurements [78, 79, 141, 218, 219], electron holography [100] and electron diffraction [72].*

Experimentally, the surface potential can be measured in two ways: either using

electrochemical probes or by using electrons [135]. An electrochemical probe, such as a hydrogen ion penetrates the space between the atoms and does not reach the regions close to the nuclei where the electric potential increases rapidly. Therefore, an electrochemical probe samples the mean external potential around the molecules.

On the other hand, electrons are light and energetic. When sent through a liquid, which can be modelled as a simple step potential, they acquire a phase shift which is proportional to the height of the potential barrier. This potential barrier is created by the mean internal potential of the liquid, including regions close to the nuclei (which are sampled by the energetic electrons).

Since electrochemical and electronic probes sample the surface potential differently, we expect the values they measure to be different. This is indeed the case: the electrochemical surface potential ranges between 0.025 and 0.1 V [78, 79, 141, 218, 219], while the electronic surface potential ranges between around 2–5 V [72, 100].

Calculating the surface potential from electronic densities reported by DFT and averaging over the whole space is expected to produce a surface potential closer to electronic than electrochemical probes. This is indeed the case, with the DFT surface potential ranging between 3.1 and 3.6 V. [63, 64, 129, 253]

On the other hand, atomistic models containing empirical point charges report a surface potential of around -0.5 V. This discrepancy is caused by the nature of the models, as explained by Kathmann et al. [135]. They are parametrised such that the average long-range interactions produce a realistic condensed phase at the desired thermodynamic conditions. However, this parametrisation says nothing about the accuracy of the charge distribution of each molecule. Consider a model such as TIP4P/2005. It contains two positive point charges on the hydrogen atoms and a negative point charge on the M site, situated on the HOH bisector. The electric potential close to these charges will have a large divergence (which is typically damped in simulations). Thus, when calculating the average potential in the interior region, this near-divergence close to the point charges will introduce fictitious terms. In real molecules (and DFT, which produces a realistic charge distribution, albeit an unrealistic structure), the molecular charge distribution is spread out over the van der Waals radius of the molecule. Thus, once a sampler reaches a region close to the nuclei, the electronic potential will have been damped at values smaller than the corresponding point-charge model with the same long-

range electrostatic.

While QDO-water has a diffuse charge distribution introduced by the QDO, it still retains the artefacts created by the rigid frame of point charges that reproduces the responses of the isolated molecule. Thus, by this argument, we expect QDO-water to have a surface potential closer to electronic samplers (thus, around 3 V) than point charges. However, the surface potential of QDO-water is close to electrochemical experiments, even if it was calculated using a method that is best compared to electronic samplers.

Despite results that look interesting, the values of the surface potential of QDO-water cannot be trusted to be an accurate representation of real water. The main reason is the artefact introduced by the point charges: despite the fact that the model is responsive and has an extended charge distribution, it does however suffer from the same problem of other models containing point charges, namely the lack of screening of the charge distribution of the isolated molecule.

The results can be made more realistic in two ways, which could be explored in future work. First, one could assume that the *polarisation* of QDO-water is realistic, even if the charge distribution of the isolated molecule is not. Let $\rho(\mathbf{R})$ be the charge distribution at a point R inside, say, the liquid state. By replacing each molecule with its corresponding ground state distribution, we arrive at $\rho_0^{\mathrm{QDO}}(\mathbf{R})$, which is the charge distribution at a point R assuming that each molecule had the same charge distribution as when isolated. Then, $\rho(\mathbf{R}) - \rho_0^{\mathrm{QDO}}(\mathbf{R})$ is the *polarisation* density, showing how much the charge distribution of each molecule changed due to its neighbouring molecules. To restore a realistic charge distribution, we need to add $\rho_0^{\mathrm{ab-initio}}(\mathbf{R})$, which is the charge distribution of a molecule calculated using ab initio methods, such as DFT. Then, $\rho(\mathbf{R}) - \rho_0^{\mathrm{QDO}}(\mathbf{R}) + \rho_0^{\mathrm{ab-initio}}(\mathbf{R})$ would give a more realistic representation of the charge distribution inside a liquid sample, potentially removing the artefacts added by the presence of point charges.

Another method of making the surface potential of QDO-water more realistic is to, rather than sample the electronic surface potential, sample the electrochemical one. To do so, one would have to average the electronic potential inside the liquid at points which are "outside" the molecules. This can be done using a certain cutoff, say at distances larger than R_c from each oxygen and hydrogen atom. The results can then be converged with respect to R_c, resulting in a surface potential than can be more accurately compared with electrochemical measurements.

5.4 Conclusion

This chapter presented an application of QDO-water to the study of water's liquid-vapour interface. This system was chosen since it is the simplest heterogeneous system and has both technological and fundamental importance. Previous molecular models failed to reproduce the surface tension, disagreed on the orientation of water molecules and resulting surface potential, disagreed on whether the surface has a significant fraction of acceptor-only molecules and on the decay length of the dipole moment. All these questions are important to answer for a fundamental understanding of what happens when water's network of hydrogen bonds is truncated to form a surface and an ability to engineer this surface for applications such as on-water catalysis.

First, the model was shown to generate a physical liquid-vapour interface. The surface tension, from ambient temperature to the critical point, is shown to match experiment to 2%. Similarly, the densities of the liquid and gas branches at coexistence pressure are within 1% of experiment, with a critical point and temperature of maximum density one error bar from experiment. Furthermore, the surface molecules at 300 K exhibit a mean molecular dipole moment ranging from 2.52 D (at 90% density) to 2.34 D (at 10% density), with the interior value being 2.6 D. It's important to note that all of these quantities are *predictions* of QDO-water, which was parametrised from the properties of the isolated molecule and a single cut through the dimer energy surface. This stands in contrast to atomistic models such as TIP4P/2005, which use the condensed phase properties as a fitting target.

One quantity that does not match experiment well is the surface potential. It ranges from ~ 0.15 V at 300 K to ~ -0.15 V at 600 K, with a value of zero close to the boiling point of water at ambient pressure, 373.15 K. This compares well with electrochemical measurements, which report a surface potential ranging from 0.025 V to 0.1 V. However, the method of calculation, which averaged the electric potential throughout the liquid centre of the lamella, should be compared to electronic holography and diffraction measurements, which report values between 3–4 V. The discrepancy is due to the point charges forming the frame of the model, which result in unphysical divergences in the potential in their close neighbourhood. I presented two ways of dealing with this: average the potential outside the molecules or make the charge distribution more physical by using a reference ab initio calculation.

Second, the hydrogen bond network is found to be truncated at the liquid–vapour interface preferentially on the hydrogen acceptor side. This truncation leads to a depletion of all molecular orientations with both hydrogen atoms dangling towards the gas phase, resulting in a surface where 98% of the molecules have at least one bound hydrogen (and thus a negligible population of acceptor only species). These observations agree with the conclusions of Kühne et al. [145], with our simulations of TIP4P/2005 and SFG experiments but are at odds with the simulations of Kuo et al. [149] and TIY-XAS experiments concerning the presence of acceptor-only species. This analysis shows that the surface of QDO-water has a negligible fraction of acceptor only molecules.

I have also identified two other hydrogen-bonding motifs: a preference for DDA over DAA configurations and the appearance of 5 hydrogen-bonded species. Since this preference is present in both the interior and surface regions and for TIP4P/2005, the intrinsic hydrogen bonding asymmetry between acceptor and donor bonds is the molecular scale mechanism leading to the observed surface orientation at the free interface.

The observation of an underlying asymmetry in hydrogen-bonding adds to the growing body of evidence that liquid water's structure is more asymmetric than a simple perturbed tetrahedral network [101, 294] and that hydrogen bond acceptors and donors have different instantaneous contact strengths [143, 144].

Chapter 6

Supercritical water

Molecular-Scale Remnants of the Liquid-Gas Transition in Supercritical Polar Fluids
Sokhan, Jones, Cipcigan, Crain, Martyna. PRL 115 (11) 2015.

6.1 Importance and the different crossovers

When water is heated above its critical temperature of 647 K, the distinction between liquid and vapour vanishes, resulting in a single, *supercritical* phase. The existence of this phase has been known for over 100 years [42], with both fundamental and technological interest.

Technologically, supercritical water is interesting because of two properties: it can dissolve *nonpolar* molecules [6], thus being able to replace toxic organic solvents, and its density can be continuously tuned between that of a liquid and a gas. Other supercritical fluids such as CO_2 have been used routinely for processes such as dissolving caffeine from coffee.

At the molecular level, supercritical water consists of small water clusters embedded in a gas-like phase. Locally, it maintains the structure of liquid water yet globally it expands to fill a space like a gas would. This breakdown of the hydrogen-bonded network makes supercritical water have a low dielectric constant and a low energetic penalty for the disturbance of hydrogen bonds, which collaborate to make it a good solvent for organic molecules.

Despite the lack of a phase transition, supercritical water contains regions of liquid-like and gas-like properties [36, 82, 83]. These have been separated using various boundaries in the phase diagram (some are sketched in Figure 6.1): the critical isochore, the maxima in thermodynamic responses (also known as the Widom lines [82]) and a dynamic crossover (known as the Frenkel line [36]). These boundaries coincide close to the critical point and diverge at higher pressures and temperatures.

In this chapter, supercritical water is studied using QDO-water from the point of view of the relationship between its molecular structure and crossover between liquid-like and gas-like regions.

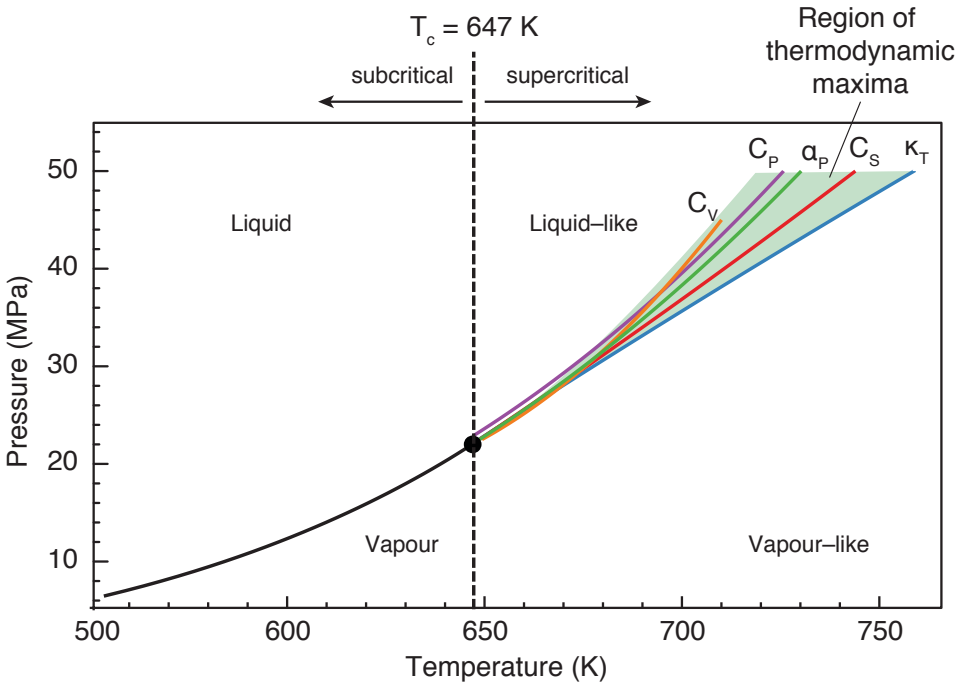

Figure 6.1 *The liquid-vapour coexistence curve (black line) ending in the critical point (black point). Above the critical temperature of 647 K water is in a supercritical state, with no transition between liquid and vapour. A region separating liquid–like and gas–like states in supercritical water is defined by the maxima in thermodynamic responses [82]: isochoric, isobaric and adiabatic heat capacity (C_V, C_P and C_S), isobaric thermal expansion (α_P) and isothermal compressibility (κ_T). Coexistence curve obtained from NIST/IAPWS [154, 287] and maxima in thermodynamic responses from Imre et al. [117]. The locus of the Frenkel line for water is still unknown.*

6.2 Simulation setup

The properties of supercritical water were sampled in the NVT ensemble across one subcritical isotherm (600 K) and three supercritical ones (673 K, 773 K and 873 K). A cubic unit cell was initialised with liquid-like configurations at densities ranging from 5 to 60 mol/l in steps of 5 mol/l. The resulting unit cells were equilibrated for 5–10 ps and sampled for 10–100 ps. Typical simulations used a timescale separation factor of $\gamma = 16$. Due to fluctuations close to the critical point, this had to be increased to $\gamma = 64$ at 673 K and $\gamma = 32$ at 773 K.

The cumulative average of the components of the pressure tensor was monitored for convergence and the average of the diagonal components was reported as the pressure of the system. The trajectories were then analysed to calculate the radial distribution function, average dipole moment and probabilities of hydrogen bonded motifs using the custom trajectory analysis software I developed.

6.3 Experimental validation

6.3.1 Isotherms

To check whether the model produces a realistic supercritical liquid, its pressure as a function of density in the NVT ensemble is calculated at four temperatures: 600 K, 673 K, 773 K and 873 K. The latter three temperatures are supercritical at all densities while the first is supercritical at densities larger than around 35 mol/l. The resulting density as a function of pressure superimposed over the experimental benchmark (NIST/IAPWS–95 [154, 287]) is shown in Figure 6.2. The agreement with experiment is good over a broad range of temperatures, including in the vicinity of the critical point where critical fluctuations require larger separation of timescales between nuclear and electronic degrees of freedom.

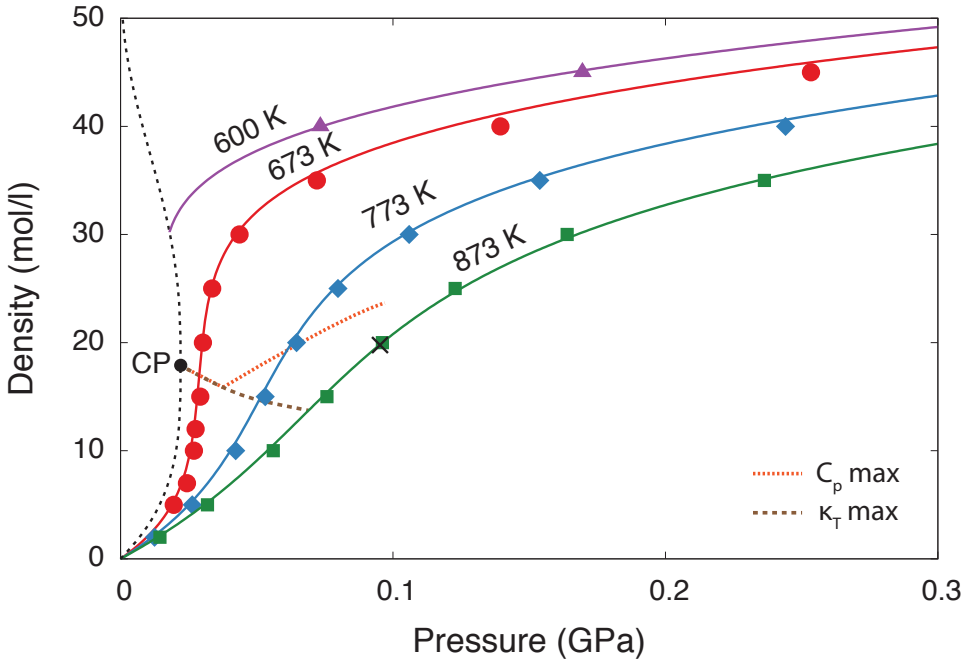

Figure 6.2 *Isotherms of supercritical QDO water at 600 K (triangles), 673 K (circles), 773 K (diamonds) and 873 K (squares). The points are calculated values while the lines are NIST/IAPWS–95 experimental data [154, 287]. The dotted line is the liquid-vapour coexistence curve of water [154, 287] ending in the critical point, labelled CP. The errors are calculated using bootstrapping [9] and are smaller than the size of the points. The dashed lines emerging from the critical point are the loci of the isobaric heat capacity C_p and isothermal compressibility κ_T, marking the Widom lines.*

6.3.2 Radial distribution function

To assess the validity of the structure, Figure 6.3 shows the radial distribution functions at 673 K as a function of temperature and compared with the experimental data of Soper [257]. At all densities the radial distribution functions show a large first peak, indicative of the existence of a first shell. This shows the presence of some tetrahedral order even in the low density structures, which is one of the signatures of a supercritical phase (i.e where the vapour starts showing liquid-like characteristics). As the density increases, the second shell forms at around 40 mol/l. The formation of a second shell can be seen as a further observable separating liquid-like and gas-like regions of supercritical water. Furthermore, the radial distribution functions with a formed second shell compare well with the experimental benchmark [257] at 647 K and 48.4 mol/l.

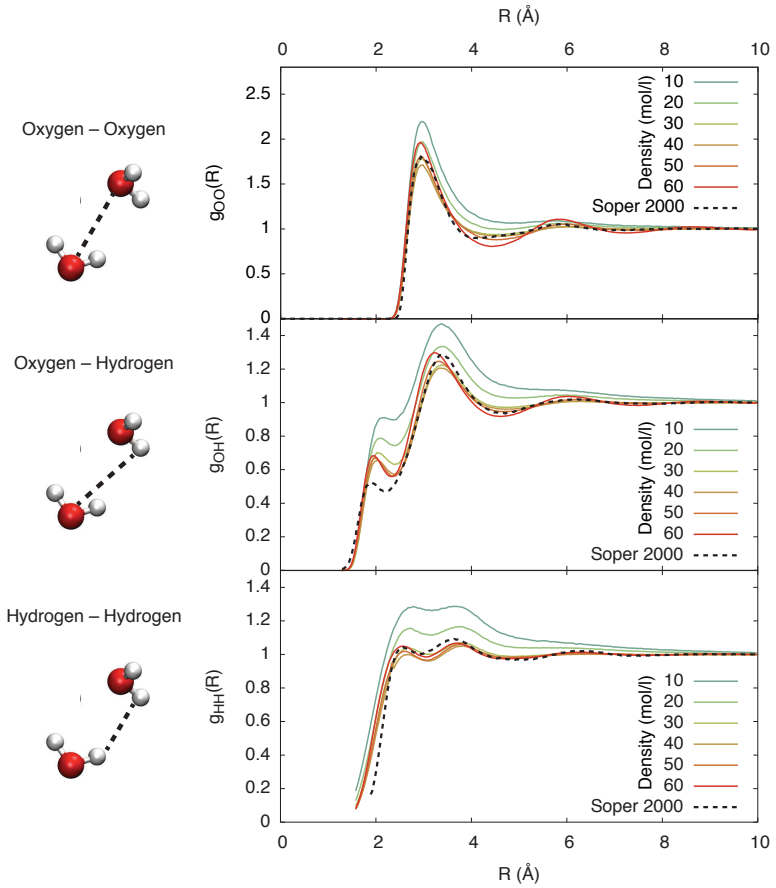

Figure 6.3 *Radial distribution functions of QDO-water at 673 K (supercritical) as a function of density. The dashed line marks the experimental radial distribution function at 673 K and 340 MPa [257], corresponding to a density of 48.4 mol/l.*

6.4 Molecular structure of supercritical water

6.4.1 Dipole moment in the condensed phase

The dipole moment is a reporter of local structure and one of the unique observables provided by QDO-water. Since supercritical water is a liquid over a large range of densities, we expect the dipole moment to vary considerably, reflecting the density and cooperativity of the local environment. Figure 6.4 shows the dipole moment as a function of density at 673 K, 773 K and 873 K.

The main feature of Figure 6.4 is a crossover, where the gradient of the dipole moment as a function of density changes quickly. The strength of this crossover decreases with increasing temperature, with the most marked behaviour close to the critical point (at 673 K). The crossover density occurs in the region of 15–20 mol/l for all the temperatures considered, with 673 K consistently lower than 773 K and 873 K. This density region coincides with the region of maxima in isothermal compressibility. Therefore, the crossover in the dipole moment is a further signature of the transition region between liquid-like behaviour and gas-like behaviour. Both of these regions have a dipole moment that linearly varies with density, but with a different gradient and y intercept.

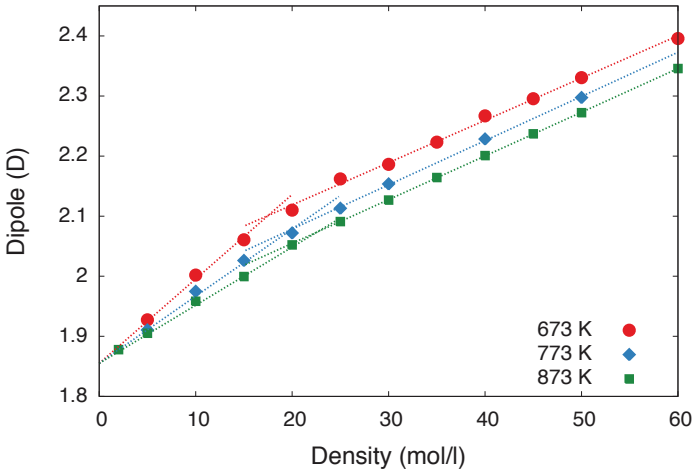

Figure 6.4 *The dipole moment as a function of density on the three isotherms: 673 K (circles), 773 K (diamonds) and 873 K (squares). The dotted lines are linear fits to the regions where the dipole moment varies linearly with temperature.*

6.4.2 Hydrogen boding

The hydrogen bonding motifs are a further way of quantifying the molecular structure of supercritical water. The hydrogen bonding motifs are calculated by first assigning hydrogen bonds using the method of Kumar et al. [147], explained in Section 5.3.4. This method assigns a hydrogen bond to any pair of molecules whose oxygen–oxygen distance R and oxygen–hydrogen–oxygen angle θ is inside the contour of the potential of mean force in R and θ enclosing the smallest R saddle point. A bond from a hydrogen atom of a molecule to an oxygen atom of another is a donor bond while a bond from an oxygen to a hydrogen is an acceptor bond. Each motif is labelled with letters indicating how many acceptor and donor bonds it has – for example, DA is a motif with one donor and one acceptor bond. Probabilities of these motifs are averaged over all of the atoms and the entirety of the trajectory and plotted in Figure 6.5 as a function of density at 673 K.

These probabilities show a few interesting trends. First, the asymmetry between acceptor and donor bonds that was identified inside the bulk liquid and at the liquid-vapour interface persists in supercritical water, increasing in magnitude with increasing density. This asymmetry can be used as an indicator of liquid-like regions – the asymmetry increases quickly with density above 20 mol/l, which is in the crossover region at 673 K.

Molecules with no hydrogen bonds (N) are the most abundant motif (30%) at low densities ($\sim$ 10 mol/l), decreasing quickly with increasing density. A intermediate densities (20-40 mol/l), two-hydrogen bonded motifs (DA) begin to dominate. These peak at 30 mol/l, followed by the dominance of three hydrogen-bonded motifs (DDA and DAA) at densities larger than 50 mol/l. This cascade shows the hierarchical ordering of water molecules. Low densities are dominated by low-coordinated molecules (with two or three hydrogen bonds), while high densities have a well connected hydrogen bonded network similar to the subcritical liquid. Thus, the structure of the hydrogen bonded network reflects the gas-like nature of low density regions and liquid-like nature of high-density regions.

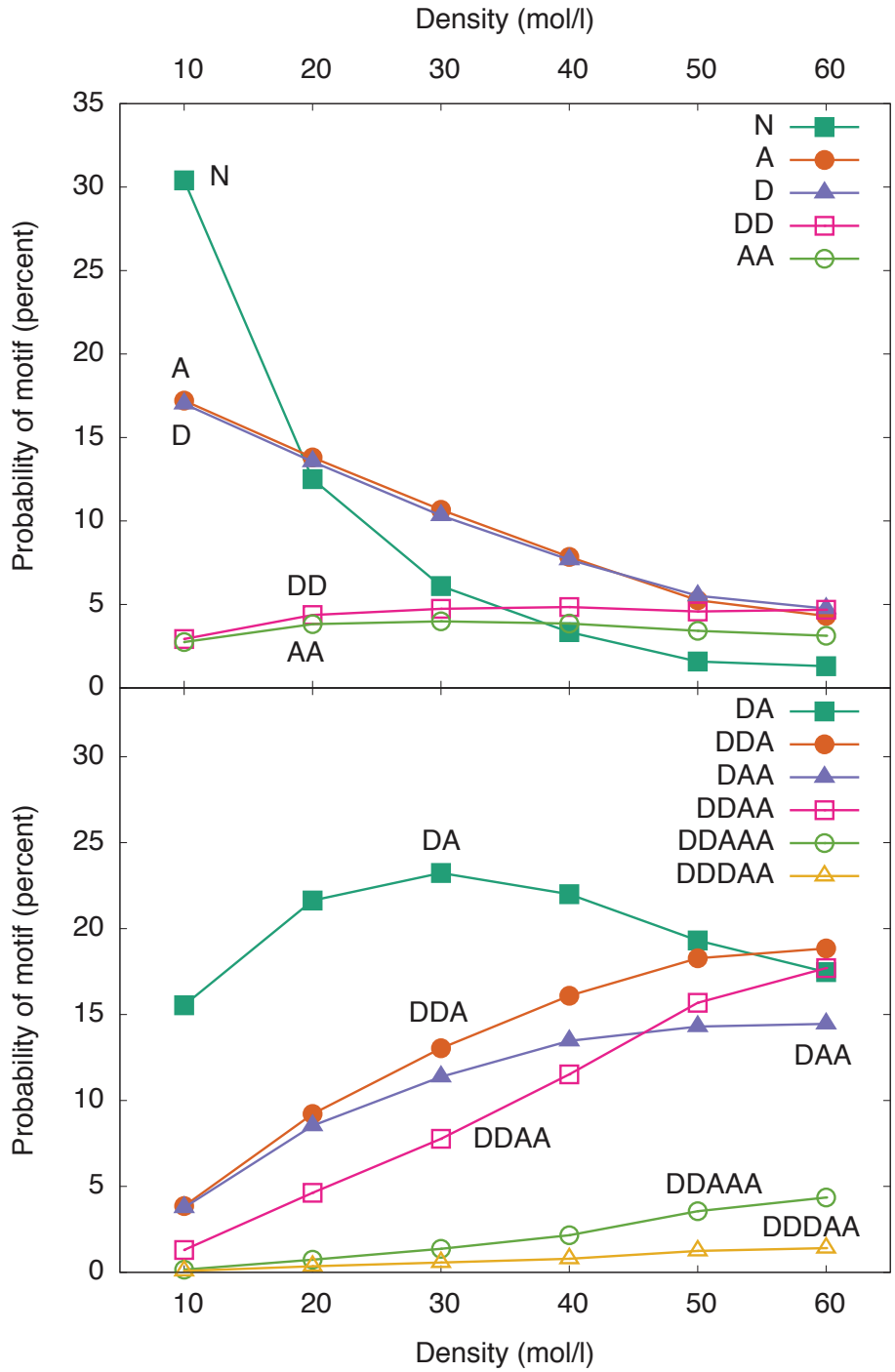

Figure 6.5 *The probability of a given hydrogen bond motif as a function of density at a constant temperature of 673 K.*

6.4.3 Conclusion

This chapter presented an application of QDO-water to supercritical water, a system chosen as an example of the fluid phase in an extreme environment. Supercritical water served to both test the transferability of the model and as a chance to understand the physics behind various crossovers extending from the critical point.

The pressure as a function of density on three supercritical isochores was shown to be predicted accurately by QDO-water, extending its transferability from ice II and the liquid-vapour interface into supercritical water.

Alongside a good match with experiment, the molecular structure was investigated. A crossover between liquid-like and gas-like regions which is observed in both dynamic and thermodynamic responses was confirmed at the molecular level using two order parameters: the molecular dipole moment and hydrogen bonding. The molecular dipole moment shows a cusp in a region close to where the thermodynamic responses display a maximum (the Widom line). The hydrogen bonding shows a continuous transition from gas-like structure to four-coordinated liquid-like structure, with two signatures of a crossover: the probability of DA configurations displays a maximum in the transition region and the asymmetry between DAA and DDA present in the liquid appears at densities above the crossover.

Chapter 7

Supercooled water

Structure and bonding at the limits of liquid water stability
Cipcigan, Sokhan, Martyna, Crain. in prep.

7.1 Importance of studying supercooled water

A supercooled liquid is formed when the liquid is cooled below its freezing temperature. In this region, the crystal is the thermodynamically stable phase. However, without a nucleation site, crystallisation faces a large energy barrier since it requires a global rearrangement from a low symmetry to a high symmetry phase. The energy barrier makes supercooled water metastable on a timescale influenced by a competition of two effects: the relaxation times of liquid water, whose rate of increase with cooling increases below the freezing point and the similarity of the local environment to the stable phase [161]. This competition defines a *homogeneous nucleation temperature* where the local environment is similar enough to the stable crystal phase so that thermal fluctuations alone can drive crystallisation on timescales below those accessible in the laboratory. Below the homogeneous nucleation temperature, supercooled water exists only on small timescales and may not even reach equilibrium before the onset of crystallisation [48, 158, 161], making both experiment and simulations complicated to perform and interpret.

Understanding supercooled water is important for two key reasons.

The first reason is fundamental. Upon supercooling, the response functions of water such as heat capacity and isothermal compressibility increase rapidly and *appear* to diverge just below the temperature of homogeneous nucleation [67]. The reason for this apparent divergence is yet unclear. The prevailing hypothesis links this effect to a liquid-liquid phase transition between the two competing local structures in liquid water occurring in no man's land – the region of the phase diagram where the homogeneous nucleation timescale is faster than the experimental one. While such a liquid-liquid transition has been observed in network-forming liquids such as phosphorous [133], fast nucleation still blocks experiments on liquid water. However, the liquid-liquid transition hypothesis is supported by both simulation and experiments using various techniques to suppress freezing, such as confinement in nanopores [61] and mixtures with salts [35] or glycerol [189]. The hypothesis is also supported by the existence of multiple phases of glassy water, separated by what looks like a first order transition [89]

However, the responses close to a liquid-liquid transition are similar to those close to a liquid-solid transition. Indeed, competing theories suggest that the homogeneous nucleation temperature puts a fundamental limit to the existence of a liquid, with the liquid phase being unstable (rather than just metastable) below this temperature [159, 161]. This hypothesis suggests that the increase of responses in supercooled water is due to the volume and entropy fluctuations created by the homogeneous nucleation of ice within the sample through a process of *coarsening*, just as you would have when approaching a liquid-gas spinodal.

Indeed, homogeneous nucleation is a key process to study in itself, with insights into the microscopic nature of phase transitions. In water it is made particularly interesting by the negative thermal expansion. The crystal has a lower density than the liquid, which means that individual crystallites must expand upon freezing and expel the remaining water between them. This process is still under study, enabled by computationally cheap models of water [184]. The results give interesting insights into the physics of water and ice, such as: the discovery of an intermediate metastable solid phase acting as a precursor to ice Ih [232], the observation of five-fold symmetric defect boundaries in homogeneously nucleated crystals [156], and the discovery that surface freezing is an important effect in micron-sized droplets of water [264]. However, the process of nucleation requires timescales longer than what QDO-water can attain, limiting the focus to the metastable phase.

The second reason to study supercooled water is practical. Supercooled water is an important player in global climate, being part of medium and high altitude clouds [264]. Depending on the temperature, these clouds are formed of either entirely supercooled water (down to −15°C), a mixture of supercooled water and ice (down to about −45°C) or entirely ice (below about −45°C). Water clouds contribute to overall warming, trapping heat from the atmosphere. On the other hand, ice clouds contribute to cooling. Only recently the effect of mixed-phase clouds on equilibrium climate sensitivity (the amount of warming caused by a doubling of atmospheric carbon to pre-industrial levels) has been understood, [267] increasing the previous estimates of 2.0–4°C to 5–5.3°C.

7.1.1 Experiments reveal large increase in thermodynamic responses upon supercooling

Observations of supercooled water date back to the 1700s, when Joseph Black [34] observed that "stirring gently with a quill tooth-pick" water left on a windowsill in freezing conditions, lead to "fine feathers of ice forming on its surface". Starting in the 1970s, the existence of apparatus better controlled than "the outside of a north window on one day of a calm and clear frost" lead to measurements of the responses of supercooled water down to the homogeneous nucleation temperature of water and up to pressures of 400 MPa. [13, 67, 111, 182] These measurements used microscopic samples to reduce the number of nucleation events – either thin films, capillaries or droplets. Collectively, the measurements revealed two anomalies [67]. First, the constant pressure heat capacity and isothermal compressibility increased upon cooling, appearing to have a maximum or divergence at around -45°C at atmospheric pressure. Second, increasing pressure reduced the magnitude of this anomaly.

The measurements lead to a wave of theories, summarised in Figure 7.1.

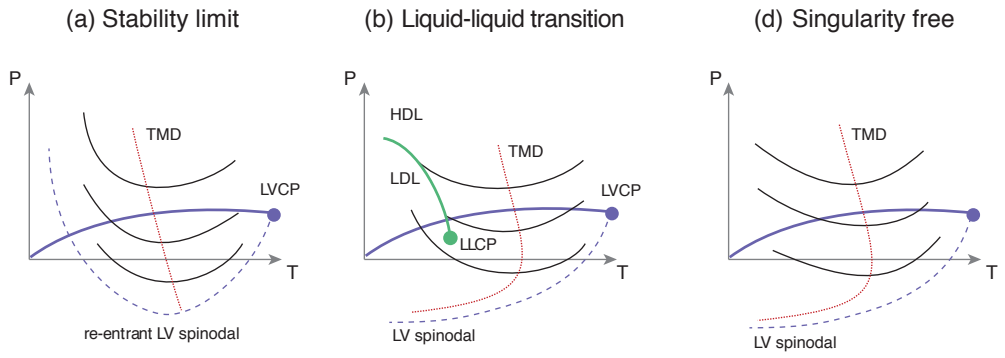

Figure 7.1 *Three hypotheses explaining the behaviour of supercooled water. (a) The stability limit conjecture [260] postulates a liquid-vapour (LV) spinodal emanating from the liquid-vapour critical point (LVCP) and retracing at positive pressure due to an intersection with the temperature of maximum density (TMD) line. (b) The liquid-liquid transition hypothesis [212] postulates a first order transition between a low density liquid (LDL) and high density liquid (HDL), ending in a liquid-liquid critical point (LLCP) that can lie at either positive or negative pressure. (c) The singularity-free hypothesis [239] postulates no anomalies, with the maxima in thermodynamic responses being a consequence of the existence of a TMD.*

The first explanation was motivated by a thermodynamic argument. The locus of temperature of maximum density (TMD) in the pressure-temperature plane has a negative gradient. If this trend continues and the TMD line intersects the liquid-vapour spinodal at negative pressure, this spinodal should have a minimum. This implies it should retrace back at positive pressure upon supercooling, creating a line of instability that leads to a maximum in responses [260].

The second explanation was motivated by experiments on glassy water. In the early 1990s, cooling water at rates higher than 10^6 K s^{-1} lead to the overshooting of the homogeneous nucleation temperature and formation of *two* types of glassy water: low density amorphous (LDA) and high density amorphous (HDA) [11]. LDA and HDA are separated by what looks like a first order phase transition controlled by pressure, with LDA being the low pressure phase. The natural extension of the phase transition between two glassy phases of water is a first order transition between two liquids: a low density liquid (LDL) and high density liquid (HDL) [212]. This transition occurs at temperatures below the homogeneous nucleation, in the so-called "no man's land", where liquid water is not viscous

enough to be glassy, while the crystal nucleation timescales are of the order of milliseconds. In order for the transition to remain hidden by homogeneous nucleation, the driving field must change from pressure to temperature as the temperature is increased, with a critical point postulated to be at positive pressure.

The current experimental picture is more complicated than two amorphous phases, with at least three types of amorphous ices being discovered [167] and with experiment suggesting that the transition between LDA and HDA might not be first order [11, 279]. Chandler [48] suggests that these ices are path-dependent forms of arrested liquid water rather than corresponding to multiple underlying liquid phases.

The third explanation was again motivated by thermodynamic arguments. A maximum (as opposed to a divergence) of thermodynamic responses does not need a critical point. It only needs the existence of a density maximum, which water has at 4°C [154]. Therefore, instead of viewing the density maximum as a consequence of a liquid-liquid phase transition, it is taken as fundamental, a consequence of water's competition between hydrogen bonds and van der Waals forces, with the increased responses emerging as a thermodynamic necessity. [239]

How do these hypotheses stand to experiment, simulation and further theoretical advances?

As noted before, experiments in no man's land are challenged by the fast timescales for nucleation. Nonetheless, the tools required to do such ultrafast experiments have been developed in recent years [22, 44, 102, 103, 243, 244, 263, 308]. These tools are based on dropping micron-sided droplets of water in a vacuum, in the path of a pulsed x-ray beam. As the droplets travel, they quickly cool via evaporation, with the temperature controlled by the distance they travel. Some droplets reach the x-ray beam at temperatures below homogeneous nucleation while still liquid, resulting in an x-ray spectrum of the liquid in no man's land.

These ultrafast experiments reached temperatures down to $-51°$ C [243, 244], but they did not reveal any signatures of a transition between two liquids. The spectrum measured in these experiments shows two peaks between 525 and 530 eV. The 1b1' peak (around 526 eV) corresponds to low-density local order while 1b1" (around 527 eV) corresponds to high-density local order (Figure 7.2) [244]. When approaching a transition, the low density peak should grow while the high

density peak shrink. However, the measurements show little change in height of the peaks from 290 K (ambient water) to 226 K (near the limit of homogeneous nucleation) and 222 K (in no man's land). This suggests two explanations: either the local structure of water changes little upon supercooling, which is unexpected if we assume the approach to a phase transition or Widom line; or the current interpretation of x-ray spectra is incomplete.

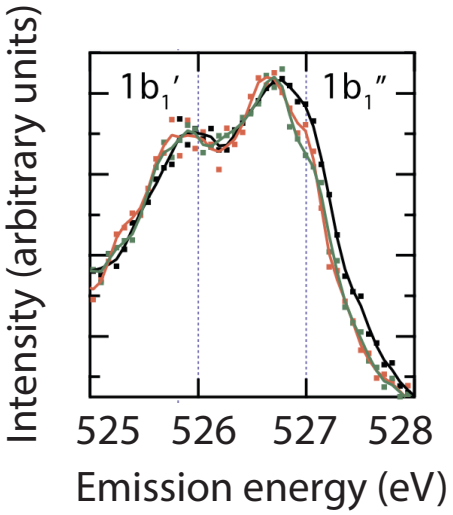

Figure 7.2 *X-ray emission spectrum of D_2O at 290 K (black), 226 K (red) and (222 K) (green), reproduced from Sellberg et al. [244]. There is little variation in the spectrum over this range of temperatures.*

A second avenue for experimentally testing the hypotheses explaining the behaviour of supercooled water is to put it under negative pressure. Stretched water is a second form of metastable liquid water, this time metastable with respect to the gas phase. As with supercooled water, it is employed by nature, this time in the trunks of tall trees, which generate large pressure gradients in order to transfer the nutrients from the roots to their tops.

Experiments with negative pressure water reached −140 MPa using micron-sized inclusions of water in naturally-occurring quartz crystals [17, 44–46, 66, 104, 200]. When heated, water fills the inclusions. Upon cooling, the liquid follows an isochore and starts to exert tension on the walls when the equilibrium volume becomes smaller than the volume of the cavity. Brillouin spectroscopy is used to measure the sound velocity and therefore the compressibility, with the pressure as a function of temperature being determined by fits to simulations of molecular models such as TIP4P/2005.

A third way of experimentally accessing no man's land is to stabilise liquid water against crystallisation. This can be done by enclosing water in nanopores [61, 291, 292], of diameter ranging from 2 to 6.5 nm or by mixing water with salts or glycerol, which inhibit crystallisation [35, 61, 189]. Both these experiments show evidence of a liquid-liquid phase transition. However, since surface effects are dominant in confined water and the ions might change the phase behaviour, the results are not easy to extrapolate to pure water. An example of this lack of transferability between confined and bulk liquid is mW, a monoatomic model of water. mW has a liquid-liquid transition when confined, but has *no* such transition in the bulk phase [185].

A fourth possibility, as yet unexplored, is substrate enhanced supercooling. Certain liquid metals, such as gold-silicon adopt a 5-fold symmetry when on a surface enhancing this type of symmetry, such as the (111) face of silica [242]. Similar results were observed for water, with freezing behaviour being influenced by both surface charge [73] and surface hydrophobicity [107, 108]. Since water is a polar molecule, it is conceivable that electric fields can affect its freezing behaviour, both close to the surface and in the bulk, especially since the dielectric constant of water is an order of magnitude higher than that of ice (and increasing upon supercooling).

7.1.2 Thermodynamic models explaining the phase behaviour of supercooled water

While experiments have revealed that the thermodynamic responses increase rapidly upon cooling and have proposed three mechanisms to explain this, they have not clarified the microscopic origin of these anomalies. This is where theory comes in, answering the question of how water's molecular structure leads to its condensed phase behaviour.

There have been three major trends in theoretical modelling, focusing on different aspects of water's structure: strength of hydrogen bonds, local volume, and free energy of mixing of two different liquids. The first two assume nothing about the existence of two different liquid states while the third takes it as an assumption (though, the existence of two liquid states doesn't necessarily lead to a first order transition between them).

One of the early models begun with the assumption that molecules may find

themselves in two local environments: one with strong hydrogen bonds and one with weak hydrogen bonds. Starting from these assumptions, a free energy was constructed that had either a re-entrant spinodal or a liquid-liquid critical point, depending on the strength of the hydrogen bonds [213].

An alternative model does away with hydrogen bonds and partitions molecules into two different local environments: one of high density and one of low density and high ordering [268]. The high density environment has higher entropy, due to more possible arrangements while the low density environment has lower energy due to the more favourable hydrogen bonded configuration. Assuming only a Boltzmann-like partitioning of molecules in these local environments, the model predicts both thermodynamic (heat capacity, density and compressibility) and dynamic (viscosity) anomalies using only the room temperature molecular structure of water, thus providing an alternative to the picture involving a liquid-liquid transition.

A third model takes the existence of two distinct liquid species as a starting point. Starting from a mixture of two different species, a free energy is constructed taking into consideration their free energy of mixing [111, 112]. If the mixing has enough non-ideality, quantified by a non-ideal mixing term, the model can phase separate at low temperatures. On the other hand, this term can also be tuned to keep the two liquids mixed at all temperatures (a physical analogue is opposite of the case of polymers, which are hard to mix together due to the mixing term in the free energy).

7.1.3 Simulations of molecular models of water

An alternative to thermodynamic theories are molecular models. Since water is the simplest complex molecule, molecular models are plentiful. They range from many-body potentials parametrised from ab initio calculations [77, 114, 209] to point charges parametrised from condensed phase properties [98], to coarse grained models that treat the water molecule as a single particle [184]. In the next paragraphs, we'll focus on three of these: two with a liquid-liquid phase transition and one without.

One of the first models used to investigate the phase behaviour of supercooled water was ST2 [262]. It was first shown to have a spinodal that was not retracing to positive pressure and then that it has indications of a liquid-liquid phase

transition [212]. Clearer evidence was provided in further studies, estimating the critical point to be at $T_C = 232(4)$ K , $\rho_C = 0.99(2)$ g/cm^3 and $p_C = 167(24)$ MPa. [99, 163, 164, 201, 214, 309] The results were contested based on insufficient sampling [159, 160] but Palmer et al. [201] showed, using eight different sampling method, that the model does indeed have two metastable free energy minima separated by an energy barrier. The critique regarding a phase transition in a metastable system was also addressed by tuning the parameters of ST2 such that liquid-liquid phase separation occurs at temperatures above freezing, where both liquids are the stable phase [251].

A second model to exhibit a liquid-liquid phase transition is TIP4P/2005 [1], which was studied in two independent studies by Abascal and Vega [2] and Singh et al. [249]. The latter fit its calculated equation of state to the two-phase thermodynamic model of [112] and predicted a critical point at $T_C = 182$ K , $\rho_C = 1.017$ g/cm^3 and $p_C = 170$ MPa.

A third model is mW, a monatomic model of water [184]. The model was shown to not exhibit a liquid-liquid phase transition as the supercooled liquid cannot be equilibrated faster than the crystallisation timescale [185, 186]. However, when confined, mW *does* exhibit a liquid-liquid phase transition, showing that its transition is blocked by dynamics rather than by thermodynamic arguments [310].

7.1.4 Aims of the chapter

In light of the existing literature, this chapter aims to explore the behaviour of QDO-water in its supercooled region. One feature of this region to be careful about is the long equilibration times, created by the rapid increase in viscosity upon cooling. Because of this, the results of the model will be compared with experimental benchmarks where possible or with the results of other standard models. Furthermore, the simulation timescales will be compared with the relaxation times of real water. This chapter aims to establish the following:

1. Is the behaviour of QDO-water consistent with a liquid-liquid transition?

2. How does the local structure evolve upon cooling and supercooling?

7.2 Simulation setup

In order to answer these questions, the behaviour of the QDO-water was sampled over a wide range of the phase diagram in the NVT ensemble. A cubic unit cell was initialised with a 300 molecule liquid configuration that was previously equilibrated using TIP4P/2005. The QDO-water configuration was then left to equilibrate for ~ 100 ps.

Due to available computer time, I chose to focus on two isochores ($\rho_1 = 52.8002$ mol/l and $\rho_2 = 55.3173$ mol/l) and four isotherms ($T_1 = 175$ K, $T_2 = 190$ K, $T_3 = 200$ K, $T_4 = 230$ K). These densities and temperatures were the focus of the simulations for two reasons. First, the isotherms are close to the estimates of the liquid-liquid critical point of TIP4P/2005. Second, the isochores are at two special densities: the density of the negative pressure experiments of Pallares et al. [200] and the density of water at ambient conditions.

In order to see how the dynamical slowdown at these temperatures will affect the equilibration times, Figure 7.3 shows the relaxation time of real water [161] versus the total sampling time achieved in each simulation.

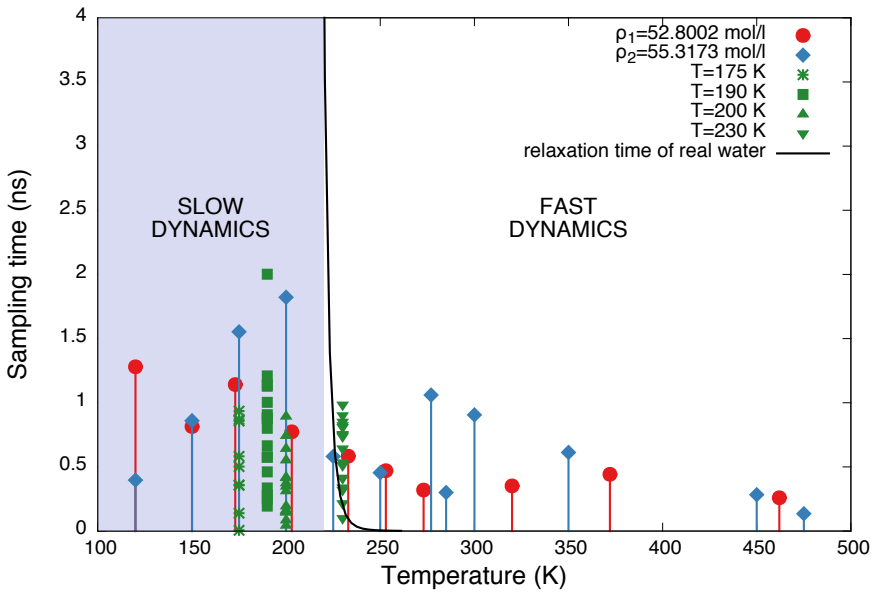

Figure 7.3 *The sampling time as a function of temperature for the isochores (red and blue symbols) and the isotherms (green symbols), compared with the relaxation time of real water, digitised from Limmer and Chandler [161].*

Real water relaxes on a timescale lower than a few nanoseconds at temperatures

above 220 K (-53 C). This is 15 K below the homogeneous nucleation temperature at atmospheric pressure (235 K), meaning that the simulations have a chance to equilibrate in water's no man's land. Indeed, if the extrapolations of the thermodynamic responses are correct, the maximum and thus the liquid-liquid critical line should occur at a temperature of 228 K at atmospheric pressure, in the region the simulations can access.

To help interpret the results in the following sections, blue shaded regions correspond to those where the sampling time is significantly lower than the relaxation time of real water. Simulations in these regions are not fully equilibrated but were performed to see whether there is any interesting physics that the model might suggest. Indeed, this will be the case - the only departures from previous benchmarks are at temperatures lower than 200 K, deep within the region where relaxation times in real water approach the millisecond timescale.

7.3 Do the simulations support a liquid-liquid transition?

First, let's look at whether the simulations support an approach to criticality. To do so, Figure 7.4 shows the pressure as a function of temperature and as a function of density on the isochores and isotherms sampled.

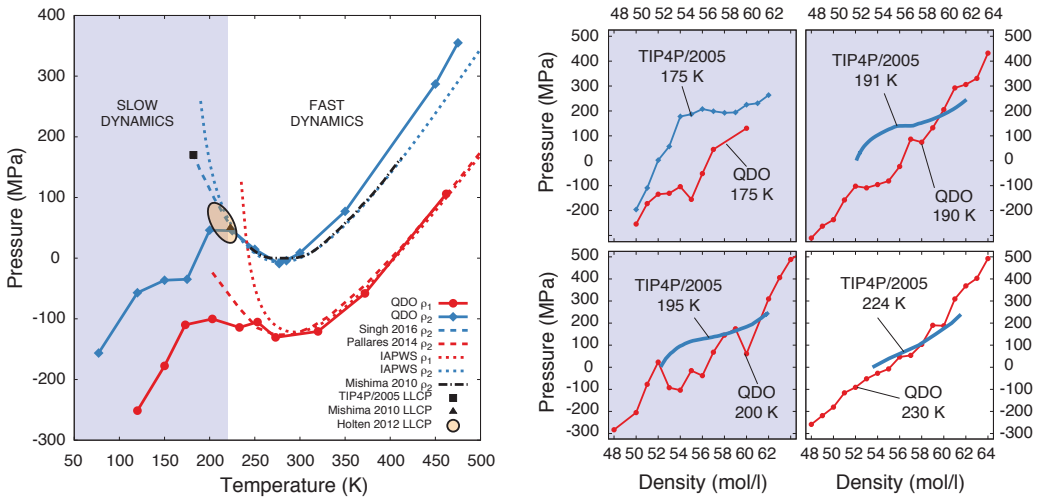

Figure 7.4 *(left) The pressure of 300 QDO-water molecules as a function of temperature at two constant volumes: $\rho_1 = 52.8002$ mol/l (red) and $\rho_2 = 55.3173$ mol/l (blue). The dashed lines represent equivalent data digitised from Singh et al. [249] (ρ_2 for TIP4P/2005) and Pallares et al. [200] (ρ_1, experimental estimates via simulations of TIP4P/2005). The dotted lines represent the corresponding isotherms of the IAPWS-95 reference equation of state for water [287]. The black dot-dashed line corresponds to an interpolated isochore based on the experimental data measured by Mishima [182]. The black square marks the liquid-liquid critical point (LLCP) of TIP4P/2005 [249] and the black triangle marks the LLCP estimated by Mishima [182] by fitting his data to Anisimov's [111] equation of state. The orange ellipse represents the estimate of the LLCP obtained by Holten et al. [111] by fitting Anisimov's equation of state to all available experimental data up to 2012. (right) The pressure of 300 QDO-water molecules as a function of density at four constant temperatures: $T_1 = 175$ K, $T_2 = 190$ K, $T_3 = 200$ K and $T_4 = 230$ K.*

For temperatures higher than about 250 K, the pressure as a function of temperature of QDO-water agrees with both experimental references [154, 182].

This situation demonstrates that the predictions of the model are realistic for supercooled water, since IAPWS-95 is expected to extrapolate reasonably well for low pressures and temperatures above homogeneous nucleation.

For temperatures close to and below the homogeneous nucleation temperature, we see a departure from the predictions of both IAPWS-95 and TIP4P/2005. While the pressure for both TIP4P/2005 and IAPWS-95 increases upon cooling, keeping the anomalous negative thermal expansion, the pressure of QDO-water shows a sharp decrease, reflecting a return to normal positive thermal expansion. This sharp downturn can be caused by the following two scenarios: one where the downturn is indicative of insufficient sampling and one where it is signature of new physics.

First, consider the effects of sampling. The downturn in pressure coincides with the onset of dynamics slower than the timescale of the simulation, meaning that we have to consider mechanisms where the results are an artefact of sampling.

Upon cooling, energy becomes dominant over entropy. This means that the population of water molecules in an ice-like, tetrahedrally-coordinated environment will increase upon cooling. This is indeed the case (as will be discussed in detail in the next sections) and is the molecular reason for the negative thermal expansion. However, the formation of tetrahedral cages requires a local reordering of the hydrogen bonds. In a region where the dynamics is slow, the reordering will happen on longer timescales that those of the simulation. Hence, the local density and the fraction of tetrahedrally-coordinated molecules will no longer increase upon cooling, restoring the observed normal positive thermal expansion. If this case were true, an increase in pressure as a function of simulation time should correlate with an increase in the fraction of tetrahedrally-coordinated molecules. Indeed, this is the case for a TIP4P/2005 simulation at temperatures close to its liquid-liquid critical point. Figure 7.5 shows the cumulative average of the pressure and tetrahedrality parameter Q, measuring the overall degree of tetrahedral coordination.[1] This simulation has an almost perfect correlation ($R^2 = 0.925$) between the cumulative average of the pressure and tetrahedrality, providing evidence for the slow relaxation of tetrahedral order in supercooled water.

[1] Q is 0 for a random arrangement and 1 for a perfect tetrahedral lattice. The parameter is defined in Section 7.5

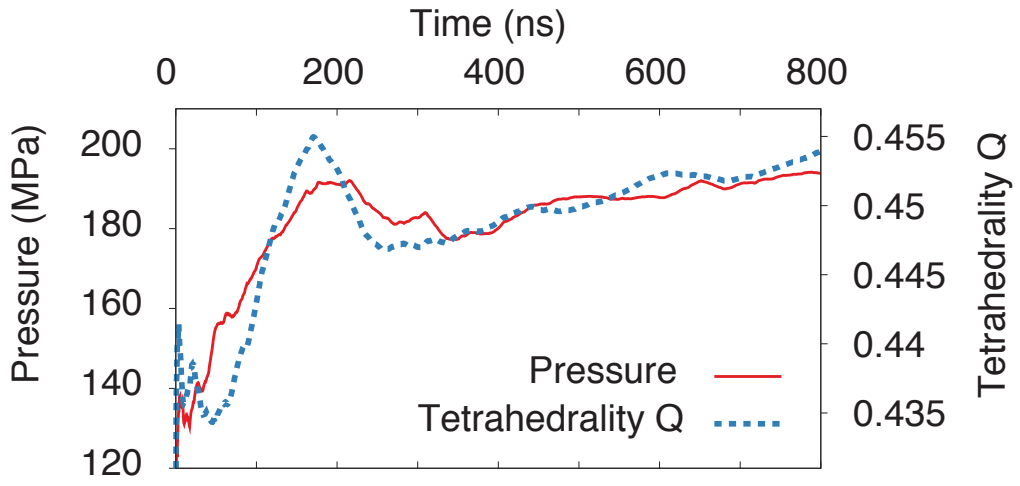

Figure 7.5 *The cumulative average of the pressure and tetrahedrality in an NVT simulation of TIP4P/2005 water at temperature $T = 175$ K and density $\rho_2 = 55.3173$ mol/l.*

Second, let's assume that the downturn in pressure is indeed a feature of the model and not one of short sampling. What scenario would it be consistent with? To do so, consider the behaviour of the model at constant temperature, as shown in the right hand side of Figure 7.4. The isotherm at 175 K is in the two-phase region of TIP4P/2005 while the isotherms at 190 K and 200 K are close to criticality. They are all within the region with slow dynamics, so again we expect to see the same considerations as previously: a slow relaxation of the tetrahedral order.

The major difference between TIP4P/2005 and QDO-water occurs in the region between ∼50 and 58 mol/l. At 175 K both models show a flattening of the pressure versus density, which is indicative of a divergent compressibility and hence a phase transition. However, QDO-water displays this flattening (albeit weakly) at negative pressure, while TIP4P/2005 displays it at positive pressure. A similar feature is seen at 190 K with the 200 and 230 K isotherms displaying normal behaviour of pressure increasing with density. This flattening in QDO-water suggests the existence of a liquid-liquid transition at negative pressure.

Since the three isotherms that differ between QDO-water and TIP4P/2005 all appear in the region where the dynamics is slow, it is worth thinking about how this difference can occur due to sampling artefacts. The central principle to

follow is again that *tetrahedral order equilibrates over timescales longer than the simulation*. This principle would need to explain why QDO-water agrees with TIP4P/2005 at densities below ∼50 mol/l and above ∼58 mol/l yet differs by as much as 400 MPa in the region between these two densities.

To do so, consider the structure of water at low, intermediate and high densities. As the density decreases, the formation of tetrahedral cages becomes more probable. Also, dynamics is faster at low density, since the local volume is closer to the preferred one and thus the Boltzmann factor related to the change from close-packed to tetrahedral is smaller than at higher densities. This all means that the equilibration of tetrahedral order is captured by the simulations of QDO-water.

The opposite picture emerges at high densities, where tetrahedral cages are suppressed by packing constraints. Thus, the tetrahedral cages that equilibrate on a long timescale are suppressed by the high density and do not contribute considerably to the pressure.

At intermediate densities, both populations of tetrahedral and close-packed local environments become important, with fluctuations between them giving rise to an increase in pressure. Due to the large energy barrier for interconversion, the short timescales do not sample these fluctuations, remaining "stuck" in the phase with structure similar to the high density liquid.

With all these in mind: does QDO-water have a signature of a liquid-liquid phase transition? In the region of the phase space accessible to simulation (i.e. above 220 K), no it does not: the isochores and isotherms show no characteristics of approaching criticality. This is consistent with both recent and not-so-recent experimental evidence. Bartell and Huang [22] measured the electron diffraction spectrum of molecular clusters consisting of around 6000 molecules and found a continuous transition from a liquid structure to that of cubic ice (ice Ic) down to temperatures of 200 K. More recently, Sellberg et al. [243] measured the x-ray diffraction [243] and emission [244] spectra of micron-sized water droplets down to 227 K and again, showed what looks like a continuous evolution of the structure towards that of LDA ice. Therefore, if a liquid-liquid critical point were to exist in both real water and QDO-water, it is likely to be below 220 K. Indeed, Mishima [182] estimates it to lie at 223 K and 50 MPa based on fitting the experimental data he gathered on supercooled water above the nucleation temperature and up to 400 MPa.

However, at the border between fast and slow dynamics, Figure 7.4 displays

tantalising evidence of a phase transition: the downturn in pressure. On the ρ_2 isochore (at ambient density), the downturn coincides with the estimates of a liquid-liquid critical point by both Mishima [182] and Holten et al. [111]. Instead of incomplete formation of tetrahedral cages, the downturn could be caused by an incomplete phase transition: a HDL-type local structure trapped in a region where LDL is thermodynamically stable. If we take the onset of the downturn to be indicative of the phase transition, then the results support a continuation of this transition to negative pressure. Indeed, this conclusion is also supported by the isotherms which show a weak flattening at negative pressure. Thus, the liquid-liquid critical point of QDO-water would be at negative pressures, as long as the current results survive the much-needed sampling of the dynamics to microseconds or more. There are a few ways this can be achieved, which will be discussed in the last chapter of this thesis.

7.4 Structure of supercooled water

Dipole moment

The dipole moment is a signature of the local structure. As we've shown in the previous chapter, a cusp in the dipole moment versus density or temperature marks a transition between local structures.

Figure 7.6 shows the variation of the average dipole moment as a function of temperature and density on the sampled isotherms and isochores. These results exhibit two interesting features: a cusp in the dipole moment as a function of temperature and a weak variation of the dipole moment with density relative to that with respect to temperature.

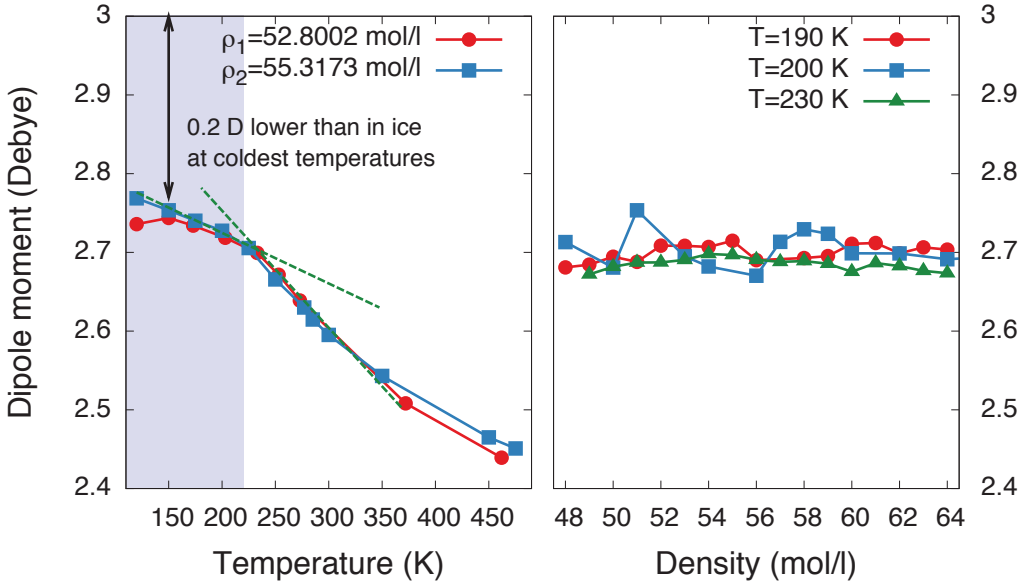

Figure 7.6 *The dipole moment as a function of temperature for two densities: $\rho_1 = 52.8002$ mol/l and $\rho_2 = 55.3173$ mol/l and three temperatures 190 K, 200 K and 230 K.*

First, let's consider the cusp in the dipole moment. This cusp coincides with two features of the model: the onset of slow dynamics of real water (meaning a lack of sufficient equilibration) and the crossing of the putative transition line identified in the previous section.

The dipole moment supports both scenarios. If tetrahedral order were suppressed by the timescales, then the increase in dipole moment with decreasing temper-

ature would be slower. Indeed, at the lowest temperature sampled, the model's dipole moment was still 0.2 D lower than that of ice, meaning that the four-coordinated network is still not fully formed. If the cusp marks a phase transition or the crossing of the Widom line of the liquid-liquid transition, we revert to a situation similar to that of supercritical water, where the dipole moment is a molecular signature of a phase transition.

Radial distribution function

The radial distribution function (RDF) enables a more detailed understanding of the local structure than the dipole moment. The isochores and isotherms show that the model produces a realistic condensed phase. To check whether it produces a realistic molecular structure, we compare the oxygen–oxygen radial distribution functions $g(r)$ to x-ray scattering experiments (performed by Skinner et al. [250]) in Figure 7.7 at three temperatures: ambient (285 K), maximum density (277 K) and supercooled (250 K). In order to visually compare the third and fourth coordination shells, $r^2(g(r) - 1)$ is plotted. This quantity is proportional to the enhancement in the number of molecules in a shell at a distance r from a molecule

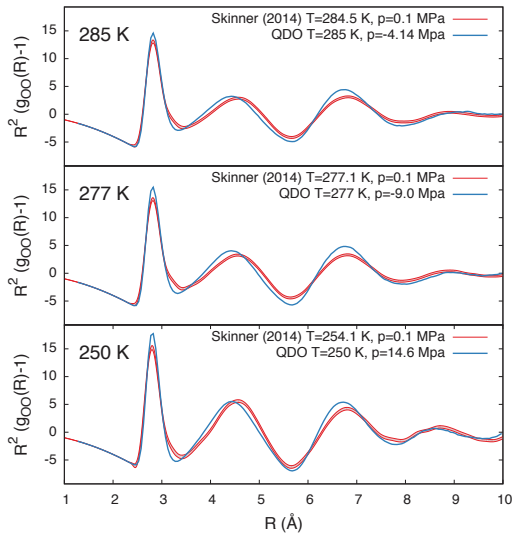

Figure 7.7 *The oxygen-oxygen radial distribution function of QDO water versus experiments by Skinner et al. [250] at three different temperatures. The red band represents experimental error margins while the blue line represents the radial distribution functions of QDO-water from NVT calculations at a density* $\rho_2 = 55.3173$ *mol/l.*

The figure reveals a good match between experiment and calculation, especially since the model was not parametrised to any specific thermodynamic conditions. The first three shells of QDO-water show a light overstructuring relative to experiment, which can also be caused by the fact that the thermodynamic conditions of simulation and experiment are slightly different.

After establishing that QDO-water produces a realistic supercooled liquid, we proceed to look at the evolution of structure as a function of temperature and density. To do so, Figures 7.8, 7.9 and 7.10 display the evolution of the radial distribution function along the two isochores and four isotherms.

These RDFs reveal two main features about the structure of supercooled water. The first feature is the major qualitative difference between the high temperature and low temperature structures. The first and second shell of the ambient and low temperature water are ice-like, with the first and second shell showing maxima similar to those found in the RDF of ice (black lines in the figures). However, at high temperatures the RDF of water becomes closer to that of a simple liquid with shells further apart than in the low temperature phase and in ice.

The transition from the low temperature to the high temperature structure reveals points where the RDFs are constant with respect to temperature. The first of these points were discovered in the experimentally measured oxygen-oxygen coordination numbers by Skinner et al. [250], who named them *isosbestic points*. Here we show the existence of multiple such isosbestic points (marked by dashed black circles), corresponding to each of the coordination shells. We also show that they persist at high temperatures, where the structure of the RDFs is vastly different than at low temperatures.

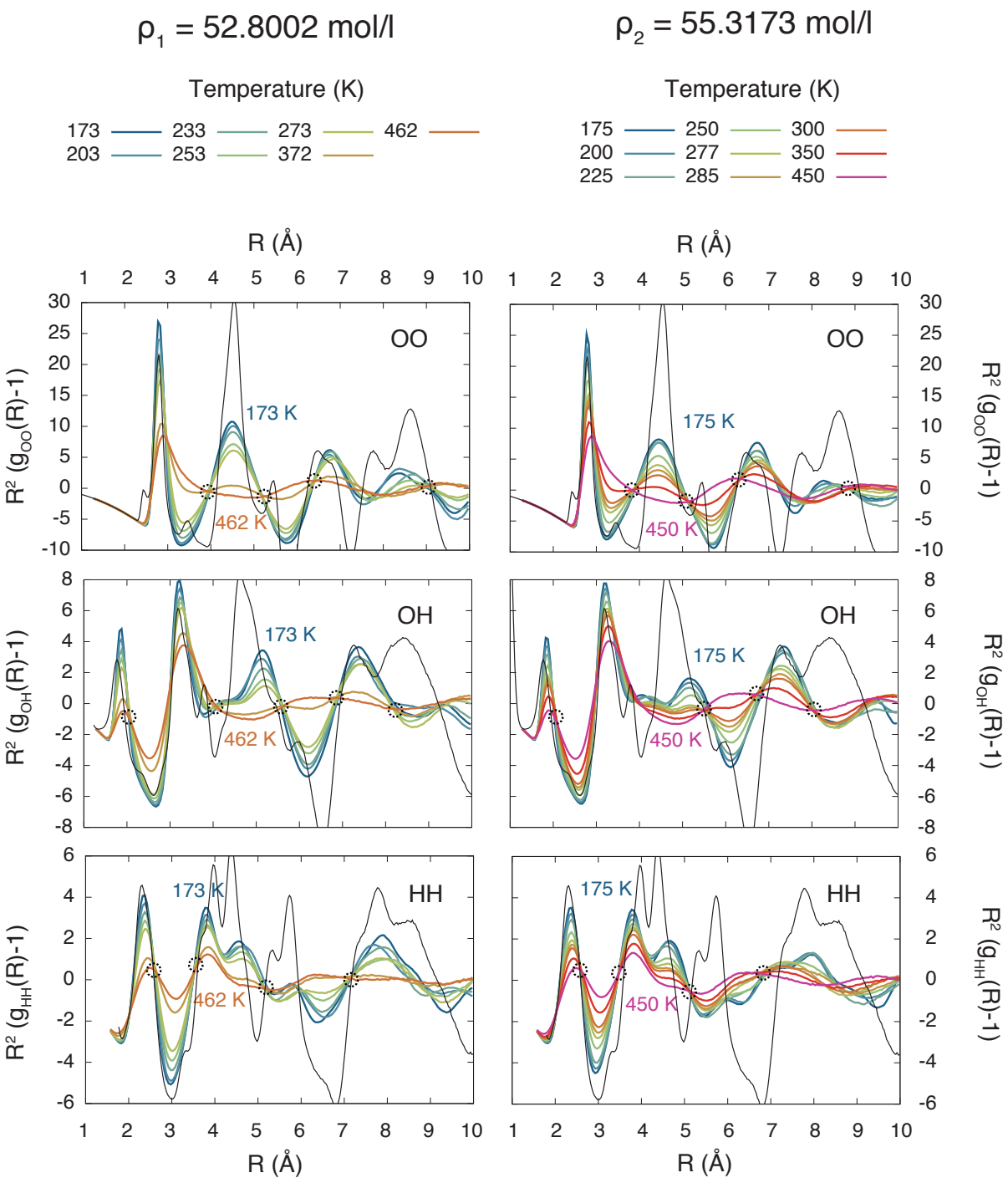

Figure 7.8 *The oxygen-oxygen, oxygen-hydrogen and hydrogen-hydrogen radial distribution functions of QDO-water as a function of temperature at two constant densities: $\rho_1 = 52.8002$ mol/l and $\rho_2 = 55.3173$ mol/l. The black lines denote the corresponding radial distribution functions of ice Ih at 220 K measured by Soper [257]. The dotted circles mark the isosbestic points corresponding to distances where the radial distribution functions remain constant with respect to changes in temperature.*

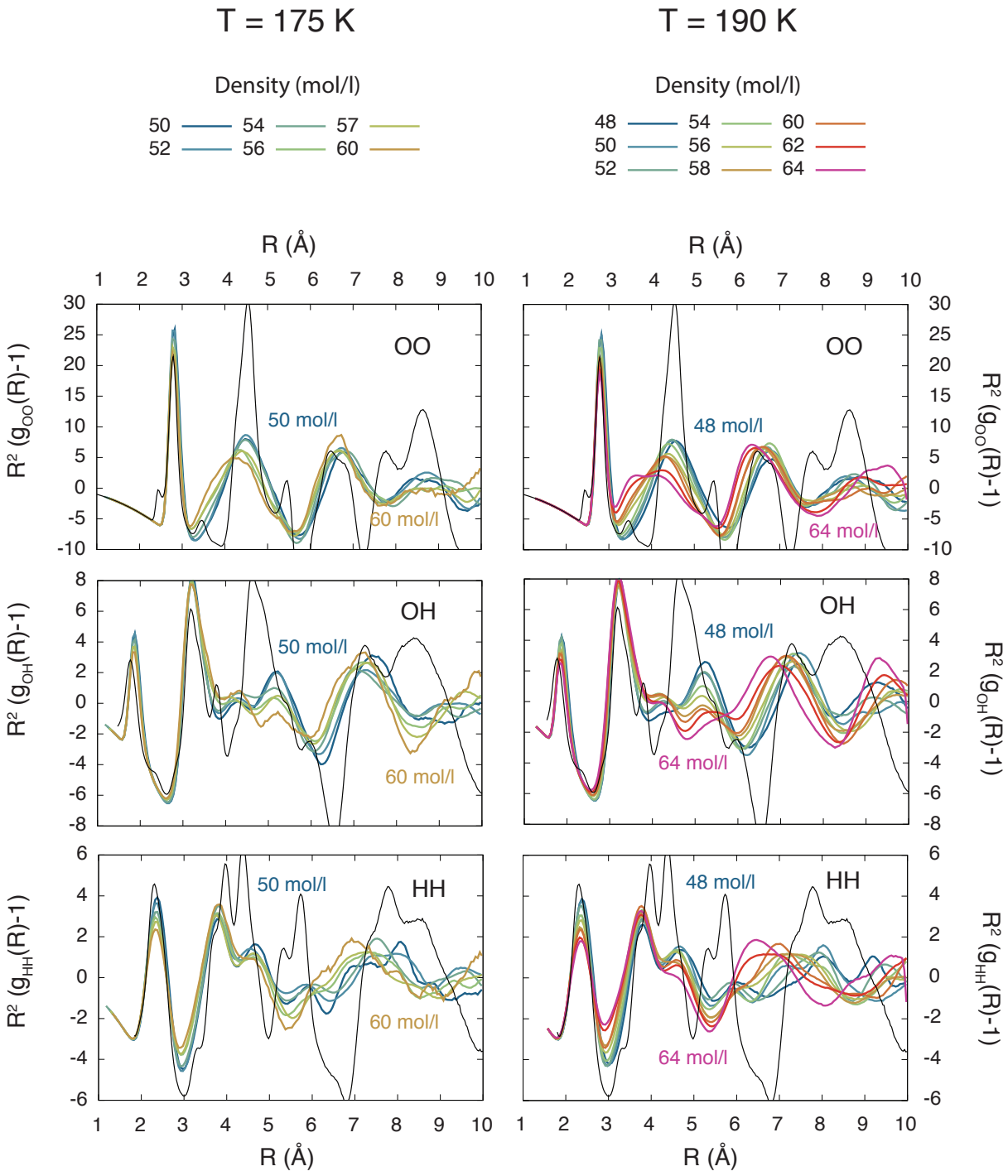

Figure 7.9 *The oxygen-oxygen, oxygen-hydrogen and hydrogen-hydrogen radial distribution functions of QDO water as a function of density at 175 K and 190 K.*

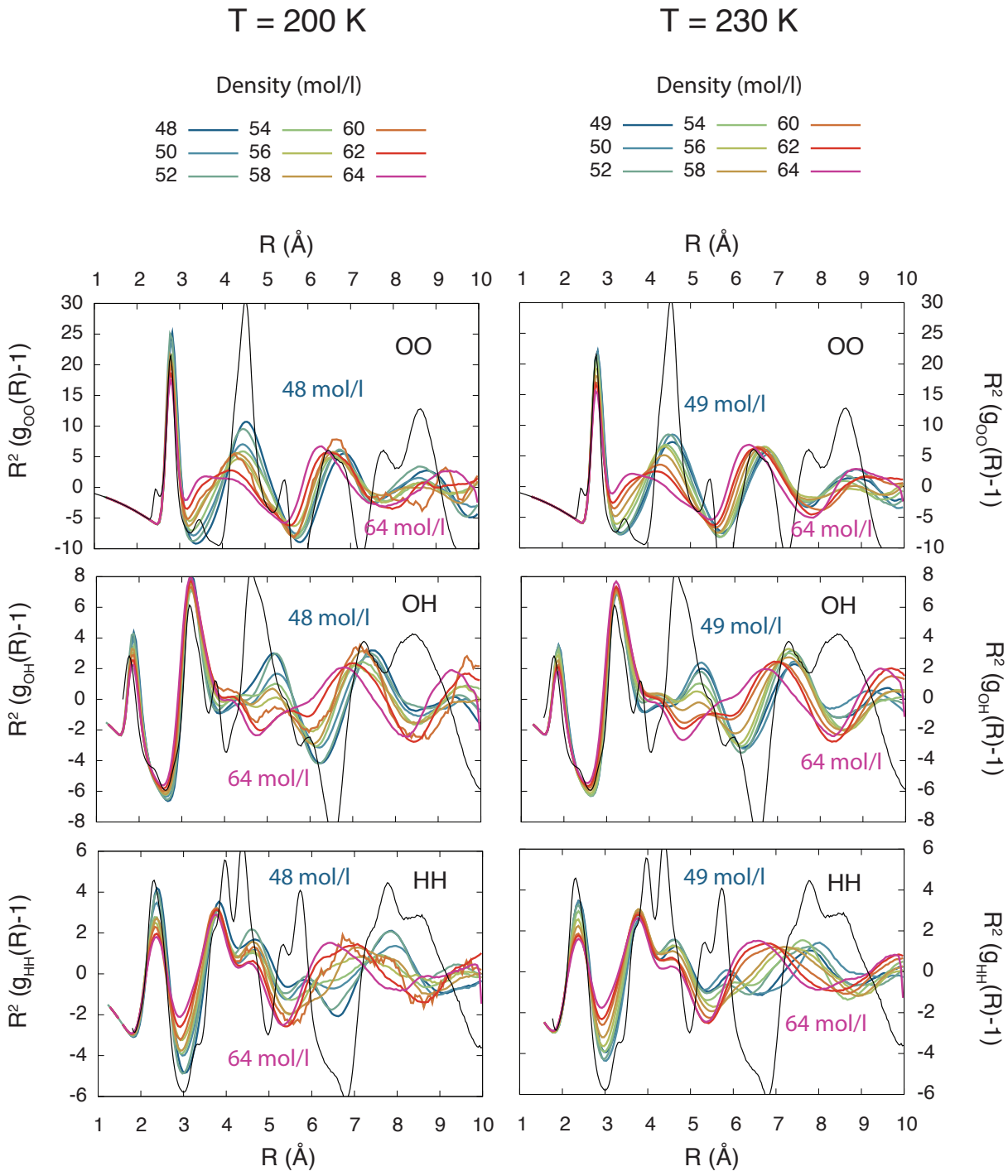

Figure 7.10 *The oxygen-oxygen, oxygen-hydrogen and hydrogen-hydrogen radial distribution functions of QDO water as a function of density at 200 K and 230 K.*

Coordination number

To investigate the local structure in more detail, Figures 7.11 and 7.12 display the oxygen-oxygen coordination numbers at a constant density of $\rho_2 = 55.3173$ mol/l and a constant temperature of 230 K (this being the only isotherm in the region where the dynamics are fast enough to achieve equilibration).

The isochoric coordination number reveals a similar feature as the radial distribution functions: multiple isosbestic points corresponding to the first, second and third coordination shells. However, these isosbestic points occur at different radii. The values of these radii correspond to the first valley in the RDF ($\sim$3.3 Å), the second peak ($\sim$4.5 Å) and the second valley ($\sim$5.8 Å). They essentially correspond to filling of the first shell, a half-filled and a fully filled second shell.

The isothermic coordination number at 230 K displays no points that are independent of density. However, the radial dependence of the coordination number does not change much with density up to a value of 4. This weak dependence on temperature reveals a very interesting feature of supercooled water: *the density of the first shell is largely independent on the overall density.* In other words, up to distances of $\sim$ 3.3 Å, a molecule experiences the same density at 50 mol/l as it does at 60 mol/l. The overall density can then only be tweaked by changes in the second shell, whose peak moves at lower values in the high density liquid and at higher values in the low density liquid, approaching the position of the corresponding ice peak.

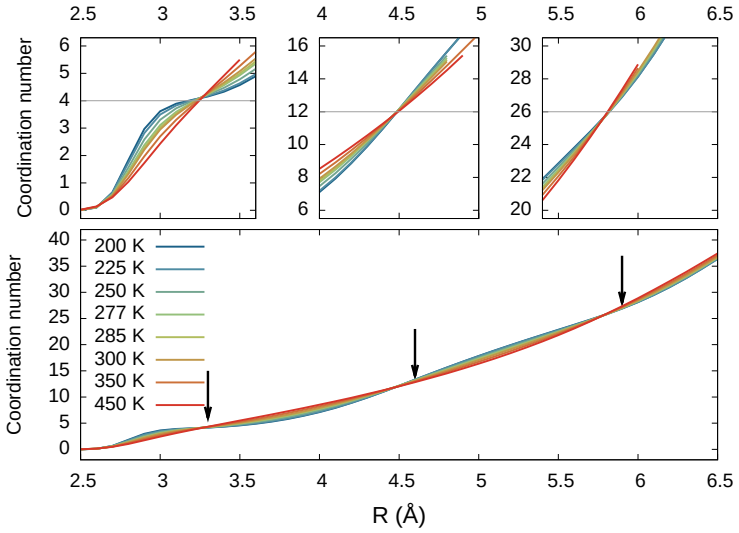

Figure 7.11 *(lower panel) The oxygen-oxygen coordination number as a function of temperature at a constant density of* $\rho_2 = 55.3173$ *mol/l. The coordination number shows three isosbestic distances, i.e. points where the coordination number is independent of temperature. These are indicated by the three arrows. (upper panel) A close-up of the region around the three isosbestic points.*

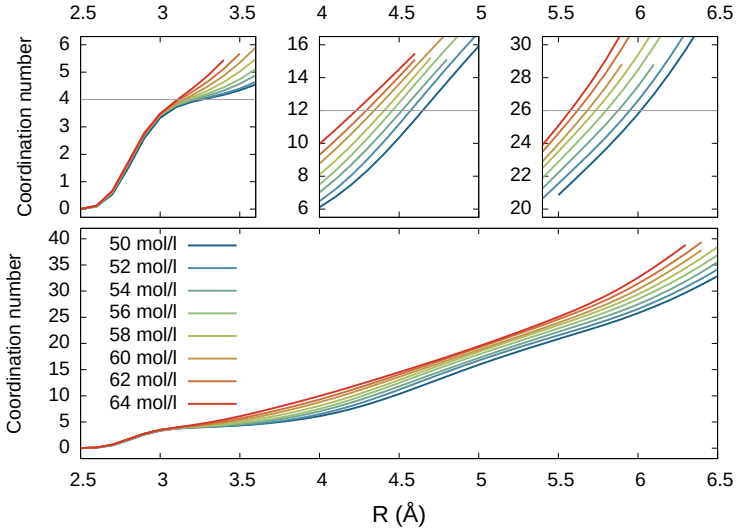

Figure 7.12 *(lower panel) The oxygen-oxygen coordination number as a function of density at a constant temperature of 230 K. Up until a value of 4, the coordination number shows a weak dependence in density, indicating the emergence of a tetrahedral first shell in supercooled water. (upper panel) A close-up of the region around the three isosbestic points that appear at constant density.*

Distribution of nearest neighbour

Another tool for understanding the local structure is the distribution of each neighbour, which is plotted in Figure 7.13. It reveals three regions of distinct behaviour. The first to fourth nearest neighbours move closer upon cooling, which is normal behaviour: the first shell exhibits positive thermal expansion. On the other hand, the fifth to twelfth neighbours *expand* upon cooling – in other words a negative thermal expansion and thus anomalous behaviour. Finally, the thirteenth neighbour revert to normal behaviour, contracting upon cooling.

What's even more interesting is that these boundaries between positive and negative thermal expansion coincide with the first two isosbestic points of the coordination number: 4 and 12.

This situation means that the local structure of liquid water is indeed a mixture of a normal and anomalous component. But the mixture doesn't manifest itself across space, with normal regions and anomalous regions, but across the coordination shell of each molecule: the first coordination shell showing normal behaviour while the second anomalous behaviour.

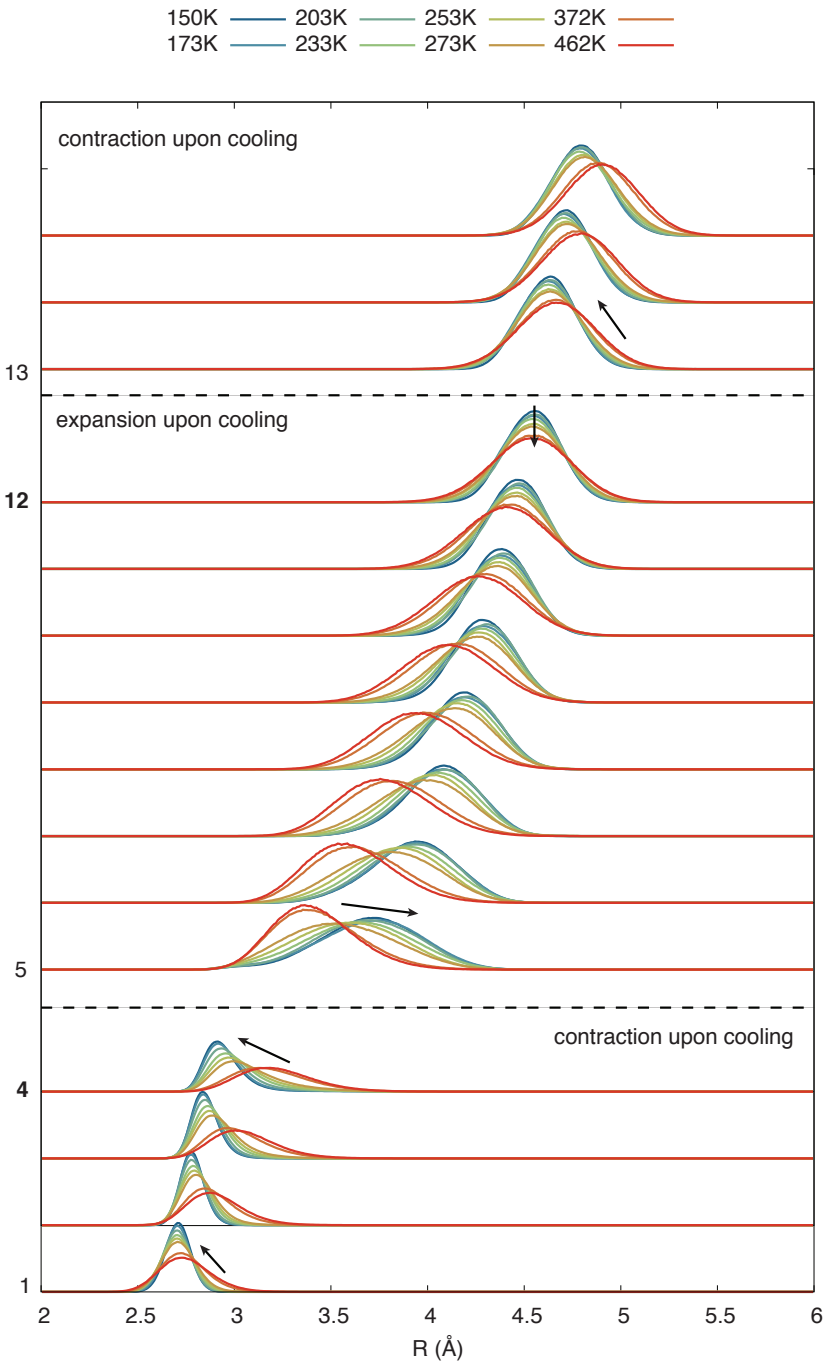

Figure 7.13 *The probability distribution of the i^{th} nearest neighbour with i running from 1 to 10, as a function of temperature at a constant density of $\rho_1 = 52.8002$ mol/l. Th dashed lines separate the regions that contract or expand upon cooling. The arrows indicate the direction of movement of the peaks of the probabilities. The y axis indicates the number of the nearest neighbour, with the probability being measured in arbitrary units.*

7.5 Order parameters

Hydrogen bonding

The previous section looked qualitatively at the structure of supercooled water. On the other hand, this section will consider the structure quantitatively using three different order parameters.

The first is the hydrogen bonding motifs. These are defined in the same way as in Chapter 5. First, the potential of mean force is calculated at each state point. Then, the contour passing through the saddle point at around 3.5 Å and 40° is calculated. A donor bond, connecting a hydrogen atom to a neighbouring oxygen is defined as one where the R_{OO} and θ_{HOO} is inside that contour. An acceptor bond is defined as the opposite side, connecting an oxygen atom to a hydrogen. A hydrogen bonded configuration is denoted by a series of letters such as DDA, representing the number of donor and acceptor bonds.

Figure 7.14 shows the evolution of the number of hydrogen bonds with temperature on the ρ_1 and ρ_2 isochores, showing a number of features. First, the dominance of DDA over DAA is kept at all temperatures studied. This asymmetry gives rise to five hydrogen bonded configurations, DDAAA which appear in both the high and low temperature samples. The probability of configurations with one or two hydrogen bonds become larger than about 1% at temperatures above 250 K, which shows that ambient and low temperature water keeps a well connected network of molecules.

Finally, the probability of three- and four- hydrogen bonded configurations starts to plateau at temperatures close to 220 K. This is again consistent both scenarios where the temperature of 220 K marks a boundary, either between two liquids or between equilibrated and non-equilibrated simulations.

If simulations below 220 K are not equilibrated then the plateau may be an artefact of sampling. At these temperatures, the system would *like* to form more DDAA configurations until the whole system is tetrahedral, and continue expanding upon cooling in the process. However, given that over 90% of the molecules are already DDAA, this will take significant structural reordering, which is hindered by slow dynamics.

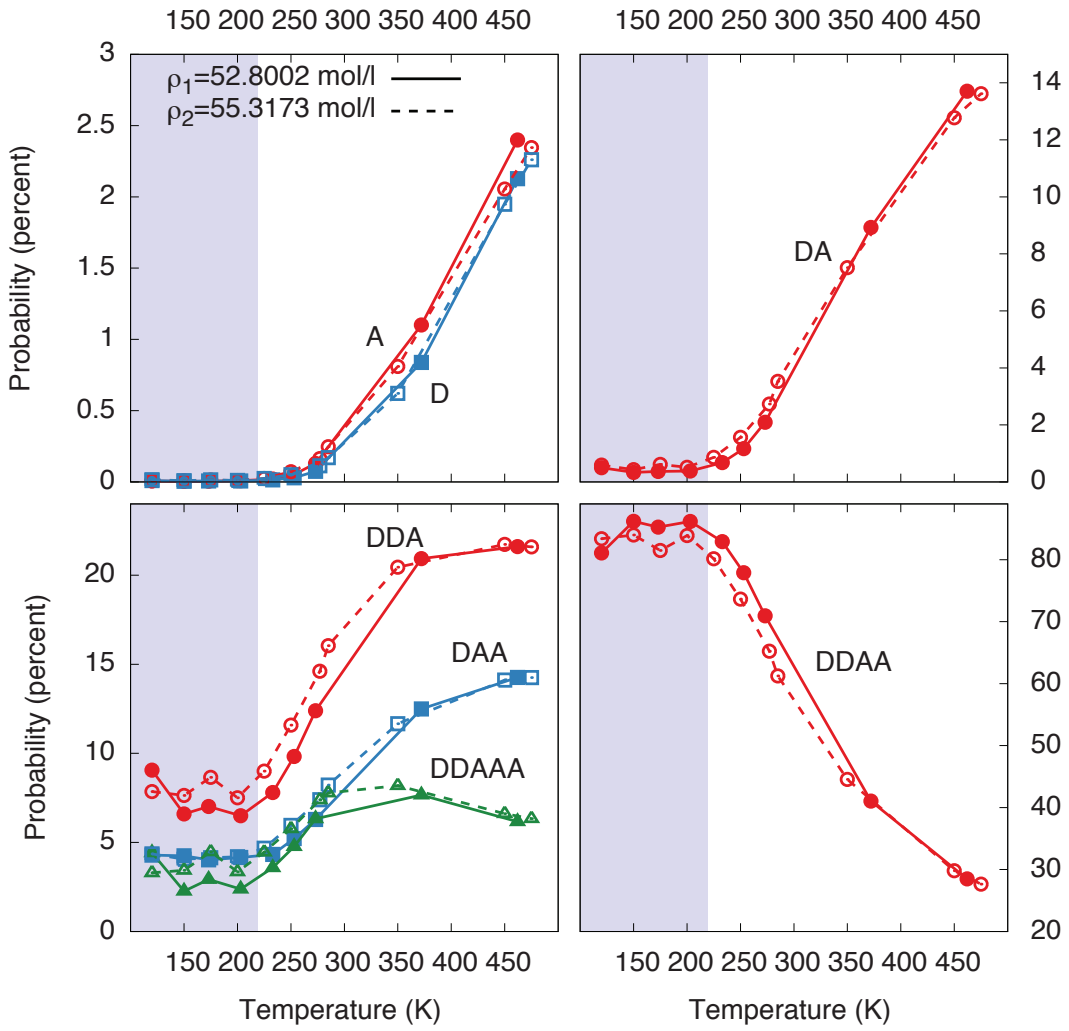

Figure 7.14 *The probability of a given hydrogen bonding motif as a function of temperature from simulations of QDO-water at two constant densities of* $\rho_1 = 52.8002$ *mol/l (continuous lines) and* $\rho_2 = 55.3173$ *mol/l (dashed lines)*

Tetrahedrality

The preference for four hydrogen bonded configurations can be further measured using the tetrahedrality order parameter Q, plotted in Figure 7.15. For a single molecule, this parameter is defined as [75]:

$$q = 1 - \frac{3}{8} \sum_{i=1}^{3} \sum_{j=i+1}^{4} \left(\cos \theta_{ij} + \frac{1}{3} \right)^2 \tag{7.1}$$

The summation is performed over the first four neighbours. The angles θ_{ij} are formed between the line connecting a molecule to its i^{th} and j^{th} neighbours. To calculate Q, the individual order parameters of each molecule are averaged over the whole box and trajectory. A value of 1 means that all molecules are tetrahedrally coordinated. A value of 0 means that the neighbours are arranged randomly.

As expected from the structuring of the first shell upon cooling and supercooling, Q increases with decreasing temperature in a linear fashion, until reaching a value close to 0.8. As with the probability of DDAA, at temperatures below 220 K, Q plateaus. This plateau is consistent with all the structural evidence gathered so far: either the further creation of tetrahedral cages is on timescales longer than the simulation or 220 K marks a phase transition.

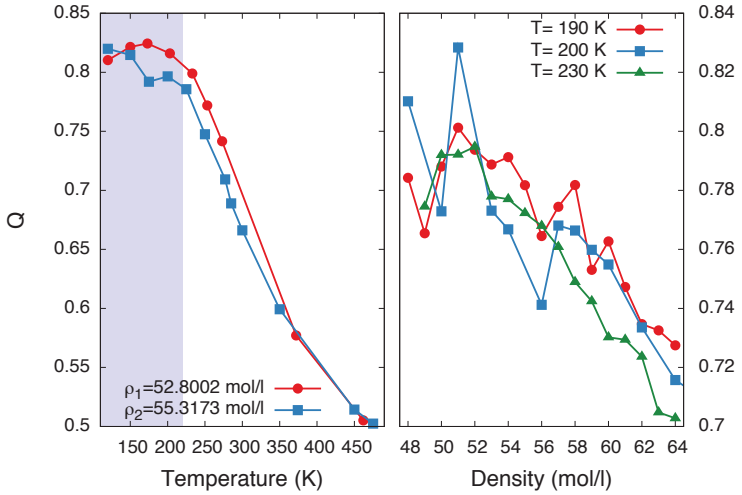

Figure 7.15 *(left) The variation of the tetrahedrality parameter Q as a function of temperature at two constant densities, $\rho_1 = 52.8002$ mol/l and $\rho_1 = 52.8002$ mol/l. (right) The variation of the tetrahedrality parameter Q as a function of density at three constant temperatures, 190 K, 200 K and 230 K.*

Local structure index

The final order parameter considered is the local structure index (LSI), which quantifies the separation between the first and second coordination shells. If that separation is of the order of the spacing between each individual neighbours, the LSI will have a low value. Otherwise, it will have a high values. Mathematically, the LSI is defined as [246]:

$$\mathrm{LSI} = \frac{1}{N}\sum_{i=1}^{N}\left(\Delta_i - \bar{\Delta}\right)^2 . \tag{7.2}$$

The distances between the reference molecule and its i^{th} neighbour are represented by r_i and sorted such that $r_1 < r_2 < ... < r_n < 3.7\text{Å} < r_{n+1}$. The distance between successive neighbours is defined as $\Delta_i = r_{i+1} - r_i$, with $\bar{\Delta}$ being the average of all Δ_i. Note that the last distance to be included in the calculation is r_{i+1}: the distance from the reference molecule to the *first* molecule outside a shell of radius 3.7 Å.

The local structure quantifies the behaviour seen in the probability densities of the nearest neighbours. Upon cooling, the gap between the first and second shell increases, (thus LSI increases). A new effect is the plateauing of the LSI on the ρ_1 isochore at temperatures below 220 K. It is interesting that the LSI does not plateau at ρ_2 and at ρ_1 it plateaus at lower temperatures than the tetrahedrality. If the dynamic scenario is true, this suggests that the second shell order is quicker to equilibrate than the first shell order, which is intuitive: the energy barrier for second shell reordering is smaller than that for first shell reordering.

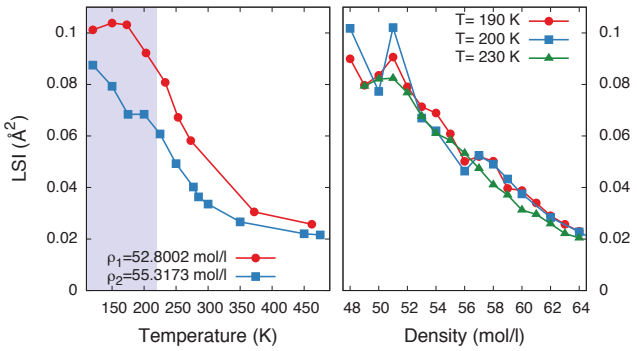

Figure 7.16 *(left) The isochoric variation of the local structure index (LSI) at $\rho_1 = 52.8002$ mol/l and $\rho_1 = 52.8002$ mol/l. (right) The isothermal variation of the local structure index (LSI) at 190 K, 200 K and 230 K.*

7.6 Discussion of the structure of supercooled water

Two questions motivated the study of supercooled water, one macroscopic and one microscopic.

Macroscopically, an major open question in water science whether a a liquid-liquid transition exists in the supercooled liquid. Both simulations and experiment support the idea. The liquid-liquid critical point of two water models (TIP4P/2005 [249] and ST2 [201]) has been calculated by fitting it to an equation of state assuming the existence of such a transition. Similarly for real water: the PVT surface above the homogeneous nucleation temperature and up to pressures of 400 MPa has been fit to estimate a liquid-liquid critical point at pressures of around 50 MPa and temperatures around 220 K [182].

Such a transition is below homogeneous nucleation (235 K at ambient pressure), making experimental confirmation hard. However, experiments evaporatively cooled water down to temperatures of 200 [22] and 227 [243] and saw a continuous rather than abrupt transition in the structure. Limmer and Chandler [159] challenge the existence of a liquid-liquid transition in water, suggesting instead that the liquid cannot be equilibrated before the onset of crystallisation at temperatures where the liquid-liquid transition might exist.

Does QDO-water support the existence of a liquid-liquid phase transition? Certainly the isochores and structural order parameters show a coordinated change in behaviour at 220 K. This can be indicative of a phase transition. The isotherms flatten at temperatures lower than 200 K and at negative pressure, suggesting that the critical point might lie at negative rather than positive pressure.

However, 220 K also marks the onset of slow dynamics (on the timescales of the current simulation times) in real water, meaning relaxation times longer than microseconds. The timescales accessible currently to QDO-water are nanoseconds, so simulations below 220 K can be considered not to have reached equilibrium. Thus, the second explanation is that the change in behaviour is simply an artefact of sampling. The pressures regains normal thermal expansion (i.e. decreasing pressure upon cooling) due to the inability of extra tetrahedral cages to form on the timescales of the simulation. This hypothesis is supported by

the fraction of DDAA molecules and the tetrahedrality order parameter Q, which both flatten at this threshold temperature of 220 K. The tetrahedrality can be forced to take higher values by using umbrella sampling [275]. Indeed, this method was among the ones used to calculate the free energy of ST2 in the tetrahedrality-density plane, showing two free energy minima corresponding to the two liquids [164]. However, biasing the simulation in such a manner can introduce qualitative artefacts, such as the multiple liquid-liquid transitions discovered by Brovchenko et al. [39], which were likely an artefact of his suppression of fluctuation [67, 157].

Microscopically, the structure of QDO water shows substantial changes from high temperature to low temperature. At high temperature, the radial distribution function has a shape similar to a normal liquid. At ambient and supercooled temperatures, the second coordination shell approaches that of ice, showing the tetrahedral nature of both the ambient and supercooled liquid.

These changes occur in such a way that special, isosbestic points remain fixed. In the coordination number, these points mark special values: 4, which is the number of molecules in the first shell and 12, and 26. The nearest neighbour distribution functions reveal what these latter numbers mean. Both a coordination number of 4 and of 12 mark boundaries between regions where the nearest neighbours approach the central molecule or distance away from it.

Structural order parameters increase or decrease linearly upon cooling and supercooling, quantifying similar patterns as observed in the radial distribution functions and the distribution of nearest neighbours. Tetrahedrality increases upon cooling, same for the local structure index and the proportion of DDAA motifs. This shows that, as expected, the local structure of water becomes more tetrahedral upon cooling in a continuous manner. A change in functional behaviour is seen at at 220 K, which can be explained by either the slow dynamics or by crossing a liquid-liquid phase boundary with a critical point at close to zero or negative pressure.

Chapter 8

Conclusion

This thesis has presented the construction and evaluation of an electronically coarse grained model of water. The model, QDO-water, is built by parametrising to the properties of the isolated molecule and a single cut through the dimer energy surface. I showed that the model is transferable to a wide range of environments, from ice II to the liquid–vapour interface of water and supercooled and supercritical water. Namely, it predicts within a few percent of experiment the following quantities, thus displaying an unprecedented degree of transferability:

- Bulk modulus of ice II at 237.65 K
- Lattice constants of ice II between 100 and 160 K
- Liquid–vapour coexistence densities above 300 K
- Temperature of maximum density
- Surface tension
- Radial distribution function in ambient pressure water, supercooled and supercritical water, and at the surface of the liquid
- A positive surface expansion
- Orientation of water molecules at the liquid–vapour interface
- Pressure of supercooled water at 55.3 and 52.8 mol/l above 220 K
- Pressure of supercritical water at 673 K, 773 K and 873 K

Alongside accurate predictions, QDO-water has revealed insights into the physics of water. Namely, it showed that an asymmetry between donor and acceptor molecules is the molecular scale mechanism responsible for the observed surface

orientation of water. A four coordinated molecule prefers to lose an acceptor bond to a donor bond, thus orienting it with the oxygen towards the gas phase.

Furthermore, QDO-water revealed an extra line separating liquid-like from gas-like regions in supercritical water. Typically these were separated by either maxima in thermodynamic responses (the Widom lines) or functional changes in the dynamics (the Frenkel line). This thesis showed that a crossover in the dipole moment can also separate these two regions.

Finally, QDO-water revealed a potential crossover in supercooled water at 220 K and a qualitative difference between the behaviour of the first and second coordination shells of water. The crossover in supercooled water is consistent with either insufficient sampling or a negative pressure liquid–liquid phase transition. The first coordination shell shows a positive thermal expansion while the second shell shows a negative one, thus contributing to the anomalous behaviour of water upon supercooling.

Are all these insights unique to QDO-water? Certainly not – the hydrogen bonding motifs are qualitatively reproduced by TIP4P/2005 while the dipole crossover exists in classically polarisable models, albeit more weakly. However, QDO-water is the only model that combines such accurate predictions across the phase diagram with a wealth of qualitative insights. And this is its major success.

Chapter 9

Future directions

The future development of electronically coarse grained methods can continue in three complementary directions: improved software, new physical systems and methodological developments. Once these three developments are under way, QDOs can be used to explore interesting physical questions such as the role of many body dispersion in condensed matter and what is the minimum set of physics needed to create a transferable water model.

The first step needed is improved software, a task which has partially begun. The software used in this thesis was `qDrude` versions 2 and 3. Version 2 could only simulate water and noble gases, with version 3 being general. However, the lead developer left and version 3 is thus unmaintained. Effort moved towards the integration of QDOs into a fork of the general purpose molecular dynamics code PINY-MD. This however needs a larger engineering effort than is currently available to the project.

Once the new codes are developed, the next step is to study other physical systems. Examples are methane, as an application to a simple organic molecule and peptides, as an application to a biological system.

In parallel, electronic coarse graining needs continued theoretical development. A possible project is the derivation of new estimators for the heat capacity, a quantity that proved a challenge to calculate from the standard energy fluctuation formula. Also, the path integral method of Poltavsky and Tkatchenko [210] can be adapted to simulate QDOs, with the potential of speeding up their simulation speed by an order of magnitude. The enhanced sampling will allow some of the

unanswered questions in this thesis to be answered, such as the behaviour of supercooled water below 220 K.

Alongside the development of improved molecular models, QDOs can be used to answer fundamental questions about condensed matter systems. One interesting such question is the role of many-body dispersion and polarisation in determining the structure and dynamics of materials such as water. This study could be done using QDO-water, by tweaking its parameters to increase the dispersion coefficients uniformly while keeping the polarisabilities intact (as we've done in reference [123]). Then, the C_6 component can be corrected using a C_6/R^6 term to recover the dipole-dipole dispersion of the baseline model. This results in a process that can uniformly increase or decrease the higher order and many-body dispersion terms, allowing us to assess their importance in modelling water.

Another interesting project would be to try to understand the minimal physical system required for a transferable model of water. Is it a QDO or could we do with something simpler? For example, QDO-water used Gaussian charges and dispersion centred on the M site rather than on the oxygen site (the latter is typically used by existing water models). Could these changes improve existing non-polarisable models? Recent experience says they could. For example, Izadi et al. [119] showed that relaxing the geometric constraints of four sites models allowed them to parametrise a fixed charge model that provided an optimum fit to water's phase diagram.

Bibliography

[1] J. L. F. Abascal and C. Vega. A general purpose model for the condensed phases of water: TIP4P/2005. *J. Chem. Phys.*, 123(23):234505, 2005. doi: 10.1063/1.2121687.

[2] J. L. F. Abascal and C. Vega. Widom line and the liquid-liquid critical point for the TIP4P/2005 water model. *J. Chem. Phys.*, 133(23):234502, 2010. doi: 10.1063/1.3506860.

[3] J. L. F. Abascal, E. Sanz, R. Garciá Fernández, and C. Vega. A potential model for the study of ices and amorphous water: TIP4P/Ice. *J. Chem. Phys.*, 122(23):234511, 2005. doi: 10.1063/1.1931662.

[4] Peter Ahlström, Anders Wallqvist, Sven Engström, and Bo Jönsson. A molecular dynamics study of polarizable water. *Mol. Phys.*, 68(3):563–581, 1989. doi: 10.1080/00268978900102361.

[5] Omololu Akin-Ojo, Yang Song, and Feng Wang. Developing ab initio quality force fields from condensed phase quantum-mechanics/molecular-mechanics calculations through the adaptive force matching method. *J. Chem. Phys.*, 129(6):064108, 2008. doi: 10.1063/1.2965882.

[6] Naoko Akiya and Phillip E. Savage. Roles of water for chemical reactions in high-temperature water. *Chem. Rev.*, 102(8):2725–2750, 2002. doi: 10.1021/cr000668w.

[7] G. Albiser, A. Lamiri, and S. Premilat. The A–B transition: temperature and base composition effects on hydration of DNA. *Int. J. Biol. Macromol.*, 28(3):199–203, 2001. doi: 10.1016/s0141-8130(00)00160-4.

[8] D. Alfè, A. P. Bartók, G. Csányi, and M. J. Gillan. Communication: Energy benchmarking with quantum Monte Carlo for water nano-droplets and bulk liquid water. *J. Chem. Phys.*, 138(22):221102, 2013. doi: 10.1063/1.4810882.

[9] M. P. Allen and D. J. Tildesley. *Computer Simulation of Liquids (Oxford Science Publications)*. Clarendon Press, 1989. ISBN 0198556454.

[10] Katrin Amann-Winkel, Marie-Claire Bellissent-Funel, Livia E. Bove, Thomas Loerting, Anders Nilsson, Alessandro Paciaroni, Daniel Schlesinger, and Lawrie Skinner. X-ray and neutron scattering of water. *Chem. Rev.*, 116(13):7570–7589, 2016. doi: 10.1021/acs.chemrev.5b00663.

[11] Katrin Amann-Winkel, Roland Böhmer, Franz Fujara, Catalin Gainaru, Burkhard Geil, and Thomas Loerting. Colloquium : Water's controversial glass transitions. *Rev. Mod. Phys.*, 88(1):011002, 2016. doi: 10.1103/RevModPhys.88.011002.

[12] Francesco Ambrosio, Giacomo Miceli, and Alfredo Pasquarello. Structural, dynamical, and electronic properties of liquid water: A hybrid functional study. *J. Phys. Chem. B*, 120(30):7456–7470, 2016. doi: 10.1021/acs.jpcb.6b03876.

[13] C. A. Angell. Supercooled Water. *Annu. Rev. Phys. Chem.*, 34(1):593–630, 1983. doi: 10.1146/annurev.pc.34.100183.003113.

[14] B. M. Auer and J. L. Skinner. Vibrational sum-frequency spectroscopy of the liquid/vapor interface for dilute HOD in D_2O. *J. Chem. Phys.*, 129(21):214705, 2008. doi: 10.1063/1.3012568.

[15] Laurent Augustin, Carlo Barbante, Piers R. F. Barnes, Jean Marc Barnola, Matthias Bigler, Emiliano Castellano, Olivier Cattani, Jerome Chappellaz, Dorthe Dahl-Jensen, Barbara Delmonte, Gabrielle Dreyfus, Gael Durand, Sonia Falourd, Hubertus Fischer, Jacqueline Flückiger, Margareta E. Hansson, Philippe Huybrechts, Gérard Jugie, Sigfus J. Johnsen, Jean Jouzel, Patrik Kaufmann, Josef Kipfstuhl, Fabrice Lambert, Vladimir Y. Lipenkov, Geneviève C. Littot, Antonio Longinelli, Reginald Lorrain, Valter Maggi, Valerie Masson-Delmotte, Heinz Miller, Robert Mulvaney, Johannes Oerlemans, Hans Oerter, Giuseppe Orombelli, Frederic Parrenin, David A. Peel, Jean-Robert Petit, Dominique Raynaud, Catherine Ritz, Urs Ruth, Jakob Schwander, Urs Siegenthaler, Roland Souchez, Bernhard Stauffer, Jorgen Peder Steffensen, Barbara Stenni, Thomas F. Stocker, Ignazio E. Tabacco, Roberto Udisti, Roderik S. W. van de Wal, Michiel van den Broeke, Jerome Weiss, Frank Wilhelms, Jan-Gunnar Winther, Eric W. Wolff, and Mario Zucchelli. Eight glacial cycles from an antarctic ice core. *Nature*, 429(6992):623–628, 2004. doi: 10.1038/nature02599.

[16] B. M. Axilrod and E. Teller. Interaction of the van der Waals type between three atoms. *J. Chem. Phys.*, 11(6):299–300, 1943. doi: 10.1063/1.1723844.

[17] Mouna El Mekki Azouzi, Claire Ramboz, Jean-François Lenain, and Frédéric Caupin. A coherent picture of water at extreme negative pressure. *Nat. Phys.*, 9(1):38–41, 2012. doi: 10.1038/nphys2475.

[18] Stephan J. Bachmann and Wilfred F. van Gunsteren. An improved simple polarisable water model for use in biomolecular simulation. *J. Chem. Phys.*, 141(22):22D515, 2014. doi: 10.1063/1.4897976.

[19] Y. S. Badyal, M.-L. Saboungi, D. L. Price, S. D. Shastri, D. R. Haeffner, and A. K. Soper. Electron distribution in water. *J. Chem. Phys.*, 112(21): 9206, 2000. doi: 10.1063/1.481541.

[20] J. Barber. Photosystem II: The water-splitting enzyme of photosynthesis. *Cold Spring Harbor Symp. Quant. Biol.*, 77(0):295–307, 2012. doi: 10.1101/sqb.2012.77.014472.

[21] J. A. Barker and R. O. Watts. Structure of water; a Monte Carlo calculation. *Chem. Phys. Lett.*, 3(3):144–145, 1969. doi: 10.1016/0009-2614(69)80119-3.

[22] Lawrence S. Bartell and Jinfan Huang. Supercooling of water below the anomalous range near 226 K. *J. Phys. Chem.*, 98(31):7455–7457, 1994. doi: 10.1021/j100082a011.

[23] Thorsten Bartels-Rausch, Vance Bergeron, Julyan H. E. Cartwright, Rafael Escribano, John L. Finney, Hinrich Grothe, Pedro J. Gutiérrez, Jari Haapala, Werner F. Kuhs, Jan B. C. Pettersson, Stephen D. Price, C. Ignacio Sainz-Díaz, Debbie J. Stokes, Giovanni Strazzulla, Erik S. Thomson, Hauke Trinks, and Nevin Uras-Aytemiz. Ice structures, patterns, and processes: A view across the icefields. *Rev. Mod. Phys.*, 84(2):885–944, 2012. doi: 10.1103/revmodphys.84.885.

[24] Elizabeth A. Bell, Patrick Boehnke, T. Mark Harrison, and Wendy L. Mao. Potentially biogenic carbon preserved in a 4.1 billion-year-old zircon. *Proc. Natl. Acad. Sci. U.S.A.*, 112(47):14518–14521, 2015. doi: 10.1073/pnas.1517557112.

[25] Marie-Claire Bellissent-Funel, Ali Hassanali, Martina Havenith, Richard Henchman, Peter Pohl, Fabio Sterpone, David van der Spoel, Yao Xu, and Angel E. Garcia. Water determines the structure and dynamics of proteins. *Chem. Rev.*, 116(13):7673–7697, 2016. doi: 10.1021/acs.chemrev.5b00664.

[26] A. Ben-Naim. Statistical mechanics of water-like particles in two-dimensions. *Mol. Phys.*, 24(4):705–721, 1972. doi: 10.1080/00268977200101851.

[27] Tobias Benighaus, Robert A. DiStasio, Rohini C. Lochan, Jeng-Da Chai, and Martin Head-Gordon. Semiempirical double-hybrid density functional with improved description of long-range correlation. *J. Phys. Chem. A*, 112 (12):2702–2712, 2008. doi: 10.1021/jp710439w.

[28] H. J. C. Berendsen, J. R. Grigera, and T. P. Straatsma. The missing term in effective pair potentials. *J. Phys. Chem.*, 91(24):6269–6271, 1987. doi: 10.1021/j100308a038.

[29] Herman J. C. Berendsen, James P. M. Postma, Wilfred F. van Gunsteren, and Jan Hermans. Interaction models for water in relation to protein

hydration. In *Intermolecular forces*, pages 331–342. Springer, 1981. doi: 10.1007/978-94-015-7658-1_21.

[30] J. D. Bernal and R. H. Fowler. A theory of water and ionic solution, with particular reference to hydrogen and hydroxyl ions. *J. Chem. Phys.*, 1(8): 515, 1933. doi: 10.1063/1.1749327.

[31] Daniel Berthelot. Sur le mélange des gaz. *Compt. Rendus.*, 126:1703–1706, 1898.

[32] Theodore Bibby, Jaakko Putkonen, Daniel Morgan, Greg Balco, and David L. Shuster. Million year old ice found under meter thick debris layer in Antarctica. *Geophys. Res. Lett.*, 43(13):6995–7001, 2016. doi: 10.1002/2016gl069889.

[33] Francis Birch. Finite elastic strain of cubic crystals. *Phys. Rev.*, 71(11): 809–824, 1947. doi: 10.1103/physrev.71.809.

[34] Joseph Black. The supposed effect of boiling upon water, in disposing it to freeze more readily, ascertained by experiments. By Joseph Black, M. D. Professor of Chemistry at Edinburgh, in a letter to Sir John Pringle, Bart. P. R. S. *Philos. Trans. Roy. Soc. London*, 65:124–128, 1775. doi: 10.1098/rstl.1775.0014.

[35] L. E. Bove, S. Klotz, J. Philippe, and A. M. Saitta. Pressure-induced polyamorphism in salty water. *Phys. Rev. Lett.*, 106(12):125701, 2011. doi: 10.1103/PhysRevLett.106.125701.

[36] V. V. Brazhkin, Yu. D. Fomin, A. G. Lyapin, V. N. Ryzhov, and K. Trachenko. Two liquid states of matter: A dynamic line on a phase diagram. *Phys. Rev. E*, 85(3), 2012. doi: 10.1103/physreve.85.031203.

[37] P. W. Bridgman. Water, in the liquid and five solid forms, under pressure. *Proc. Am. Acad. Arts Sci.*, 47(13):441, 1912. doi: 10.2307/20022754.

[38] John Brodholt, Marco Sampoli, and Renzo Vallauri. Parameterizing a polarizable intermolecular potential for water. *Mol. Phys.*, 86(1):149–158, 1995. doi: 10.1080/00268979500101901.

[39] Ivan Brovchenko, Alfons Geiger, and Alla Oleinikova. Multiple liquid–liquid transitions in supercooled water. *The Journal of Chemical Physics*, 118(21): 9473, 2003. doi: 10.1063/1.1576372.

[40] V. Buch, R. Martoňák, and M. Parrinello. Data bank on ice and icy particles. `https://web.archive.org/web/20140821113851/http://www.fh.huji.ac.il/~viki/databank/OtherIcePolymorphs2.html`. Accessed 21 August 2014.

[41] V. Buch, R. Martoňák, and M. Parrinello. A new molecular-dynamics based approach for molecular crystal structure search. *J. Chem. Phys.*, 123(5): 051108, 2005. doi: 10.1063/1.2000230.

[42] C. Cagniard de la Tour. Exposé de quelques résultats obtenu par l'action combinée de la chaleur et de la compression sur certains liquides, tels que l'eau, l'alcool, l'éther sulfurique et l'essence de pétrole rectifiée. *Ann. Chim. Phys.*, 21:127–132, 1822.

[43] Christopher D. Cappa, Jared D. Smith, Kevin R. Wilson, and Richard J. Saykally. Revisiting the total ion yield x-ray absorption spectra of liquid water microjets. *J. Phys.: Condens. Matter*, 20(20):205105, 2008. doi: 10.1088/0953-8984/20/20/205105.

[44] Frédéric Caupin. Escaping the no man's land: Recent experiments on metastable liquid water. *J. Non-Cryst. Solids*, 407:441–448, 2015.

[45] Frédéric Caupin and Eric Herbert. Cavitation in water: a review. *C. R. Phys.*, 7(9-10):1000–1017, 2006.

[46] Frédéric Caupin, Arnaud Arvengas, Kristina Davitt, Mouna El Mekki Azouzi, Kirill I. Shmulovich, Claire Ramboz, David A. Sessoms, and Abraham D. Stroock. Exploring water and other liquids at negative pressure. *J. Phys.: Condens. Matter*, 24(28):284110, 2012.

[47] Aviel Chaimovich and M. Scott Shell. Anomalous waterlike behavior in spherically-symmetric water models optimized with the relative entropy. *Phys. Chem. Chem. Phys.*, 11(12):1901, 2009. doi: 10.1039/b818512c.

[48] D. Chandler. Metastability and no criticality. *Nature*, 531(7593):E1–E2, 2016. doi: 10.1038/nature16539.

[49] Bin Chen, Jianhua Xing, and J. Ilja Siepmann. Development of polarizable water force fields for phase equilibrium calculations. *J. Phys. Chem. B*, 104 (10):2391–2401, 2000. doi: 10.1021/jp993687m.

[50] Yeonchoo Cho, Seung Kyu Min, Jeonghun Yun, Woo Youn Kim, Alexandre Tkatchenko, and Kwang S. Kim. Noncovalent interactions of DNA bases with naphthalene and graphene. *J. Chem. Theory Comput.*, 9(4):2090–2096, 2013. doi: 10.1021/ct301097u.

[51] G. Chopra and M. Levitt. Remarkable patterns of surface water ordering around polarized buckminsterfullerene. *Proc. Natl. Acad. Sci. U.S.A.*, 108 (35):14455–14460, 2011. doi: 10.1073/pnas.1110626108.

[52] Flaviu S. Cipcigan, Vlad P. Sokhan, Andrew P. Jones, Jason Crain, and Glenn J. Martyna. Hydrogen bonding and molecular orientation at the liquid–vapour interface of water. *Phys. Chem. Chem. Phys.*, 17(14):8660–8669, 2015. doi: 10.1039/c4cp05506c.

[53] Flaviu S. Cipcigan, Vlad P. Sokhan, Jason Crain, and Glenn J. Martyna. Electronic coarse graining enhances the predictive power of molecular simulation allowing challenges in water physics to be addressed. *J. Comput. Phys.*, 326:222–233, 2016. doi: 10.1016/j.jcp.2016.08.030.

[54] Flaviu S. Cipcigan, Vlad P. Sokhan, Jason Crain, and Glenn J. Martyna. Structural order and hydrogen bonding at the limits of liquid water stability. in prep.

[55] Gerardo Andrés Cisneros, Kjartan Thor Wikfeldt, Lars Ojamäe, Jibao Lu, Yao Xu, Hedieh Torabifard, Albert P. Bartók, Gábor Csányi, Valeria Molinero, and Francesco Paesani. Modeling molecular interactions in water: From pairwise to many-body potential energy functions. *Chem. Rev.*, 116 (13):7501–7528, 2016. doi: 10.1021/acs.chemrev.5b00644.

[56] W. Cochran. Lattice dynamics of alkali halides. *Philos. Mag.*, 4(45):1082–1086, 1959. doi: 10.1080/14786435908238288.

[57] Olivier Collet. How does the first water shell fold proteins so fast? *J. Chem. Phys.*, 134(8):085107, 2011. doi: 10.1063/1.3554731.

[58] M. M. Conde, C. Vega, G. A. Tribello, and B. Slater. The phase diagram of water at negative pressures: Virtual ices. *J. Chem. Phys.*, 131(3):034510, 2009. doi: 10.1063/1.3182727.

[59] C. A. Coulson and D. Eisenberg. Interactions of H_2O molecules in ice. I. the dipole moment of an H_2O molecule in ice. *Proc. R. Soc. London, Ser. A*, 291(1427):445–453, 1966. doi: 10.1098/rspa.1966.0105.

[60] N. Cox, D. A. Pantazis, F. Neese, and W. Lubitz. Artificial photosynthesis: understanding water splitting in nature. *Interface Focus*, 5(3):20150009–20150009, 2015. doi: 10.1098/rsfs.2015.0009.

[61] Antonio Cupane, Margarita Fomina, Irina Piazza, Judith Peters, and Giorgio Schirò. Experimental evidence for a liquid-liquid crossover in deeply cooled confined water. *Phys. Rev. Lett.*, 113(21):1–5, 2014. doi: 10.1103/PhysRevLett.113.215701.

[62] G. B. Dalrymple. The age of the earth in the twentieth century: a problem (mostly) solved. *Geol. Soc. London Spec. Publ.*, 190(1):205–221, 2001. doi: 10.1144/gsl.sp.2001.190.01.14.

[63] Liem X. Dang and Tsun-Mei Chang. Molecular dynamics study of water clusters, liquid, and liquid–vapor interface of water with many-body potentials. *J. Chem. Phys.*, 106(19):8149, 1997. doi: 10.1063/1.473820.

[64] Liem X. Dang and Tsun-Mei Chang. Molecular mechanism of ion binding to the liquid/vapor interface of water. *J. Phys. Chem. B*, 106(2):235–238, 2002. doi: 10.1021/jp011853w.

[65] Tom Darden, Darrin York, and Lee Pedersen. Particle mesh Ewald: An Nlog(N) method for Ewald sums in large systems. *J. Chem. Phys.*, 98(12): 10089–10092, 1993. doi: 10.1063/1.464397.

[66] Kristina Davitt, Etienne Rolley, Frédéric Caupin, Arnaud Arvengas, and Sébastien Balibar. Equation of state of water under negative pressure. *J. Chem. Phys.*, 133(17):174507, 2010.

[67] Pablo G. Debenedetti. Supercooled and glassy water. *J. Phys.: Condens. Matter*, 15(45):R1669–R1726, 2003.

[68] Z. H. Deng, G. J. Martyna, and M. L. Klein. Quantum Simulation Studies of Metal-Ammonia Solutions. *J. Chem. Phys.*, 100(10):7590–7601, 1994. doi: 10.1063/1.466852.

[69] Cristiano L. Dias, Tapio Ala-Nissila, Martin Grant, and Mikko Karttunen. Three-dimensional "Mercedes-Benz" model for water. *J. Chem. Phys.*, 131 (5):054505, 2009. doi: 10.1063/1.3183935.

[70] Paul Drude. *The theory of optics*. Longmans, Green & Co., 1902.

[71] Q. Du, R. Superfine, E. Freysz, and Y. Shen. Vibrational spectroscopy of water at the vapor/water interface. *Phys. Rev. Lett.*, 70(15):2313–2316, 1993. doi: 10.1103/physrevlett.70.2313.

[72] G. G. Dvoryankina, V. F. Dvoryankin, and A. G. Petrov. Calculation of the atomic scattering factors of fast electrons at zero angle of incidence of an electron beam and mean inner crystal potentials. *Crystallogr. Rep.*, 53 (2):187–191, 2008. doi: 10.1134/s1063774508020041.

[73] D. Ehre, E. Lavert, M. Lahav, and I. Lubomirsky. Water freezes differently on positively and negatively charged surfaces of pyroelectric materials. *Science*, 327(5966):672–675, 2010.

[74] Werner U. Ehrmann and Andreas Mackensen. Sedimentological evidence for the formation of an East Antarctic ice sheet in Eocene/Oligocene time. *Palaeogeography, Palaeoclimatology, Palaeoecology*, 93(1-2):85–112, 1992. doi: 10.1016/0031-0182(92)90185-8.

[75] Jeffrey R. Errington and Pablo G. Debenedetti. Relationship between structural order and the anomalies of liquid water. *Nature*, 409(6818): 318–321, 2001. doi: 10.1038/35053024.

[76] Andrzej Falenty, Thomas C. Hansen, and Werner F. Kuhs. Formation and properties of ice XVI obtained by emptying a type sII clathrate hydrate. *Nature*, 516(7530):231–233, 2014. doi: 10.1038/nature14014.

[77] George S. Fanourgakis and Sotiris S. Xantheas. Development of transferable interaction potentials for water. v. extension of the flexible, polarizable, thole-type model potential (TTM3-F, v. 3.0) to describe the vibrational spectra of water clusters and liquid water. *J. Chem. Phys.*, 128(7):074506, 2008. doi: 10.1063/1.2837299.

[78] John R. Farrell and Peter McTigue. Precise compensating potential difference measurements with a voltaic cell. *J. Electroanal. Chem. Interfacial Electrochem.*, 139(1):37–56, 1982. doi: 10.1016/0022-0728(82)85102-4.

[79] W. Ronald Fawcett. The ionic work function and its role in estimating absolute electrode potentials. *Langmuir*, 24(17):9868–9875, 2008. doi: 10.1021/la7038976.

[80] Richard P. Feynman. *Statistical Mechanics: A Set Of Lectures (Advanced Books Classics)*. Westview Press, 1998. ISBN 0201360764.

[81] H. Fischer, J. Severinghaus, E. Brook, E. Wolff, M. Albert, O. Alemany, R. Arthern, C. Bentley, D. Blankenship, J. Chappellaz, T. Creyts, D. Dahl-Jensen, M. Dinn, M. Frezzotti, S. Fujita, H. Gallee, R. Hindmarsh, D. Hudspeth, G. Jugie, K. Kawamura, V. Lipenkov, H. Miller, R. Mulvaney, F. Parrenin, F. Pattyn, C. Ritz, J. Schwander, D. Steinhage, T. van Ommen, and F. Wilhelms. Where to find 1.5 million yr old ice for the IPICS "oldest-ice" ice core. *Clim. Past*, 9(6):2489–2505, 2013. doi: 10.5194/cp-9-2489-2013.

[82] Michael E. Fisher. Decay of correlations in linear systems. *J. Chem. Phys.*, 50(9):3756, 1969. doi: 10.1063/1.1671624.

[83] Yu. D. Fomin, V. N. Ryzhov, E. N. Tsiok, and V. V. Brazhkin. Dynamical crossover line in supercritical water. *Sci. Rep.*, 5:14234, 2015. doi: 10.1038/srep14234.

[84] Peter R. Fontana. Theory of long-range interatomic forces. I. Dispersion energies between unexcited atoms. *Phys. Rev.*, 123(5):1865–1870, 1961. doi: 10.1103/physrev.123.1865.

[85] A. D. Fortes, I. G. Wood, J. P. Brodholt, and L. Vocădlo. Ab initio simulation of the ice II structure. *J. Chem. Phys.*, 119(8):4567, 2003. doi: 10.1063/1.1593630.

[86] A. D. Fortes, I. G. Wood, M. Alfredsson, L. Vočadlo, and K. S. Knight. The incompressibility and thermal expansivity of D_2O ice II determined by powder neutron diffraction. *J. Appl. Crystallogr.*, 38(4):612–618, 2005. doi: 10.1107/s0021889805014226.

[87] Raúl Fuentes-Azcatl and José Alejandre. Non-polarizable force field of water based on the dielectric constant: TIP4P/ϵ. *J. Phys. Chem. B*, 118(5):1263–1272, 2014. doi: 10.1021/jp410865y.

[88] Raúl Fuentes-Azcatl, Noé Mendoza, and José Alejandre. Improved SPC force field of water based on the dielectric constant: SPC/ϵ. *Physica A*, 420:116–123, 2015. doi: 10.1016/j.physa.2014.10.072.

[89] V. Fuentes-Landete, C. Mitterdorfer, P. H. Handle, G. N. Ruiz, J. Bernard, A. Bogdan, M. Seidl, K. Amann-Winkel, J. Stern, S. Fuhrmann, and T. Loerting. Crystalline and amorphous ices. In *Proceedings of the International School of Physics "Enrico Fermi". Water: Fundamentals as the Basis for Understanding the Environment and Promoting Technology.*, pages 173–208. IOS Press, 2015. doi: 10.3254/978-1-61499-507-4-173.

[90] R. E. Gagnon, H. Kiefte, M. J. Clouter, and Edward Whalley. Pressure dependence of the elastic constants of ice Ih to 2.8 kbar by Brillouin spectroscopy. *J. Chem. Phys.*, 89(8):4522, 1988. doi: 10.1063/1.454792.

[91] R. E. Gagnon, H. Kiefte, M. J. Clouter, and Edward Whalley. Acoustic velocities and densities of polycrystalline ice Ih, II, III, v, and VI by Brillouin spectroscopy. *J. Chem. Phys.*, 92(3):1909, 1990. doi: 10.1063/1.458021.

[92] Alex P. Gaiduk, François Gygi, and Giulia Galli. Density and compressibility of liquid water and ice from first-principles simulations with hybrid functionals. *J. Phys. Chem. Lett.*, 6(15):2902–2908, 2015. doi: 10.1021/acs.jpclett.5b00901.

[93] M. J. Gillan, F. R. Manby, M. D. Towler, and D. Alfè. Assessing the accuracy of quantum Monte Carlo and density functional theory for energetics of small water clusters. *J. Chem. Phys.*, 136(24):244105, 2012. doi: 10.1063/1.4730035.

[94] M. J. Gillan, D. Alfè, A. P. Bartók, and G. Csányi. First-principles energetics of water clusters and ice: A many-body analysis. *J. Chem. Phys.*, 139(24):244504, 2013. doi: 10.1063/1.4852182.

[95] Michael J. Gillan, Dario Alfè, and Angelos Michaelides. Perspective: How good is DFT for water? *J. Chem. Phys.*, 144(13):130901, 2016. doi: 10.1063/1.4944633.

[96] Mark S. Gordon, Dmitri G. Fedorov, Spencer R. Pruitt, and Lyudmila V. Slipchenko. Fragmentation methods: A route to accurate calculations on large systems. *Chem. Rev.*, 112(1):632–672, 2012. doi: 10.1021/cr200093j.

[97] L. Greengard and V. Rokhlin. A fast algorithm for particle simulations. *J. Comput. Phys.*, 73(2):325–348, 1987. doi: 10.1016/0021-9991(87)90140-9.

[98] Bertrand Guillot. A reappraisal of what we have learnt during three decades of computer simulations on water. *J. Mol. Liq.*, 101(1-3):219–260, 2002. doi: 10.1016/s0167-7322(02)00094-6.

[99] Stephen Harrington, Rong Zhang, Peter H. Poole, Francesco Sciortino, and H. Eugene Stanley. Liquid-liquid phase transition: Evidence from simulations. *Phys. Rev. Lett.*, 78(12):2409–2412, 1997.

[100] A. Harscher and H. Lichte. Inelastic mean free path and mean inner potential of carbon foil and vitrified ice measured with electron holography. In *Proc. ICEM14*, volume 1, page 553, 1998.

[101] T. Head-Gordon and M. E. Johnson. Tetrahedral structure or chains for liquid water. *Proc. Natl. Acad. Sci. U.S.A.*, 103(21):7973–7977, 2006. doi: 10.1073/pnas.0510593103.

[102] Christopher H. Heath, Kiril Streletzky, Barbara E. Wyslouzil, Judith Wolk, and Reinhard Strey. H_2O–D_2O condensation in a supersonic nozzle. *J. Chem. Phys.*, 117(13):6176, 2002. doi: 10.1063/1.1502644.

[103] Christopher H. Heath, Kiril A. Streletzky, Barbara E. Wyslouzil, Judith Wolk, and Reinhard Strey. Small angle neutron scattering from D_2O–H_2O nanodroplets and binary nucleation rates in a supersonic nozzle. *J. Chem. Phys.*, 118(12):5465, 2003. doi: 10.1063/1.1554736.

[104] Eric Herbert and Frédéric Caupin. The limit of metastability of water under tension: theories and experiments. *J. Phys.: Condens. Matter*, 17 (45):S3597–S3602, 2005.

[105] Andreas Hermann and Peter Schwerdtfeger. Ground-state properties of crystalline ice from periodic Hartree-Fock calculations and a coupled-cluster-based many-body decomposition of the correlation energy. *Phys. Rev. Lett.*, 101(18), oct 2008. doi: 10.1103/physrevlett.101.183005.

[106] Andreas Hermann, Robert P. Krawczyk, Matthias Lein, Peter Schwerdtfeger, I. P. Hamilton, and James J. P. Stewart. Convergence of the many-body expansion of interaction potentials: From van der Waals to covalent and metallic systems. *Phys. Rev. A*, 76(1), 2007. doi: 10.1103/physreva.76.013202.

[107] Golrokh Heydari, Esben Thormann, Mikael Järn, Eric Tyrode, and Per M. Claesson. Hydrophobic surfaces: Topography effects on wetting by supercooled water and freezing delay. *J. Phys. Chem. C*, 117(42):21752–21762, 2013. doi: 10.1021/jp404396m.

[108] Golrokh Heydari, Maziar Sedighi Moghaddam, Mikko Tuominen, Matthew Fielden, Janne Haapanen, Jyrki M. Mäkelä, and Per M. Claesson. Wetting hysteresis induced by temperature changes: Supercooled water on hydrophobic surfaces. *J. Colloid Interface Sci.*, 468:21–33, 2016.

[109] Joseph O. Hirschfelder, Charles F. Curtiss, and R. Byron Bird. *The Molecular Theory of Gases and Liquids*. Wiley-Interscience, 1954. ISBN 0471400653.

[110] Pavel Holoborodko. Smooth noise robust differentiators. `bit.ly/noise-differentiators`, 2008.

[111] V. Holten, C. E. Bertrand, M. A. Anisimov, and J. V. Sengers. Thermodynamics of supercooled water. *J. Chem. Phys.*, 136(9), 2012. doi: 10.1063/1.3690497.

[112] Vincent Holten, Jeremy C. Palmer, Peter H. Poole, Pablo G. Debenedetti, and Mikhail A. Anisimov. Two-state thermodynamics of the ST2 model for supercooled water. *J. Chem. Phys.*, 140(10), 2014. doi: 10.1063/1.4867287.

[113] Hans W. Horn, William C. Swope, Jed W. Pitera, Jeffry D. Madura, Thomas J. Dick, Greg L. Hura, and Teresa Head-Gordon. Development of an improved four-site water model for biomolecular simulations: TIP4P-Ew. *J. Chem. Phys.*, 120(20):9665, 2004. doi: 10.1063/1.1683075.

[114] Lei Huang and Benoît Roux. Automated force field parameterization for non-polarizable and polarizable atomic models based on ab initio target data. *J. Chem. Theory Comput.*, 9(8):10.1021/ct4003477, 2013.

[115] P.-S. Huang, G. Oberdorfer, C. Xu, X. Y. Pei, B. L. Nannenga, J. M. Rogers, F. DiMaio, T. Gonen, B. Luisi, and D. Baker. High thermodynamic stability of parametrically designed helical bundles. *Science*, 346(6208):481–485, 2014. doi: 10.1126/science.1257481.

[116] Y. Huang, C. Zhu, L. Wang, X. Cao, Y. Su, X. Jiang, S. Meng, J. Zhao, and X. C. Zeng. A new phase diagram of water under negative pressure: The rise of the lowest-density clathrate s-III. *Sci. Adv.*, 2(2), 2016. doi: 10.1126/sciadv.1501010.

[117] A. R. Imre, U. K. Deiters, T. Kraska, and I. Tiselj. The pseudocritical regions for supercritical water. *Nucl. Eng. Des.*, 252:179–183, 2012. doi: 10.1016/j.nucengdes.2012.07.007.

[118] Saeed Izadi and Alexey V. Onufriev. Accuracy limit of rigid 3-point water models. *J. Chem. Phys.*, 145(7):074501, 2016. doi: 10.1063/1.4960175.

[119] Saeed Izadi, Ramu Anandakrishnan, and Alexey V. Onufriev. Building water models: A different approach. *J. Phys. Chem. Lett.*, 5(21):3863–3871, 2014. doi: 10.1021/jz501780a.

[120] Liam C. Jacobson, Robert M. Kirby, and Valeria Molinero. How short is too short for the interactions of a water potential? Exploring the parameter space of a coarse-grained water model using uncertainty quantification. *J. Phys. Chem. B*, 118(28):8190–8202, 2014. doi: 10.1021/jp5012928.

[121] G. P. Johari. Dielectric properties of ice VII and VIII and the phase boundary between ice VI and VII. *J. Chem. Phys.*, 61(10):4292, 1974. doi: 10.1063/1.1681733.

[122] Margaret E. Johnson, Teresa Head-Gordon, and Ard A. Louis. Representability problems for coarse-grained water potentials. *J. Chem. Phys.*, 126(14):144509, 2007. doi: 10.1063/1.2715953.

[123] A. Jones, F. Cipcigan, V. P. Sokhan, J. Crain, and G. J. Martyna. Electronically coarse-grained model for water. *Phys. Rev. Lett.*, 110(22), 2013. doi: 10.1103/physrevlett.110.227801.

[124] A. P. Jones, J. Crain, F. S. Cipcigan, V. P. Sokhan, M. Modani, and G. J. Martyna. Electronically coarse-grained molecular dynamics using quantum drude oscillators. *Mol. Phys.*, 111(22-23):3465–3477, 2013. doi: 10.1080/00268976.2013.843032.

[125] Andrew Jones. *Quantum drude oscillators for accurate many-body intermolecular forces*. PhD thesis, The University of Edinburgh, 2010.

[126] Andrew Jones and Ben Leimkuhler. Adaptive stochastic methods for sampling driven molecular systems. *J. Chem. Phys.*, 135(8):084125, 2011. doi: 10.1063/1.3626941.

[127] Andrew Jones, Andrew Thompson, Jason Crain, Martin H. Müser, and Glenn J. Martyna. Norm-conserving diffusion Monte Carlo method and diagrammatic expansion of interacting drude oscillators: Application to solid xenon. *Phys. Rev. B*, 79(14), 2009. doi: 10.1103/physrevb.79.144119.

[128] Andrew P. Jones, Jason Crain, Vlad P. Sokhan, Troy W. Whitfield, and Glenn J. Martyna. Quantum drude oscillator model of atoms and molecules: Many-body polarization and dispersion interactions for atomistic simulation. *Phys. Rev. B*, 87(14), 2013. doi: 10.1103/physrevb.87.144103.

[129] William L. Jorgensen, Jayaraman Chandrasekhar, Jeffry D. Madura, Roger W. Impey, and Michael L. Klein. Comparison of simple potential functions for simulating liquid water. *J. Chem. Phys.*, 79(2):926, 1983. doi: 10.1063/1.445869.

[130] Yousung Jung and R. A. Marcus. On the theory of organic catalysis "on water". *J. Am. Chem. Soc.*, 129(17):5492–5502, 2007. doi: 10.1021/ja068120f.

[131] B. Kamb. Ice. II. a proton-ordered form of ice. *Acta Crystallogr.*, 17(11):1437–1449, 1964. doi: 10.1107/s0365110x64003553.

[132] B. Kamb. Structure of ice VI. *Science*, 150(3693):205–209, 1965. doi: 10.1126/science.150.3693.205.

[133] Yoshinori Katayama, Takeshi Mizutani, Wataru Utsumi, Osamu Shimomura, Masaaki Yamakata, and Ken-ichi Funakoshi. A first-order liquid–liquid phase transition in phosphorus. *Nature*, 403(6766):170–173, 2000. doi: 10.1038/35003143.

[134] Shawn M. Kathmann, I.-Feng William Kuo, and Christopher J. Mundy. Electronic effects on the surface potential at the vapor-liquid interface of water. *J. Am. Chem. Soc.*, 131(47):17522–17522, 2009. doi: 10.1021/ja908142d.

[135] Shawn M. Kathmann, I.-Feng William Kuo, Christopher J. Mundy, and Gregory K. Schenter. Understanding the surface potential of water. *J. Phys. Chem. B*, 115(15):4369–4377, 2011. doi: 10.1021/jp1116036.

[136] Daniel D. Kemp and Mark S. Gordon. An interpretation of the enhancement of the water dipole moment due to the presence of other water molecules. *J. Phys. Chem. A*, 112(22):4885–4894, 2008. doi: 10.1021/jp801921f.

[137] Jan Kessler, Hossam Elgabarty, Thomas Spura, Kristof Karhan, Pouya Partovi-Azar, Ali A. Hassanali, and Thomas D. Kühne. Structure and dynamics of the instantaneous water/vapor interface revisited by path-integral and ab initio molecular dynamics simulations. *J. Phys. Chem. B*, 119(31):10079–10086, 2015. doi: 10.1021/acs.jpcb.5b04185.

[138] Charles Kittel. *Introduction to Solid State Physics*. Wiley, 2004. ISBN 047141526X.

[139] Jiří Klimeš, David R. Bowler, and Angelos Michaelides. Chemical accuracy for the van der Waals density functional. *J. Phys.: Condens. Matter*, 22 (2):022201, 2009. doi: 10.1088/0953-8984/22/2/022201.

[140] S. Klotz, J. M. Besson, G. Hamel, R. J. Nelmes, J. S. Loveday, and W. G. Marshall. Metastable ice VII at low temperature and ambient pressure. *Nature*, 398(6729):681–684, 1999. doi: 10.1038/19480.

[141] N. N. Kochurova and A. I. Rusanov. Dynamic surface properties of water: Surface tension and surface potential. *J. Colloid Interface Sci.*, 81(2):297–303, 1981. doi: 10.1016/0021-9797(81)90411-2.

[142] Nobuyasu Koga, Rie Tatsumi-Koga, Gaohua Liu, Rong Xiao, Thomas B. Acton, Gaetano T. Montelione, and David Baker. Principles for designing ideal protein structures. *Nature*, 491(7423):222–227, 2012. doi: 10.1038/nature11600.

[143] Thomas D. Kühne and Rustam Z. Khaliullin. Electronic signature of the instantaneous asymmetry in the first coordination shell of liquid water. *Nature Comm*, 4:1450, 2013. doi: 10.1038/ncomms2459.

[144] Thomas D. Kühne and Rustam Z. Khaliullin. Nature of the asymmetry in the hydrogen-bond networks of hexagonal ice and liquid water. *J. Am. Chem. Soc.*, 136(9):3395–3399, 2014. doi: 10.1021/ja411161a.

[145] Thomas D. Kühne, Tod A. Pascal, Efthimios Kaxiras, and Yousung Jung. New insights into the structure of the vapor/water interface from large-scale first-principles simulations. *J. Phys. Chem. Lett.*, 2(2):105–113, 2011. doi: 10.1021/jz101391r.

[146] W. F. Kuhs, J. L. Finney, C. Vettier, and D. V. Bliss. Structure and hydrogen ordering in ices VI, VII, and VIII by neutron powder diffraction. *J. Chem. Phys.*, 81(8):3612, 1984. doi: 10.1063/1.448109.

[147] R. Kumar, J. R. Schmidt, and J. L. Skinner. Hydrogen bonding definitions and dynamics in liquid water. *J. Chem. Phys.*, 126(20):204107, 2007. doi: 10.1063/1.2742385.

[148] Anna-Pitschna E. Kunz and Wilfred F. van Gunsteren. Development of a nonlinear classical polarization model for liquid water and aqueous solutions: COS/D. *J. Phys. Chem. A*, 113(43):11570–11579, 2009. doi: 10.1021/jp903164s.

[149] I.-F. Will Kuo, Christopher J. Mundy, Becky L. Eggimann, Matthew J. McGrath, J. Ilja Siepmann, Bin Chen, John Vieceli, and Douglas J. Tobias. Structure and dynamics of the aqueous liquid-vapor interface: A comprehensive particle-based simulation study. *J. Phys. Chem. B*, 110(8): 3738–3746, 2006. doi: 10.1021/jp056330t.

[150] I.-Feng W. Kuo and Christopher J. Mundy. An ab initio molecular dynamics study of the aqueous liquid-vapor interface. *Science*, 303(5658):658–660, 2004. doi: 10.1126/science.1092787.

[151] Guillaume Lamoureux, Alexander D. MacKerell, and Benoît Roux. A simple polarizable model of water based on classical drude oscillators. *J. Chem. Phys.*, 119(10):5185, 2003. doi: 10.1063/1.1598191.

[152] Guillaume Lamoureux, Edward Harder, Igor V. Vorobyov, Benoît Roux, and Alexander D. MacKerell. A polarizable model of water for molecular dynamics simulations of biomolecules. *Chem. Phys. Lett.*, 418(1-3):245–249, 2006. doi: 10.1016/j.cplett.2005.10.135.

[153] A. J. Leadbetter, R. C. Ward, J. W. Clark, P. A. Tucker, T. Matsuo, and H. Suga. The equilibrium low-temperature structure of ice. *J. Chem. Phys.*, 82(1):424, 1985. doi: 10.1063/1.448763.

[154] E. W. Lemmon, M. O. McLinden, and D. G. Friend. *"Thermophysical Properties of Fluid Systems, NIST Standard Reference Database Number 69"*. National Institute of Standards and Technology, 2016. Retrieved 18 September 2014.

[155] Kevin Leung. Surface potential at the air-water interface computed using density functional theory. *J. Phys. Chem. Lett.*, 1(2):496–499, 2010. doi: 10.1021/jz900268s.

[156] Tianshu Li, Davide Donadio, Giovanna Russo, and Giulia Galli. Homogeneous ice nucleation from supercooled water. *Phys. Chem. Chem. Phys.*, 13(44):19807, 2011. doi: 10.1039/c1cp22167a.

[157] David T. Limmer and David Chandler. The putative liquid-liquid transition is a liquid-solid transition in atomistic models of water. *J. Chem. Phys.*, 135(13):134503, 2011. doi: 10.1063/1.3643333.

[158] David T. Limmer and David Chandler. Corresponding states for mesostructure and dynamics of supercooled water. *Faraday Discuss.*, 167: 485–498, 2013. doi: 10.1039/C3FD00076A.

[159] David T. Limmer and David Chandler. The putative liquid-liquid transition is a liquid-solid transition in atomistic models of water. II. *J. Chem. Phys.*, 138(21), 2013. doi: 10.1063/1.4807479.

[160] David T. Limmer and David Chandler. Theory of amorphous ices. *Proc. Natl. Acad. Sci. U.S.A.*, 111(26):9413–8, 2014. doi: 10.1073/pnas.1407277111.

[161] David T. Limmer and David Chandler. Time scales of supercooled water and implications for reversible polyamorphism. *Mol. Phys.*, 113(May):2799–2804, 2015. doi: 10.1080/00268976.2015.1029552.

[162] I.-Chun Lin, Ari P. Seitsonen, Ivano Tavernelli, and Ursula Rothlisberger. Structure and dynamics of liquid water from ab initio molecular dynamics—comparison of BLYP, PBE, and revPBE density functionals with and without van der waals corrections. *J. Chem. Theory Comput.*, 8 (10):3902–3910, 2012. doi: 10.1021/ct3001848.

[163] Yang Liu, Athanassios Z. Panagiotopoulos, and Pablo G. Debenedetti. Low-temperature fluid-phase behavior of ST2 water. *J. Chem. Phys.*, 131(10), 2009. doi: 10.1063/1.3229892.

[164] Yang Liu, Jeremy C. Palmer, Athanassios Z. Panagiotopoulos, and Pablo G. Debenedetti. Liquid-liquid transition in ST2 water. *J. Chem. Phys.*, 137 (21):214505, 2012.

[165] C. Lobban, J. L. Finney, and W. F. Kuhs. The p–T dependency of the ice II crystal structure and the effect of helium inclusion. *J. Chem. Phys.*, 117 (8):3928, 2002. doi: 10.1063/1.1495837.

[166] Colin Lobban, John L. Finney, and Werner F. Kuhs. The structure and ordering of ices III and V. *J. Chem. Phys.*, 112(16):7169, 2000. doi: 10.1063/1.481282.

[167] Thomas Loerting, Katrin Winkel, Markus Seidl, Marion Bauer, Christian Mitterdorfer, Philip H. Handle, Christoph G. Salzmann, Erwin Mayer, John L. Finney, and Daniel T. Bowron. How many amorphous ices are there? *Phys. Chem. Chem. Phys.*, 13(19):8783, 2011. doi: 10.1039/c0cp02600j.

[168] F. London. The general theory of molecular forces. *Trans. Faraday Soc.*, 33(8):8b, 1937. doi: 10.1039/tf937330008b.

[169] J. D. Londono, W. F. Kuhs, and J. L. Finney. Neutron diffraction studies of ices III and IX on under-pressure and recovered samples. *J. Chem. Phys.*, 98(6):4878, 1993. doi: 10.1063/1.464942.

[170] H. A. Lorentz. Ueber die anwendung des satzes vom virial in der kinetischen theorie der gase. *Ann. Phys.*, 248(1):127–136, 1881. doi: 10.1002/andp.18812480110.

[171] V. Lotrich, N. Flocke, M. Ponton, A. D. Yau, A. Perera, E. Deumens, and R. J. Bartlett. Parallel implementation of electronic structure energy, gradient, and Hessian calculations. *J. Chem. Phys.*, 128(19), 2008. doi: 10.1063/1.2920482.

[172] Jibao Lu, Yuqing Qiu, Riccardo Baron, and Valeria Molinero. Coarse-graining of TIP4P/2005, TIP4P-Ew, SPC/E, and TIP3P to monatomic anisotropic water models using relative entropy minimization. *J. Chem. Theory Comput.*, 10(9):4104–4120, 2014. doi: 10.1021/ct500487h.

[173] Shruti Maheshwary, Nitin Patel, Narayanasami Sathyamurthy, Anant D. Kulkarni, and Shridhar R. Gadre. Structure and stability of water clusters $(H_2O)_n$, n =8-20: An ab initio investigation. *J. Phys. Chem. A*, 105(46): 10525–10537, 2001. doi: 10.1021/jp013141b.

[174] Michael W. Mahoney and William L. Jorgensen. A five-site model for liquid water and the reproduction of the density anomaly by rigid, nonpolarizable potential functions. *J. Chem. Phys.*, 112(20):8910, 2000. doi: 10.1063/1.481505.

[175] Yves A. Mantz, Bin Chen, and Glenn J. Martyna. Temperature-dependent water structure: Ab initio and empirical model predictions. *Chem. Phys. Lett.*, 405(4-6):294–299, 2005. doi: 10.1016/j.cplett.2005.02.050.

[176] M. Marqués, G. J. Ackland, and J. S. Loveday. Nature and stability of ice X. *High Pressure Res.*, 29(2):208–211, 2009. doi: 10.1080/08957950802564031.

[177] Glenn J. Martyna and Bruce J. Berne. Structure and energetics of Xe_n^-: Many-body polarization effects. *J. Chem. Phys.*, 88(7):4516, 1988. doi: 10.1063/1.453759.

[178] S. Y. Mashayak, Mara N. Jochum, Konstantin Koschke, N. R. Aluru, Victor Rühle, and Christoph Junghans. Relative entropy and optimization-driven coarse-graining methods in VOTCA. *PLoS ONE*, 10(7):e0131754, 2015. doi: 10.1371/journal.pone.0131754.

[179] Erwin Mayer and Andreas Hallbrucker. Cubic ice from liquid water. *Nature*, 325(6105):601–602, 1987. doi: 10.1038/325601a0.

[180] S. L. Miller. A production of amino acids under possible primitive earth conditions. *Science*, 117(3046):528–529, 1953. doi: 10.1126/science.117.3046.528.

[181] Claude Millot, Jean-Christophe Soetens, Marília T. C. Martins Costa, Matthew P. Hodges, and Anthony J. Stone. Revised Anisotropic Site Potentials for the Water Dimer and Calculated Properties. *J. Phys. Chem. A*, 102(4):754–770, 1998. doi: 10.1021/jp972578+.

[182] Osamu Mishima. Volume of supercooled water under pressure and the liquid-liquid critical point. *J. Chem. Phys.*, 133(14), 2010. doi: 10.1063/1.3487999.

[183] Valeria Molinero. Minimalistic models of water. Summer school lecture, 2013. URL `http://static.sif.it/SIF/resources/public/files/va2013/Molinero-1107.pdf`.

[184] Valeria Molinero and Emily B. Moore. Water modeled as an intermediate element between carbon and silicon. *J. Phys. Chem. B*, 113(13):4008–4016, 2009. doi: 10.1021/jp805227c.

[185] Emily B. Moore and Valeria Molinero. Ice crystallization in water's "no-man's land". *J. Chem. Phys.*, 132(24), 2010. doi: 10.1063/1.3451112.

[186] Emily B. Moore, Ezequiel de la Llave, Kai Welke, Damian Scherlis, and Valeria Molinero. Freezing, melting and structure of ice in a hydrophilic nanopore. *Phys. Chem. Chem. Phys.*, 12(16):4124–4134, 2010. doi: 10.1039/b919724a.

[187] Tobias Morawietz and Jörg Behler. A density-functional theory-based neural network potential for water clusters including van der Waals corrections. *J. Phys. Chem. A*, 117(32):7356–7366, 2013. doi: 10.1021/jp401225b.

[188] Tobias Morawietz, Andreas Singraber, Christoph Dellago, and Jörg Behler. How van der Waals interactions determine the unique properties of water. *Proc. Natl. Acad. Sci. U.S.A.*, 113(30):8368–8373, 2016. doi: 10.1073/pnas.1602375113.

[189] Ken-ichiro Murata and Hajime Tanaka. Liquid–liquid transition without macroscopic phase separation in a water–glycerol mixture. *Nat. Mater.*, 11(5):436–443, 2012. doi: 10.1038/nmat3271.

[190] F. D. Murnaghan. The compressibility of media under extreme pressures. *Proc. Natl. Acad. Sci. U.S.A.*, 30(9):244–247, 1944.

[191] Hiroki Nada and Jan P. J. M. van der Eerden. An intermolecular potential model for the simulation of ice and water near the melting point: A six-site model of H_2O. *J. Chem. Phys.*, 118(16):7401, 2003. doi: 10.1063/1.1562610.

[192] Béla Nagy, J. Doyne Farmer, Quan M. Bui, and Jessika E. Trancik. Statistical basis for predicting technological progress. *PLoS ONE*, 8(2):e52669, 2013. doi: 10.1371/journal.pone.0052669.

[193] Tatsuya Nakamura, Masakazu Matsumoto, Takuma Yagasaki, and Hideki Tanaka. Thermodynamic stability of ice II and its hydrogen-disordered counterpart: Role of zero-point energy. *J. Phys. Chem. B*, 120(8):1843–1848, 2016. doi: 10.1021/acs.jpcb.5b09544.

[194] Sridhar Narayan, John Muldoon, M. G. Finn, Valery V. Fokin, Hartmuth C. Kolb, and K. Barry Sharpless. "On water": Unique reactivity of organic compounds in aqueous suspension. *Angew. Chem. Int. Ed.*, 44(21):3275–3279, 2005. doi: 10.1002/anie.200462883.

[195] R. J. Nelmes, J. S. Loveday, R. M. Wilson, J. M. Besson, Ph. Pruzan, S. Klotz, G. Hamel, and S. Hull. Neutron diffraction study of the structure of deuterated ice VIII to 10 GPa. *Phys. Rev. Lett.*, 71(8):1192–1195, 1993. doi: 10.1103/physrevlett.71.1192.

[196] Satoshi Nihonyanagi, Jahur A. Mondal, Shoichi Yamaguchi, and Tahei Tahara. Structure and dynamics of interfacial water studied by heterodyne-detected vibrational sum-frequency generation. *Annu. Rev. Phys. Chem.*, 64(1):579–603, 2013. doi: 10.1146/annurev-physchem-040412-110138.

[197] A. Nilsson, D. Schlesinger, and L. G. M. Pettersson. X-ray spectroscopy, scattering and simulation studies of instantaneous structures in water. In *Proceedings of the International School of Physics "Enrico Fermi". Water: Fundamentals as the Basis for Understanding the Environment and Promoting Technology*, volume 187, pages 77–135. IOS Press Amsterdam, SIF Bologna, 2015.

[198] Nicola Nosengo. Can artificial intelligence create the next wonder material? *Nature*, 533(7601):22–25, 2016. doi: 10.1038/533022a.

[199] Lars Ojamaee and Kersti Hermansson. Ab initio study of cooperativity in water chains: Binding energies and anharmonic frequencies. *The Journal of Physical Chemistry*, 98(16):4271–4282, 1994. doi: 10.1021/j100067a011.

[200] Gaël Pallares, Mouna El Mekki Azouzi, Miguel A. González, Juan L. Aragones, José L. F. Abascal, Chantal Valeriani, and Frédéric Caupin. Anomalies in bulk supercooled water at negative pressure. *Proc. Natl. Acad. Sci. U.S.A.*, 111(22):7936–7941, 2014.

[201] Jeremy C. Palmer, Fausto Martelli, Yang Liu, Roberto Car, Athanassios Z. Panagiotopoulos, and Pablo G. Debenedetti. Metastable liquid–liquid transition in a molecular model of water. *Nature*, 510(7505):385–388, 2014. doi: 10.1038/nature13405.

[202] B. Pamuk, J. M. Soler, R. Ramírez, C. P. Herrero, P. W. Stephens, P. B. Allen, and M.-V. Fernández-Serra. Anomalous nuclear quantum effects in ice. *Physical Review Letters*, 108(19), 2012. doi: 10.1103/physrevlett.108.193003.

[203] M. Parrinello and A. Rahman. Study of an F center in molten KCl. *J. Chem. Phys.*, 80(2):860, 1984. doi: 10.1063/1.446740.

[204] L. Pauling. *The Nature of the Chemical Bond and the Structure of Molecules and Crystals: An Introduction to Modern Structural Chemistry*. Cornell University Press, 1960. ISBN 9780801403330.

[205] V. E. Petrenko, M. L. Antipova, A. V. Borovkov, and O. V. Ved'. New model pair potential for water. effect of inclusion of specific O···H interactions on the topology and dynamics of the hydrogen-bond network. *Russ. J. Gen. Chem.*, 77(10):1700–1707, 2007. doi: 10.1134/s1070363207100076.

[206] Victor F. Petrenko and Robert W. Whitworth. *Physics of Ice*. Oxford University Press, 2002. ISBN 0198518943.

[207] James C. Phillips, Rosemary Braun, Wei Wang, James Gumbart, Emad Tajkhorshid, Elizabeth Villa, Christophe Chipot, Robert D. Skeel, Laxmikant Kalé, and Klaus Schulten. Scalable molecular dynamics with NAMD. *J. Comput. Chem.*, 26(16):1781–1802, 2005. doi: 10.1002/jcc.20289.

[208] Piotr A. Pieniazek, Craig J. Tainter, and James L. Skinner. Surface of liquid water: Three-body interactions and vibrational sum-frequency spectroscopy. *J. Am. Chem. Soc.*, 133(27):10360–10363, 2011. doi: 10.1021/ja2026695.

[209] Carlos Pinilla, Amir H. Irani, Nicola Seriani, and Sandro Scandolo. Ab initio parameterization of an all-atom polarizable and dissociable force field for water. *J. Chem. Phys.*, 136(11), 2012. doi: 10.1063/1.3691603.

[210] Igor Poltavsky and Alexandre Tkatchenko. Modeling quantum nuclei with perturbed path integral molecular dynamics. *Chem. Sci.*, 7(2):1368–1372, 2016. doi: 10.1039/c5sc03443d.

[211] Jay W. Ponder, Chuanjie Wu, Pengyu Ren, Vijay S. Pande, John D. Chodera, Michael J. Schnieders, Imran Haque, David L. Mobley, Daniel S. Lambrecht, Robert A. DiStasio, Martin Head-Gordon, Gary N. I. Clark, Margaret E. Johnson, and Teresa Head-Gordon. Current status of the AMOEBA polarizable force field. *J. Phys. Chem. B*, 114(8):2549–2564, 2010. doi: 10.1021/jp910674d.

[212] Peter H. Poole, Francesco Sciortino, Ulrich Essmann, and H. Eugene Stanley. Phase behaviour of metastable water. *Nature*, 360(6402):324–328, 1992. doi: 10.1038/360324a0.

[213] Peter H. Poole, Francesco Sciortino, Tor Grande, H. Eugene Stanley, and C. Austen Angell. Effect of Hydrogen Bonds on the Thermodynamic Behavior of Liquid Water. *Phys. Rev. Lett.*, 73(12):1632–1635, 1994. doi: 10.1103/PhysRevLett.73.1632.

[214] Peter H. Poole, Ivan Saika-Voivod, and Francesco Sciortino. Density minimum and liquid–liquid phase transition. *J. Phys.: Condens. Matter*, 17(43):L431–L437, 2005. doi: 10.1088/0953-8984/17/43/L01.

[215] Thomas M. Proctor. Low-temperature speed of sound in single-crystal ice. *J. Acoust. Soc. Am.*, 39(5A):972–977, 1966. doi: 10.1121/1.1909980.

[216] Aneesur Rahman. Molecular dynamics study of liquid water. *J. Chem. Phys.*, 55(7):3336, 1971. doi: 10.1063/1.1676585.

[217] Eloy Ramos-Cordoba, Daniel S. Lambrecht, and Martin Head-Gordon. Charge-transfer and the hydrogen bond: Spectroscopic and structural implications from electronic structure calculations. *Faraday Discuss.*, 150: 345, 2011. doi: 10.1039/c1fd00004g.

[218] J. E. B. Randles. Structure at the free surface of water and aqueous electrolyte solutions. *Phys. Chem. Liq.*, 7(1-2):107–179, 1977. doi: 10.1080/00319107708084730.

[219] J. E. B. Randles and D. J. Schiffrin. The temperature-dependence of the surface potential of aqueous electrolytes. *J. Electroanal. Chem.*, 10(5-6): 480–484, 1965. doi: 10.1016/0022-0728(65)80049-3.

[220] Rebecca J. Rapf and Veronica Vaida. Sunlight as an energetic driver in the synthesis of molecules necessary for life. *Phys. Chem. Chem. Phys.*, 18(30): 20067–20084, 2016. doi: 10.1039/c6cp00980h.

[221] Elizabeth A. Raymond, Teresa L. Tarbuck, Mac G. Brown, and Geraldine L. Richmond. Hydrogen-bonding interactions at the vapor/water interface investigated by vibrational sum-frequency spectroscopy of $HOD/H_2O/D_2O$ mixtures and molecular dynamics simulations. *J. Phys. Chem. B*, 107(2): 546–556, 2003. doi: 10.1021/jp021366w.

[222] Tyler Reddy, David Shorthouse, Daniel L. Parton, Elizabeth Jefferys, Philip W. Fowler, Matthieu Chavent, Marc Baaden, and Mark S. P. Sansom. Nothing to sneeze at: A dynamic and integrative computational model of an influenza a virion. *Structure*, 23(3):584–597, 2015. doi: 10.1016/j.str.2014.12.019.

[223] Pengyu Ren and Jay W. Ponder. Polarizable atomic multipole water model for molecular mechanics simulation. *J. Phys. Chem. B*, 107(24):5933–5947, 2003. doi: 10.1021/jp027815+.

[224] Jan Řezáč, Petr Jurečka, Kevin E. Riley, Jiří Černý, Haydee Valdes, Kristýna Pluháčková, Karel Berka, Tomáš Řezáč, Michal Pitoňák, Jiří Vondrášek, and Pavel Hobza. Quantum chemical benchmark energy and geometry database for molecular clusters and complex molecular systems (www.begdb.com): A users manual and examples. *Collect. Czech. Chem. Commun.*, 73(10):1261–1270, 2008. doi: 10.1135/cccc20081261.

[225] Steven W. Rick. Simulations of ice and liquid water over a range of temperatures using the fluctuating charge model. *J. Chem. Phys.*, 114 (5):2276, 2001. doi: 10.1063/1.1336805.

[226] Steven W. Rick. A reoptimization of the five-site water potential (TIP5P) for use with Ewald sums. *J. Chem. Phys.*, 120(13):6085, 2004. doi: 10.1063/1.1652434.

[227] Steven W. Rick. A polarizable, charge transfer model of water using the Drude oscillator. *J. Comput. Chem.*, 37(22):2060–2066, 2016. doi: 10.1002/jcc.24426.

[228] Steven W. Rick, Steven J. Stuart, and B. J. Berne. Dynamical fluctuating charge force fields: Application to liquid water. *J. Chem. Phys.*, 101(7):6141, 1994. doi: 10.1063/1.468398.

[229] Elisabeth Rieper, Janet Anders, and Vlatko Vedral. Quantum entanglement between the electron clouds of nucleic acids in DNA, 2010. arXiv:1006.4053.

[230] Krzysztof Rościszewski, Beate Paulus, Peter Fulde, and Hermann Stoll. Ab initio coupled-cluster calculations for the fcc and hcp structures of rare-gas solids. *Phys. Rev. B*, 62(9):5482–5488, 2000. doi: 10.1103/physrevb.62.5482.

[231] K. Z. Rushchanskii, S. Kamba, V. Goian, P. Vaněk, M. Savinov, J. Prokleška, D. Nuzhnyy, K. Knížek, F. Laufek, S. Eckel, S. K. Lamoreaux, A. O. Sushkov, M. Ležaić, and N. A. Spaldin. A multiferroic material to search for the permanent electric dipole moment of the electron. *Nat. Mater.*, 9(8):649–654, 2010. doi: 10.1038/nmat2799.

[232] John Russo, Flavio Romano, and Hajime Tanaka. New metastable form of ice and its role in the homogeneous crystallization of water. *Nat. Mater.*, 13(7):733–739, 2014. doi: 10.1038/nmat3977.

[233] C. G. Salzmann. The preparation and structures of hydrogen ordered phases of ice. *Science*, 311(5768):1758–1761, 2006. doi: 10.1126/science.1123896.

[234] Christoph G. Salzmann, Thomas Loerting, Ingrid Kohl, Erwin Mayer, and Andreas Hallbrucker. Pure ice IV from high-density amorphous ice. *J. Phys. Chem. B*, 106(22):5587–5590, 2002. doi: 10.1021/jp014391v.

[235] Christoph G. Salzmann, Paolo G. Radaelli, Erwin Mayer, and John L. Finney. Ice XV: A new thermodynamically stable phase of ice. *Phys. Rev. Lett.*, 103(10), 2009. doi: 10.1103/physrevlett.103.105701.

[236] M. J. L. Sangster and M. Dixon. Interionic potentials in alkali halides and their use in simulations of the molten salts. *Adv. Phys.*, 25(3):247–342, 1976. doi: 10.1080/00018737600101392.

[237] Biswajit Santra, Angelos Michaelides, Martin Fuchs, Alexandre Tkatchenko, Claudia Filippi, and Matthias Scheffler. On the accuracy of density-functional theory exchange-correlation functionals for H bonds in small water clusters. II. The water hexamer and van der Waals interactions. *J. Chem. Phys.*, 129(19):194111, 2008. doi: 10.1063/1.3012573.

[238] Biswajit Santra, Robert A. DiStasio, Fausto Martelli, and Roberto Car. Local structure analysis in ab initio liquid water. *Mol. Phys.*, 113(17-18):2829–2841, 2015. doi: 10.1080/00268976.2015.1058432.

[239] Srikanth Sastry, Pablo G. Debenedetti, Francesco Sciortino, and H. E. Stanley. Singularity-free interpretation of the thermodynamics of supercooled water. *Phys. Rev. E*, 53(6):6144–6154, 1996. doi: 10.1103/PhysRevE.53.6144.

[240] Julie R. Schames, Richard H. Henchman, Jay S. Siegel, Christoph A. Sotriffer, Haihong Ni, and J. Andrew McCammon. Discovery of a novel binding trench in HIV integrase. *J. Med. Chem.*, 47(8):1879–1881, 2004. doi: 10.1021/jm0341913.

[241] Jochen Schmidt, Joost VandeVondele, I.-F. William Kuo, Daniel Sebastiani, J. Ilja Siepmann, Jürg Hutter, and Christopher J. Mundy. Isobaric-isothermal molecular dynamics simulations utilizing density functional theory: An assessment of the structure and density of water at near-ambient conditions. *J. Phys. Chem. B*, 113(35):11959–11964, 2009. doi: 10.1021/jp901990u.

[242] T. U. Schülli, R. Daudin, G. Renaud, A. Vaysset, O. Geaymond, and A. Pasturel. Substrate-enhanced supercooling in AuSi eutectic droplets. *Nature*, 464(7292):1174–1177, 2010. doi: 10.1038/nature08986.

[243] J. A. Sellberg, C. Huang, T. A. McQueen, N. D. Loh, H. Laksmono, D. Schlesinger, R. G. Sierra, D. Nordlund, C. Y. Hampton, D. Starodub, D. P. DePonte, M. Beye, C. Chen, A. V. Martin, A. Barty, K. T. Wikfeldt, T. M. Weiss, C. Caronna, J. Feldkamp, L. B. Skinner, M. M. Seibert, M. Messerschmidt, G. J. Williams, S. Boutet, L. G. M. Pettersson, M. J. Bogan, and A. Nilsson. Ultrafast X-ray probing of water structure below the homogeneous ice nucleation temperature. *Nature*, 509(7505):381–4, 2014. doi: 10.1038/nature13266.

[244] Jonas A. Sellberg, Trevor A. McQueen, Hartawan Laksmono, Simon Schreck, Martin Beye, Daniel P. Deponte, Brian Kennedy, Dennis Nordlund, Raymond G. Sierra, Daniel Schlesinger, Takashi Tokushima, Iurii Zhovtobriukh, Sebastian Eckert, Vegard H. Segtnan, Hirohito Ogasawara, Katharina Kubicek, Simone Techert, Uwe Bergmann, Georgi L. Dakovski, William F. Schlotter, Yoshihisa Harada, Michael J. Bogan, Philippe Wernet, Alexander Föhlisch, Lars G. M. Pettersson, and Anders Nilsson. X-ray emission spectroscopy of bulk liquid water in no-man's land. *J. Chem. Phys.*, 142(4), 2015. doi: 10.1063/1.4905603.

[245] M. Scott Shell. The relative entropy is fundamental to multiscale and inverse thermodynamic problems. *J. Chem. Phys.*, 129(14):144108, 2008. doi: 10.1063/1.2992060.

[246] Eli Shiratani. Growth and collapse of structural patterns in the hydrogen bond network in liquid water. *J. Chem. Phys.*, 104(19):7671, 1996. doi: 10.1063/1.471475.

[247] Pier Silvestrelli and Michele Parrinello. Water molecule dipole in the gas and in the liquid phase. *Phys. Rev. Lett.*, 82(16):3308–3311, 1999. doi: 10.1103/physrevlett.82.3308.

[248] Gurmeet Singh, Apurba Nandi, and Shridhar R. Gadre. Breaking the bottleneck: Use of molecular tailoring approach for the estimation of binding energies at MP2/CBS limit for large water clusters. *J. Chem. Phys.*, 144(10):104102, 2016. doi: 10.1063/1.4943115.

[249] Rakesh S. Singh, John W. Biddle, Pablo G. Debenedetti, and Mikhail A. Anisimov. Two-state thermodynamics and the possibility of a liquid-liquid phase transition in supercooled TIP4P/2005 water. *J. Chem. Phys.*, 144 (14):144504, 2016. doi: 10.1063/1.4944986.

[250] L. B. Skinner, C. J. Benmore, J. C. Neuefeind, and J. B. Parise. The structure of water around the compressibility minimum. *J. Chem. Phys.*, 141(21), 2014. doi: 10.1063/1.4902412.

[251] Frank Smallenburg and Francesco Sciortino. Tuning the liquid-liquid transition by modulating the hydrogen-bond angular flexibility in a model for water. *Phys. Rev. Lett.*, 115(1):015701, 2015. doi: 10.1103/physrevlett.115.015701.

[252] National Snow and Ice Data Center. Facts about glaciers. `https://web.archive.org/web/20160828222708/http://nsidc.org/cryosphere/glaciers/quickfacts.html`, 2016. Accessed 28 August 2016.

[253] V. P. Sokhan and D. J. Tildesley. The free surface of water: molecular orientation, surface potential and nonlinear susceptibility. *Mol. Phys.*, 92 (4):625–640, 1997. doi: 10.1080/002689797169916.

[254] V. P. Sokhan, A. Jones, F. S. Cipcigan, J. Crain, and G. J. Martyna. Molecular-scale remnants of the liquid-gas transition in supercritical polar fluids. *Phys. Rev. Lett.*, 115(11), 2015. doi: 10.1103/physrevlett.115.117801.

[255] Vlad P. Sokhan, Andrew P. Jones, Flaviu S. Cipcigan, Jason Crain, and Glenn J. Martyna. Signature properties of water: Their molecular electronic origins. *Proc. Natl. Acad. Sci. U.S.A.*, 112(20):6431–6346, 2015. doi: 10.1073/pnas.1418982112.

[256] Sanjoy M. Som, David C. Catling, Jelte P. Harnmeijer, Peter M. Polivka, and Roger Buick. Air density 2.7 billion years ago limited to less than twice modern levels by fossil raindrop imprints. *Nature*, 484(7394):359–362, 2012. doi: 10.1038/nature10890.

[257] A. K. Soper. The radial distribution functions of water and ice from 220 to 673 K and at pressures up to 400 MPa. *Chem. Phys.*, 258(2-3):121–137, 2000. doi: 10.1016/s0301-0104(00)00179-8.

[258] A. K. Soper. The radial distribution functions of water as derived from radiation total scattering experiments: Is there anything we can say for sure? *ISRN Phys. Chem.*, pages 1–67, 2013. doi: 10.1155/2013/279463.

[259] M. J. Sparnaay. On the additivity of London-van der Waals forces. *Physica*, 25(1-6):217–231, 1959. doi: 10.1016/S0031-8914(59)92714-4.

[260] Robin J. Speedy. Stability-limit conjecture. An interpretation of the properties of water. *J. Phys. Chem.*, 86(6):982–991, 1982. doi: 10.1007/s00542-005-0004-z.

[261] Michiel Sprik and Michael L. Klein. A polarizable model for water using distributed charge sites. *J. Chem. Phys.*, 89(12):7556, 1988. doi: 10.1063/1.455722.

[262] Frank H. Stillinger and Aneesur Rahman. Improved simulation of liquid water by molecular dynamics. *J. Chem. Phys.*, 60(4):1545–1557, 1974. doi: 10.1063/1.1681229.

[263] Kiril A. Streletzky, Yury Zvinevich, Barbara E. Wyslouzil, and Reinhard Strey. Controlling nucleation and growth of nanodroplets in supersonic nozzles. *J. Chem. Phys.*, 116(10):4058, 2002. doi: 10.1063/1.1446031.

[264] A Tabazadeh, Y. S. Djikaev, and H. Reiss. Surface crystallization of supercooled water in clouds. *Proc. Natl. Acad. Sci. U.S.A.*, 99(25):15873–8, 2002. doi: 10.1073/pnas.252640699.

[265] Yasuhiro Tachibana, Lionel Vayssieres, and James R. Durrant. Artificial photosynthesis for solar water-splitting. *Nature Photonics*, 6(8):511–518, 2012. doi: 10.1038/nphoton.2012.175.

[266] G. Tammann. Ueber die grenzen des festen zustandes IV. *Ann. Phys.*, 307 (5):1–31, 1900. doi: 10.1002/andp.19003070502.

[267] Ivy Tan, Trude Storelvmo, and Mark D. Zelinka. Observational constraints on mixed-phase clouds imply higher climate sensitivity. *Science*, 352(6282): 224–227, 2016. doi: 10.1126/science.aad5300.

[268] Hajime Tanaka. Simple physical model of liquid water. *J. Chem. Phys.*, 112(2000):799, 2000. doi: 10.1063/1.480609.

[269] Berhane Temelso, Kaye A. Archer, and George C. Shields. Benchmark structures and binding energies of small water clusters with anharmonicity corrections. *J. Phys. Chem. A*, 115(43):12034–12046, 2011. doi: 10.1021/jp2069489.

[270] A. R. Thomson, C. W. Wood, A. J. Burton, G. J. Bartlett, R. B. Sessions, R. L. Brady, and D. N. Woolfson. Computational design of water-soluble α-helical barrels. *Science*, 346(6208):485–488, 2014. doi: 10.1126/science.1257452.

[271] Alexandre Tkatchenko and Matthias Scheffler. Accurate molecular van der Waals interactions from ground-state electron density and free-atom reference data. *Phys. Rev. Lett.*, 102(7), 2009. doi: 10.1103/physrevlett.102.073005.

[272] Alexandre Tkatchenko, Robert A. DiStasio, Roberto Car, and Matthias Scheffler. Accurate and efficient method for many-body van der Waals interactions. *Phys. Rev. Lett.*, 108(23), 2012. doi: 10.1103/physrevlett.108.236402.

[273] Alexandre Tkatchenko, Alberto Ambrosetti, and Robert A. DiStasio. Interatomic methods for the dispersion energy derived from the adiabatic connection fluctuation-dissipation theorem. *J. Chem. Phys.*, 138(7):074106, 2013. doi: 10.1063/1.4789814.

[274] Owen B. Toon and Richard P. Turco. Polar stratospheric clouds and ozone depletion. *Scientific American*, 264(6):68–74, 1991. doi: 10.1038/scientificamerican0691-68.

[275] G. M. Torrie and J. P. Valleau. Nonphysical sampling distributions in Monte Carlo free-energy estimation: Umbrella sampling. *J. Chem. Phys*, 23(2):187–199, 1977. doi: 10.1016/0021-9991(77)90121-8.

[276] H. F. Trotter. On the product of semi-groups of operators. *Proc. Amer. Math. Soc*, 10(4):545–545, 1959. doi: 10.1090/s0002-9939-1959-0108732-6.

[277] M. Tuckerman, B. J. Berne, and G. J. Martyna. Reversible multiple time scale molecular dynamics. *The Journal of Chemical Physics*, 97(3):1990, 1992. doi: 10.1063/1.463137.

[278] Mark E. Tuckerman, Bruce J. Berne, Glenn J. Martyna, and Michael L. Klein. Efficient molecular dynamics and hybrid Monte Carlo algorithms for path integrals. *J. Chem. Phys.*, 99(4):2796, 1993. doi: 10.1063/1.465188.

[279] J. Urquidi, C. J. Benmore, P. A. Egelstaff, M. Guthrie, S. E. Mclain, C. A. Tulk, D. D. Klug, and J. F. C. Turner. A structural comparison of supercooled water and intermediate density amorphous ices. *Mol. Phys.*, 102(19-20):2007–2014, 2004. doi: 10.1080/00268970412331292650.

[280] C. Vega and J. L. F. Abascal. Relation between the melting temperature and the temperature of maximum density for the most common models of water. *J. Chem. Phys.*, 123(14):144504, 2005. doi: 10.1063/1.2056539.

[281] C. Vega, J. L. F. Abascal, E. Sanz, L. G. MacDowell, and C. McBride. Can simple models describe the phase diagram of water? *J. Phys.: Condens. Matter*, 17(45):S3283–S3288, 2005. doi: 10.1088/0953-8984/17/45/013.

[282] Carlos Vega. Water: one molecule, two surfaces, one mistake. *Mol. Phys.*, 113(9-10):1145–1163, 2015. doi: 10.1080/00268976.2015.1005191.

[283] Carlos Vega and Jose L. F. Abascal. Simulating water with rigid non-polarizable models: a general perspective. *Phys. Chem. Chem. Phys.*, 13 (44):19663, 2011. doi: 10.1039/c1cp22168j.

[284] Carlos Vega, Carl McBride, Eduardo Sanz, and Jose L. F. Abascal. Radial distribution functions and densities for the SPC/E, TIP4P and TIP5P models for liquid water and ices Ih, Ic, II, III, IV, v, VI, VII, VIII, IX, XI and XII. *Phys. Chem. Chem. Phys.*, 7(7):1450, 2005. doi: 10.1039/b418934e.

[285] O. Anatole von Lilienfeld and Alexandre Tkatchenko. Two- and three-body interatomic dispersion energy contributions to binding in molecules and solids. *J. Chem. Phys.*, 132(23):234109, 2010. doi: 10.1063/1.3432765.

[286] Jacob W. Wagner, James F. Dama, Aleksander E. P. Durumeric, and Gregory A. Voth. On the representability problem and the physical meaning of coarse-grained models. *J. Chem. Phys.*, 145(4):044108, 2016. doi: 10.1063/1.4959168.

[287] W. Wagner and A. Pruß. The IAPWS formulation 1995 for the thermodynamic properties of ordinary water substance for general and scientific use. *J. Phys. Chem. Ref. Data*, 31(2):387–535, 2002.

[288] Marvin Waldman and A. T. Hagler. New combining rules for rare gas van der Waals parameters. *J. Comput. Chem.*, 14(9):1077–1084, 1993. doi: 10.1002/jcc.540140909.

[289] F. Wang and K. D. Jordan. Application of a Drude model to the binding of excess electrons to water clusters. *J. Chem. Phys.*, 116(16):6973–6981, 2002. doi: 10.1063/1.1461811.

[290] Jun Wang, Piotr Cieplak, Qin Cai, Meng-Juei Hsieh, Junmei Wang, Yong Duan, and Ray Luo. Development of polarizable models for molecular mechanical calculations. 3. Polarizable water models conforming to thole polarization screening schemes. *J. Phys. Chem. B*, 116(28):7999–8008, 2012. doi: 10.1021/jp212117d.

[291] Zhe Wang, Kanae Ito, Juscelino B. Leão, Leland Harriger, Yun Liu, and Sow-Hsin Chen. Liquid–liquid phase transition and its phase diagram in deeply–cooled heavy water confined in a nanoporous silica matrix. *J. Phys. Chem. Lett.*, 6(11):2009–2014, 2015.

[292] Zhe Wang, Peisi Le, Kanae Ito, Juscelino B. Leão, Madhusudan Tyagi, and Sow Hsin Chen. Dynamic crossover in deeply cooled water confined in MCM-41 at 4 kbar and its relation to the liquid-liquid transition hypothesis. *J. Chem. Phys.*, 143(11), 2015. doi: 10.1063/1.4930855.

[293] Franz J. Wegner. Corrections to scaling laws. *Phys. Rev. B*, 5(11):4529–4536, 1972. doi: 10.1103/physrevb.5.4529.

[294] Ph. Wernet, D. Nordlund, U. Bergmann, M. Cavalleri, M. Odelius, H. Ogasawara, L. Å. Näslund, T. K. Hirsch, L. Ojamäe, P. Glatzel, L. G. M. Pettersson, and A. Nilsson. The structure of the first coordination shell in liquid water. *Science*, 304(5673):995–999, 2004. doi: 10.1126/science.1096205.

[295] E. Whalley. Dielectric properties of ice VII. Ice VIII: A new phase of ice. *J. Chem. Phys.*, 45(11):3976, 1966. doi: 10.1063/1.1727447.

[296] E. Whalley. The O-H distance in ice. *Molecular Physics*, 28(4):1105–1108, 1974. doi: 10.1080/00268977400102431.

[297] Troy W. Whitfield and Glenn J. Martyna. A unified formalism for many-body polarization and dispersion: The quantum Drude model applied to fluid xenon. *Chem. Phys. Lett.*, 424(4-6):409–413, 2006. doi: 10.1016/j.cplett.2006.04.035.

[298] Troy W. Whitfield and Glenn J. Martyna. Low variance energy estimators for systems of quantum Drude oscillators: Treating harmonic path integrals with large separations of time scales. *J. Chem. Phys.*, 126:074104, 2007. doi: 10.1063/1.2424708.

[299] Collin D. Wick, I.-Feng W. Kuo, Christopher J. Mundy, and Liem X. Dang. The effect of polarizability for understanding the molecular structure of aqueous interfaces. *J. Chem. Theory Comput.*, 3(6):2002–2010, 2007. doi: 10.1021/ct700098z.

[300] Simon A. Wilde, John W. Valley, William H. Peck, and Colin M. Graham. Evidence from detrital zircons for the existence of continental crust and oceans on the earth 4.4 Gyr ago. *Nature*, 409(6817):175–178, 2001. doi: 10.1038/35051550.

[301] Adam P. Willard and David Chandler. Instantaneous liquid interfaces. *J. Phys. Chem. B*, 114(5):1954–1958, 2010. doi: 10.1021/jp909219k.

[302] Robert W. Williams and Daksh Malhotra. van der Waals corrections to density functional theory calculations: Methane, ethane, ethylene, benzene, formaldehyde, ammonia, water, PBE, and CPMD. *Chem. Phys.*, 327(1):54–62, 2006. doi: 10.1016/j.chemphys.2006.03.037.

[303] Soohaeng Yoo Willow, Michael A. Salim, Kwang S. Kim, and So Hirata. Ab initio molecular dynamics of liquid water using embedded-fragment second-order many-body perturbation theory towards its accurate property prediction. *Sci. Rep.*, 5:14358, 2015. doi: 10.1038/srep14358.

[304] Kevin R. Wilson, Matteo Cavalleri, Bruce S. Rude, Richard D. Schaller, A. Nilsson, L. G. M. Pettersson, N. Goldman, Tony Catalano, J. D. Bozek, and R. J. Saykally. Characterization of hydrogen bond acceptor

molecules at the water surface using near-edge x-ray absorption fine-structure spectroscopy and density functional theory. *J. Phys.: Condens. Matter*, 14(8):L221–L226, 2002. doi: 10.1088/0953-8984/14/8/107.

[305] Kevin R. Wilson, R. D. Schaller, D. T. Co, R. J. Saykally, Bruce S. Rude, T. Catalano, and J. D. Bozek. Surface relaxation in liquid water and methanol studied by x-ray absorption spectroscopy. *J. Chem. Phys.*, 117 (16):7738, 2002. doi: 10.1063/1.1508364.

[306] Michael A. Wilson, Andrew. Pohorille, and Lawrence R. Pratt. Molecular dynamics of the water liquid-vapor interface. *J. Phys. Chem.*, 91(19):4873–4878, 1987. doi: 10.1021/j100303a002.

[307] Yujie Wu, Harald L. Tepper, and Gregory A. Voth. Flexible simple point-charge water model with improved liquid-state properties. *J. Chem. Phys.*, 124(2):024503, 2006. doi: 10.1063/1.2136877.

[308] B. E. Wyslouzil, J. L. Cheung, G. Wilemski, and R. Strey. Small angle neutron scattering from nanodroplet aerosols. *Phys. Rev. Lett.*, 79(3):431–434, 1997. doi: 10.1103/PhysRevLett.79.431.

[309] L. Xu, P. Kumar, S. V. Buldyrev, S. H. Chen, P. H. Poole, F. Sciortino, and H. E. Stanley. Relation between the Widom line and the dynamic crossover in systems with a liquid-liquid phase transition. *Proc. Natl. Acad. Sci. U.S.A.*, 102(46):16558–16562, 2005.

[310] Limei Xu and Valeria Molinero. Is there a liquid-liquid transition in confined water? *J. Phys. Chem. B*, 115(48):14210–14216, 2011. doi: 10.1021/jp205045k.

[311] Soohaeng Yoo, Xiao Cheng Zeng, and Sotiris S. Xantheas. On the phase diagram of water with density functional theory potentials: The melting temperature of ice I_h with the Perdew–Burke–Ernzerhof and Becke–Lee–Yang–Parr functionals. *J. Chem. Phys.*, 130(22):221102, 2009. doi: 10.1063/1.3153871.

[312] Haibo Yu and Wilfred F. van Gunsteren. Charge-on-spring polarizable water models revisited: From water clusters to liquid water to ice. *J. Chem. Phys.*, 121(19):9549, 2004. doi: 10.1063/1.1805516.

[313] Julija Zavadlav, Manuel N. Melo, Siewert J. Marrink, and Matej Praprotnik. Adaptive resolution simulation of polarizable supramolecular coarse-grained water models. *J. Chem. Phys.*, 142(24):244118, 2015. doi: 10.1063/1.4923008.